ARCHIVES OF ACOUSTICS
20, 1, 3–12 (1995)

ASSESSMENT OF FREQUENCY SELECTIVITY WITH PSYCHOACOUSTIC MASKING CURVES

T. R. ŁĘTOWSKI* and A. K. NABELEK**

* Departament of Communication Disorders
The Pennsylvania State University
University Park, PA 16802

** Departament of Audiology and Speech Pathology
The University of Tennessee
Knoxville, TN 37996–0740

Psychophysical tuning curves (PTCs) and narrow-band masking curves (NMCs) were obtained for three frequencies: 500, 1600, and 2500 Hz, using the Bekesy tracking method. Comparisons of the data obtained for seven normal and one slightly impaired ears indicate that PTCs measured at 20 dB SL and NMCs measured at 40 dB SL seem to be equally effective in describing frequency selectivity using $Q(10)$ criterion. Therefore, the choice of either methodology for assessment of frequency resolution may be dictated by its convenience and avilable instrumentation. Due to dependence of PTCs and NMCs on signal presentation level, the conclusions of this study are limited to normally hearing listeners. It is yet to be shown whether and within what range of hearing loss both measures can be treated as equivalent at higher presentation level.

1. Introduction

Psychophysical tuning curves (PTCs) and narrow-band masking curves (NMC) are two measures of frequency selectivity (frequency resolution) of the hearing system. Although there are many conflicting reports in the literature, the reduced frequency resolution is commonly regarded as one of the main factors responsible for poor speech discrimination [1, 20, 23, 24, 30]. Decrease in frequency resolution appears as „an increase in the bandwidth of a hypothesized auditory filter and a decrease in the slopes of this filter, particularly on the low-frequency side" [6, p. 667]. WEST and EVANS [27] observed that frequency resolution tests allow the detection of early asymptomatic hearing loss unrevealed by pure tone audiometry.

The most common measure of the auditory filter selectivity is the „coefficient of sharpness" $Q(10)$ defined as a center frequency of the filter divided by the filter bandwidth measured 10 dB below its maximum response [6, 21, 22, 25]. Other measures of the auditory filter selectivity recommended by various authors include:

1) the difference (in dB) between the level at the tuning curve tip and the level at which the masking or the tuning curve is an octave wide, 2) high frequency slope, and 3) tip-to-tail difference, defined as the difference (in dB) between the L_{max} at tip and the level at the intersection of two main segments of the low frequency slope [1, 4, 22]. Special advantages of the $Q(10)$ measure are its convenience and relative invariance with signal level in comparison to other measures listed above [21].

The use of frequency selectivity measures in the audiology clinic has been limited due to the correlation between the degree of hearing loss and the sharpness of tuning curves [6, 13]. The sharpness of both PTCs and NMCs changes with level and measures obtained from normally hearing listeners cannot be used as standards for comparison with data obtained from hearing impaired listeners at higher levels [15, 17]. Measures of frequency resolution may, however, by helpful in explaining differences in perceived hearing handicap for individuals with comparable pure tone thresholds [5, 26]. It is generally believed that abnormally poor frequency resolution is related to the difficulties in speech recognition in persons with similar audiometric configurations. This belief is supported by reports demonstrating wide variations in effects of masking, such as signal detection and speech recognition, among persons with similar hearing threshold configurations [2, 14, 19]. Similarly, there are reports indicating that impaired frequency resolution is not always attributable to elevated threshold of hearing [10, 12, 18] and is highly dependent on the type of hearing loss.

Clinical measures of frequency resolution are generally obtained from PTCs measured with precise but arduous laboratory methods. DAVIDSON and MELNICK [4] indicated that one of the reasons that PTC measurements are rarely used in audiology clinics is the cost and time-consuming character of these measurements. In comparison to PTCs, the NMCs are much easier and faster to obtain. For example, application of the frequency-roving tracking procedure does not require specialized equipment such as a sweeping narrow-band noise signal source needed for PTC measurements. If dicrete frequencies are used then the audiologist can just measure several thresholds of hearing in a fixed narrow-band noise using a conventional audiometer. More importantly, the task of listening to a signal that actually changes is simpler for the listener than listening to a fixed signal while ignoring the changes in the other signal. Finally, the meaning of NMCs is generally easier to explain to a client than that of PTCs.

Despite the fact that the body available literature on PTCs and NMCs is quite impressive, there are only a few studies that compared both of these measures of frequency selectivity. FLORENTINE *et al.* [6] compared four different tests of frequency selectivity: 1) psychophysical tuning curves, 2) narrow-band masking, 3) two-tone masking, and 4) loudness summation. The reference frequency was kept constant at 500 Hz or 4000 Hz. The authors concluded that the two most sensitive measures of reduced frequency sensitivity were the $Q(n)$ values of the tuning curves and the narrow-band masking.The authors used interrmittent pure tones and a 40 dB SL

narrow-band masker for measuring NMCs and a 10 dB SL test tone and a continuous pure tone masker in measuring PTCs. Their $Q(n)$ values for NMCs for normal-hearing listeners were slightly lower (mean = 5.73) than those obtained for PTCs (mean = 6.92). For hearing impaired listeners, the $Q(n)$ values were always lower than those obtained for normal hearing listeners and NMCs were frequently sharper than PTCs. The comparison of $Q(n)$ measures obtained from NMCs and PTCs is, however, possible only in relative terms since the authors used different types of maskers and different definitions of $Q(n)$ for both methods. HUMES [8] compared PTCs and NMCs using a pure tone masker and a pure tone test signal. The masker was presented at 60 or 85 dB SPL (NMC method) and the test tone at 35 dB SPL (PTC method). Inspection of his data for several heating-impaired listeners indicates much larger deviations of NMCs than PTCs from those obtained with normal-hearing listeners. He did not make, however, a direct comparsion between these two methods and only concluded that both methods showed similar results.

Despite methodological advantages, the NMC measurement have not gained the clinical popularity of the PTC measurements. The primary reason for this fact is that at high intensity levels the shapes of PTCs and NMCs are not the same. Tuning curves demonstrate effects of various narrow-band changing in frequency on a preselected narrow region of the basilar membrane. Masking curves demonstrate effects of a fixed narrow-band masker on various along the basilar membrane. The former have steeper high-frequency slopes and the latteer have steeper low-frequency slopes. However, the masking curves and the psychophysical tuning curves obtained for the „represent identical data that can be transformed from one to the other by simply interchanging ordinates and parameters" [28, p. 71]. A low stimulation levels, the shapes of PTCs and NMCs become fairly symmetrical and $Q(10)$ s of selected pairs of PTCs and NMCs may become similar measures of frequency resolution.

The purpose of the present study was to determine whether PTCs and NMCs can be equivalent measures of frequency selectivity in listeners who are audiometrically normal or exhibit a slight (<20 dB HL) hearing loss. The authors hypothesized that if the NMCs provide the same amount of clinically relevent information as the PTCs, the NMCs could be an attractive clinical alternative for frequency resolution testing of audiometrically normal patients who experienced disproportional difficulties with speech recognition. This, in turn, may lead to greater clinical popularity of frequency selectivity measures.

2. Methods

2. 1. Subjects

Four listeners participated in the study. Their air-conduction audiometric thresholds are listed in Table 1. The listeners were 30 to 42 years old. All Tests were performed monaurally for the left and right ear of each listener.

TABLE 1. Pure tone air conduction hearing thresholds (in dB HL) of the four listeners (A-D) participating in this study.

Listener	Ear	Frequency (Hz): 250	500	10000	2000	4000	8000
A	LEFT EAR	0	0	0	−10	−10	0
	RIGHT EAR	0	0	0	−5	−5	−5
B	LEFT EAR	10	5	10	10	5	0
	RIGHT EAR	15	10	15	10	5	−5
C	LEFT EAR	15	15	0	0	10	10
	RIGHT EAR	20	15	5	5	10	10
D	LEFT EAR	30	25	15	10	20	30
	RIGHT EAR	15	15	10	0	10	25

2.2. Stimili and equipment

The same three frequencies: 500, 1600 and 2500 Hz, subsequently referred to as main frequencies, were used to determine the frequency resolution of the listeners on the basis of their PTCs and NMCs. The selected frequencies correspond to the typical values of *F*1, *F*2, and *F*3 formant frequencies of several English vowels. Both tuning and masking curves were measured at seven test frequencies: 4/3, 1−, 2/3, and 1/3-octave below the main frequency, at the main frequency, and 1/3 − and 2/3-octave above the main frequency. The larger number of data points below than above the main frequency was based on previous studies indicating that the steepness of the low-frequency side of PTCs varies more among subjects than the steepness of the high-frequency side. Such arrangement of test frequencies allowed us to capture all main elements of both tuning and masking curves at low intensity levels. Pilot experiments indicated that two test frequencies set at 1/3 − and 2/3-octave intervals above the main frequency would be sufficient to obtain $Q(10)$ measures from both tuning and masking curves.

Experimental instrumentation included a Bekesy audiometer (Grason-Stadler, Model E800) supplemented by a tone generator (Wavetek, Model 159), a noise generator (Grason-Stadler, Model 455C), an electronic switch (Grason-Stadler, Model 829E), and a band-pass filter (B and K, Model 2113). The probe signal was a pulsed pure tone fixed at one of the main/test frequencies. The pulsation frequency was 2.5 pulses/sec with a 50% duty cycle. The masker was a 1/3-octave wide band of random noise centered at one of the main/test frequencies. Both signals were added together in a mixer (Numark, Model DM − 1550) and the resulting composite signal was delivered to a single TDH − 50 earphone the second earphone was inactive and covered the opposite ear of the subject through a power amplifer (SAE, Model 2200).

2.3. Procedures

In the PTC measurement task, the probe tone was presented at 20 dB SL for each subject at each main frequency and the subject controlled the level of the masker

presented at various test frequencies. In the NMC measurement task, the masking noise was presented at 40 dB SL for each subject at each main frequency and the subject controlled the level of the test tone presented at each of test frequencies. The masker level of 40 dB SL have been determined on the basis of several pilot runs with masker level 30, 40, 50, and 60 dB SL. Data reported by several authors indicate that for tone signals below 60 dB SPL the frequency resolution curves are fairly symmetrical and $Q(10)$ measures relatively invariant with level [8, 16, 21].

In both measurements performed in this study, the masked thresold estimates were obtained using a Bekesy tracking technique [4]. The listener was asked to alternately depress and release the control button of the Bekesy audiometer in order to lose and recover the signal alternatively. In the PTC task the listener controlled the level of the masker whereas in the NMC task the listener controlled them level of the tone. The listener's task was to maintain the tone at a level which was just barely audible. The listener's threshold for each main frequency was defined as the midpoint of the up-down excursions of the Bekesy tracings during the test period. The duration of each test period was set to one minute.

3. Results and discussion

Results of the measurements are shown in Figs. 1, 2, and 3 for the main frequencies 500, 1600, and 2500 Hz. Each Figure includes results of the NMC task (upper panel) and the PTC task (lower panel). The shape of data points in Figures 1 – 3 identifies the listener. To compare the slopes of individual curves obtained for the same test condition, the masked threshold values measured at the main frequency were normalized for all tested ears and expressed in the form of Relative Masking Level dB.

The psychophysical tuning curves obtained in this study (Figs. 1 – 3, lower panels) have typical „V" shapes reported in the literature. The high-frequency skirts of the curves were very similar for all listeners at all main frequencies. The NMCs (upper panels) mirrored the shapes of respective PTCs in their central and high-frequency parts. Their low-frequency slopes appeared to be less steep than high frequency slopes, contrary to findings reported by FLORENTINE *et al.*[6] for the same signal level. A possible explanation of this finding may be the inverse frequency dependence of masking patterns at low intensity levels [3, 7, 9, 11, 29].

The „coefficients of sharpness" $Q(10)$ calculated for both types of curves are listed in Table 2. The values in Table 2 are lower than those reported by other authors for listeners with normal hearing [4, 14]. They may be explained however by a relatively wide masker signal and the age of the listeners [12, 13, 17, 18].

An analysis of variance of $Q(10)$ with repeated measures on two factors (method, main frequency) showed that differences between $Q(10)$ coefficients obtained for PTC and NMC methods were not statistically significant at any main frequency. This indicates that the $Q(10)$ values derived from PTCs measured at 20 dB SL and NMCs measured at 40 dB SL can be assumed to be equivalent measures of frequency selectivity.

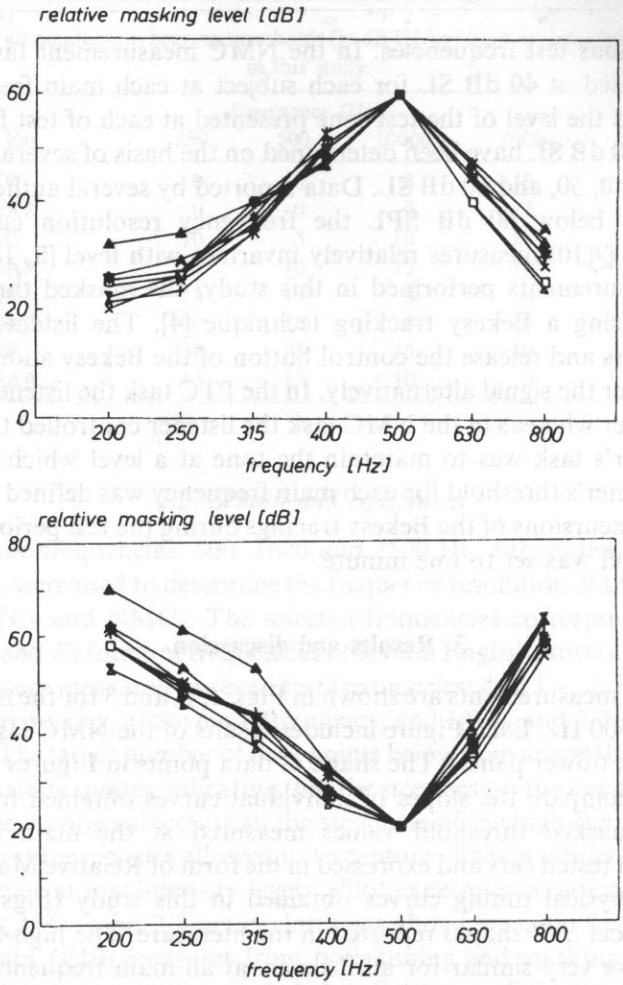

Fig. 1. Narrow-band masking curves (upper panel) and psychophysical tuning curves (bottom panel) for 500 Hz.

TABLE 2. Coefficients $Q(10)$ obtained from PTCs and for four listeners (A—D) participating in this study.

	Measure →	Coefficient $Q(10)$					
	Frequency →	500 Hz		1600 Hz		2500 Hz	
	Curve →	PTC	NMC	PTC	NMC	PTC	NMC
A	LEFT EAR	3.1	2.8	3.9	4.2	4.0	4.2
	RIGHT EAR	3.0	2.8	3.9	3.8	4.3	4.2
B	LEFT EAR	2.3	2.2	3.8	3.6	3.6	3.4
	RIGHT EAR	2.4	2.4	3.2	3.2	3.1	3.0
C	LEFT EAR	2.6	2.8	3.4	3.1	3.2	3.3
	RIGHT EAR	2.4	2.6	2.7	2.9	3.8	3.6
D	LEFT EAR	3.7	3.6	4.0	4.3	3.7	3.6
	RIGHT EAR	3.4	3.3	4.9	4.6	3.4	3.4

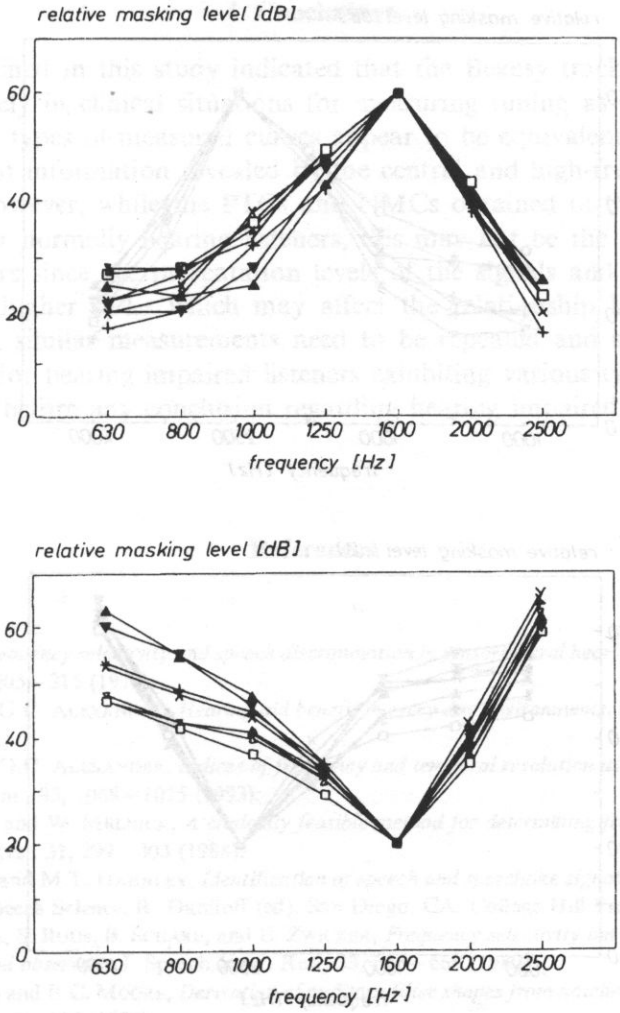

Fig. 2. Narrow-band masking curves (upper panel) and psychophysical tuning curves (bottom panel) for 1600 Hz.

The $Q(10)$ coefficients obtained from PTCs and NMCs at 500 Hz were significantly lower than those obtained at 1600 and 2500 Hz at the 0.01 level. FLORENTINE *et al.* [6] reported that $Q(10)$ calculated at 500 Hz did not differ significantly among groups of listeners with various etiologies of hearing loss whereas $Q(10)$ differed when calculated at 4000 Hz. They also reported that $Q(10)$ values were significantly smaller in all listeners with elevated bone-conduction thresholds. In our study listener D had a mild air conduction hearing loss and normal bone conduction threshold in his left ear. His $Q(10)$ values for PTC and NMC are quite similar.

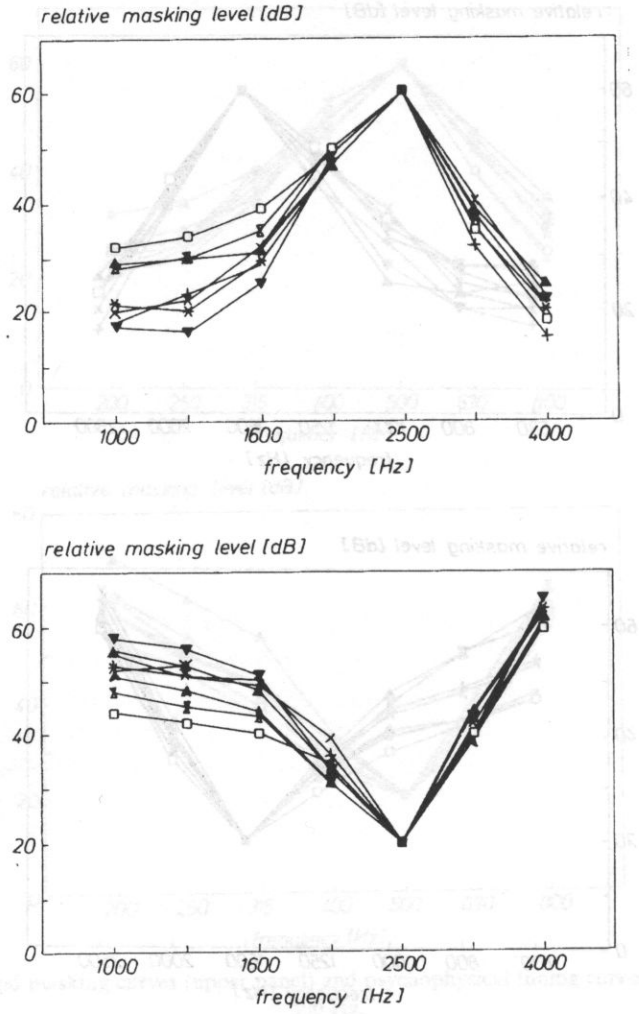

Fig. 3. Narrow-band masking curves (upper panel) and psychophysical tuning curves (bottom panel) for 2500 Hz.

However, his PTC and NMC for the left ear show steeper slopes than those observed for normal ears. This artifact was due to the presence of a conductivity hearing loss which differentially affected the signal and masker levels reaching the cochlea resulting in the shape of the curves. The subjects actual frequency sensitivity could have been the same or even worse than the frequency selectivity of the other subjects but his masking curves did not reflect this. This is an example how measurements of frequency selectivity can be confounded by the presence of conductive hearing loss.

4. Conclusions

Results obtained in this study indicated that the Bekesy tracking method can be used effectively in clinical situations for measuring tuning as well as masking curves. The two types of measured curves appear to be equivalent in terms of the type and amount information revealed by the central and high-frequency parts of their shapes. However, while the PTCs and NMCs obtained in this study appear to be similar for normally hearing listeners, this may not be the case for hearing impaired listeners since the presentation levels of the signals and maskers will be at significantly higher SPLs which may affect the relationship between the two measures. Thus, similar measurements need to be repeated and similar relationships confirmed for hearing impaired listeners exhibiting various types and degrees of hearing loos before any conclusion regarding hearing impaired listeners can be made.

References

[1] P. Bonding, *Frequency selectivity and speech discrimination in sensorineural hearing loss*, Scandinavian Audiology, **8**, 205–215 (1979).

[2] R.M. Cox and G.C. Alexander, *Hearing aid benefit in every day environments*, Ear and Hearing, **12**, 127–139 (1991).

[3] R.M. Cox and G.C. Alexander, *Indices of frequency and temporal resolution as a function of level*, J. Acoust. Soc. Am., **93**, 1068–1075 (1993).

[4] S.A. Davidson and W. Melnick, *A clinically feasible method for determining frequency resolution*, J. Speech Hear. Res., **31**, 299–303 (1988).

[5] M.F. Dorman and M.T. Hannley, *Identification of speech and speechlike signals by hearing impaired listeners*, In: **Speech Science**, R. Daniloff (ed). San Diego, CA: College-Hill Press, 1985.

[6] M. Florentine, S. Buus, B. Scharf, and E. Zwicker, *Frequency selectivity inn normally-hearing and hearing-impaired observers*. J. Speech Hear. Res., **23**, 646–669 (1980).

[7] B.R. Glasberg and B.C. Moore, *Derivation of auditory filter shapes from notched-noise data*, Hearing Research, **47**, 103–138 (1990).

[8] E.L. Humes, *Midfrequency dysfunction in listeners having high-frequency sensorineural hearing loss*, J. Speech Hear. Res., **26**, 425–435 (1983).

[9] J.F. Jerger, T.W. Tillman and J.L. Peterson, *Masking by octave bands of noise in normal and impaired ears*, J. Acoust. Soc. Am., **32**, 385–390 (1960).

[10] M.R. Leek and W. Van Summers, *Auditory filters in noise-masked normal and hearing -impaired listeners*, J. Acoust. Soc. Am., 88 (Suppl. 1), S50 (1990).

[11] R. Lutfi and R.D. Patterson, *On the growth of masking asymmetry with stimulus intensity*, J. Acoust. Soc. Am., **76**, 739–745 (1984).

[12] M.E. Lutman and J. Clark, *Speech identification under simulated hearing-aid frequency response characteristics in relation to sensitivity, frequency resolution, and temporal resolution*, J. Acoust. Soc. Am., **80**, 1030–1040 (1986).

[13] M.E. Lutman, S. Gatehouse and A.G. Worthington, *Frequency resolution as a function of hearing treshold level and age*, J. Acoust. Soc. Am., **89** (1), 320–328 (1991).

[14] E.S. Martin and J.M. Pickett, *Sensorineural hearing loss and upward spread of masking*, J. Speech Hear. Res., **13**, 426–437 (1970).

[15] D.A. NELSON, *High-level psychophysical tuning curves: Forward masking in normal-hearing and hearing- impaired listeners*, J. Speech Hear. Res., **34**, 1233–1249 (1991).

[16] D.A. NELSON, S.J. CHARGO, J.G. KOPUN and R.L. FREYMAN, *Effects of stimulus level on forward-masked psychophysical tuning curves in quiet and in noise*, J. Acoust. Soc. Am., **88**, 2143–2151 (1990).

[17] D.A. NELSON and T.W. FORTUNE, *High-level psychophysical tuning curves: Simultaneous masking with different noise bandwidths*, J. Speech Hear. Res., **34**, 374–378 (1991).

[18] R.D. PATTERSON, I. NIMMO-SMITH, D.L. WEBER and R. MILROY, *The deterioration of hearing with age: Frequency selectivity, the critical ratio, the audiogram, and speech threshold*, J. Acoust. Soc. Am., **72**, 1788–1803 (1982).

[19] W. RABINOWITZ, R.C. BILGER, C. TRAHIOTIS and J. NUETZEL, *Two-tone masking in normal hearing listeners*, J. Acoust. Soc. Am., **68**, 1096–1106 (1980).

[20] A. SIDWELL and Q. SUMMERFIELD, *The effect of enhanced spectral contrast on the internal representation of vowelshaped noise*, J. Acoust. Soc. Am., **78**, 495–506 (1985).

[21] P.G. STELMACHOWICZ and W. JESTEADT, *Psychophysical tuning curves in normal-hearing listeners: Test reliability and probe level effect*, J. Speech. Hear. Res., **27**, 396–402, (1984).

[22] P.G. STELMACHOWICZ, W. JESTEADT, M.P. GORGA and J. MOTT, *Speech perception ability and psychophysical tuning curves in hearing-impaired listeners*, J. Acoust. Soc. Am., **77** (2), 620–627 (1585).

[23] M. ter KEURS, J.M. FESTEN, R. PLOMP, *Effect of spectral envelope smearing on speech reception*, J. Acoust. Soc. Am., **91**, 2872–2880 (1992).

[24] L.M. THIBODEAU and D.J. VAN TASEL, *Tone detection and synthetic speech speech discrimination in band-rehect noise by hearing impaired listeners*, J. Acoust. Soc. Am., **82**, 864–873 (1987).

[25] C.W. TURNER and C.C. HENN, *The relation between vowel recognition and measures of frequency resolution*, J. Speech Hear. Res., **32**, 49–58 (1989).

[26] D.J. VAN TASELL, *Perception of second-formant transitions by hearing-impaired persons*, Ear and Hearing, 1, 130–136 (1980).

[27] P. WEST and E. EVANS, *Early detection of hearing damage in young listeners resulting from exposure to amplified music*, British J. Audiology, **24**, 89–103 (1990).

[28] E. ZWICKER and H. FASTEL, *Psychoacoustics*, Berlin: Springer-Verlag, 1990.

[29] E. ZWICKER and A. JAROSZEWSKI, *Inverse frequency dependance of simultaneous tone-on-tone masking patterns at low levels*, J. Acoust. Soc. Am., **71**, 1508–1512 (1982).

[30] E. ZWICKER and K. SCHORN, *Psychoacoustical tuning curves in audiology*, Audiology, **17**, 120–140 (1978).

ARCHIVES OF ACOUSTICS
20, 1, 13–26 (1995)

VIBRATION CHARACTERISTICS OF FREE VIOLIN PLATES AND THEIR RELATION TO TAP TONES DATA

A. JAROSZEWSKI, A. RAKOWSKI and J. ŻERA

Fryderyk Chopin Academy of Music
(00–368 Warszawa ul. Okólnik 2)

Frequency responses of freely suspended violin plates were measured using various kinds of plate driving and microphone location. Spectral densities of tap tones were also measured, using different points of holding, tapping and listening. The data are discussed with reference to those obtained by HUTCHINS *et al.* [1, 2, 3].

1. Introduction

Over thirty years ago, HUTCHINS, HOPPING and SAUNDERS [1] developed the concept of the „plate tone" for examination of unassembled violin plates. For this test a very light coil was attached to the centre of the freely suspended violin plate. The suitably prepared magnet pole was inserted into the coil to which a variable frequency and constant amplitude voltage was delivered. The response of the plate was picked up by a ceramic microphone. The usefulness of this test is not in question as it has been successfully used in the construction of a substantial number of instruments.

Later these authors (HUTCHINS, HOPPING and SAUNDERS [12]) gave a description of new testing equipment using a moving armature type driver and a microphone at 45 cm distance from the plate surface. The latter point seems to be reasonably important since it shows that the microphone picks up the sound energy from this part of the field where strong interference due to modal division and finite plate dimensions occurs. Also, it explains why the low frequency emission is practically cut-off, resulting in frequency response record showing: „the lowest strong resonance of the plate observed by this method", as high as 300 to 400 Hz (HUTCHINS, STETSON and TAYLOR [3]. Thus, low frequency information is not represented in these recordes.

In the previously mentioned paper, HUTCHINS *et al.* [2] state that, „before one taps a violin plate it is necessary to settle where the plate is to be held and where tapped". In this statement, which is of course very true, one additional point seems to be missing. Namely: which exact point the listener's ear should be placed? The situation analogous to the one during the electroacustic testing described by Hutchins,

Hopping and Saunders should occur only by keeping the plate 45 cm from the ear. However, to the authors' knowledge, tapping by violin makers is almost invariably done while keeping the plate rather close to the ear. In this situation, various tones can be heard depending on the exact place of listening, even if holding and tapping is done always the same way. This is due to the fact that tapping the plate, i.e. application of the mechanical pulse signal, produces a number of vibration modes and corresponding tones are radiated from various places of the plate depending on the distribution of modal lines.

In pilot experiments made prior to the research described in the present report, a group of eight expres, with very substantial experience in the experiments pertaining to pitch perception, performed the tapping on the same violin top plate. The plate was taken from the unassembled superior quality violin made late in the 18-th century by an unrecognized Italian violin maker. The plate had integral bass bar curved from the same piece of wood. Listeners were holding the plate at a given point and determined pitch intervals between tones heard from the strictly determined two points keeping the plate very close to the ear. The pitch interval thus determined was close to fourth in median value, with intersubject differences amounting to one semitone. The above observation shows that configuration of the near field naturally explored by violin makers in traditional tap-tone tests must be taken into account while choosing the place of listening. The main purpose of the present report is to show the physical differences in the signals obtained by driving the single top plate in various ways and by picking up the sound emitted by the plate from various points in the field. Some earlier data, obtained from sine driving, using Hutchins' method, and from the transducer with motional feedback driving, are also discussed, showing significant differences. The judgements of tap-tone pitch obtained from a group of six expert listeners are included.

2. The equipment and methods

A. Sine driving

In some earlier experiments with sine driving of freely suspended or clamped plates, a simple electrodynamic transducer with motional feedbeck (JAROSZEWSKI [4]) was used. With this transducer, driving with constant velocity or constant acceleration was obtained using a BK 1024 generator and compressor at 1000 dB/s with suitable 6 dB/oct filters. To compare the results with those obtained by HUTCHINS *et al.*, the coil driving of freely suspended plates (on rubber threads) was also used, possibly similar to that described in the Hutchins report [1]. The sound was picked-up using a condenser microphone located at various points of the plate 1 cm from its surface. In some tests this spacing was enlarged to 32 cm. The microphone output was amplified and fed to a BK 2305 level recorder. The measurements were conducted in a small acoustically treated room (reverberation time less than 0.5 sec).

B. Tap tones

The tap tones were picked-up with a BK 4145 1" condenser microphone located at specified points 1 cm from the plate surface and recorded on magnetic tape using a NAGRA portable tape recorder. Loops with the recorded tap tones were then analyzed using a BK 2020 slave heterodyne analyzer system at constant 3.16 Hz bandwidth. Integration constant of the level recorder was set at 500 ms to eliminate amplitude variations present in the original tap tone records. In listening to the tap tones performed by the experts, the plates were held so that the appropriate points were as close to the ear as possible. The tapping and listening was done in a way exactly following the one used by professional violin makers. The distance between the plate and the ear was about 10 cm. The tapping was performed using a knuckle of the second joint of the bent right hand forefinger. The plate was held and tapped by the same person. In all experiments the plates were held, driven or tapped and the sounds picked up at the three points V_1, H_1 and H_2 after HUTCHINS *et al.* [2], Fig. 1. All measurements and listenings were performed in the same, acoustically-treated room.

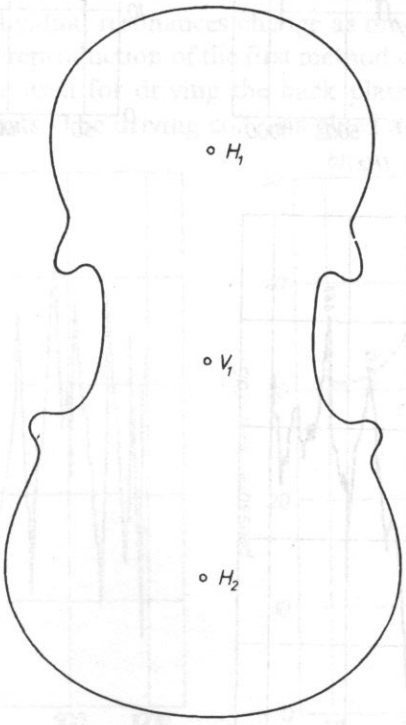

Fig. 1. Three points V_1, H_1, H_2 where the plates were held, driven or tapped and the sound picked-up (after HUTCHINS *et. al.* 1960).

3. The results

A. Sine driving

The results obtained with sine driving, both using an electrodynamic transducer with motional feedback, and the first method of those used by HUTCHINS *et al.*, (i.e.

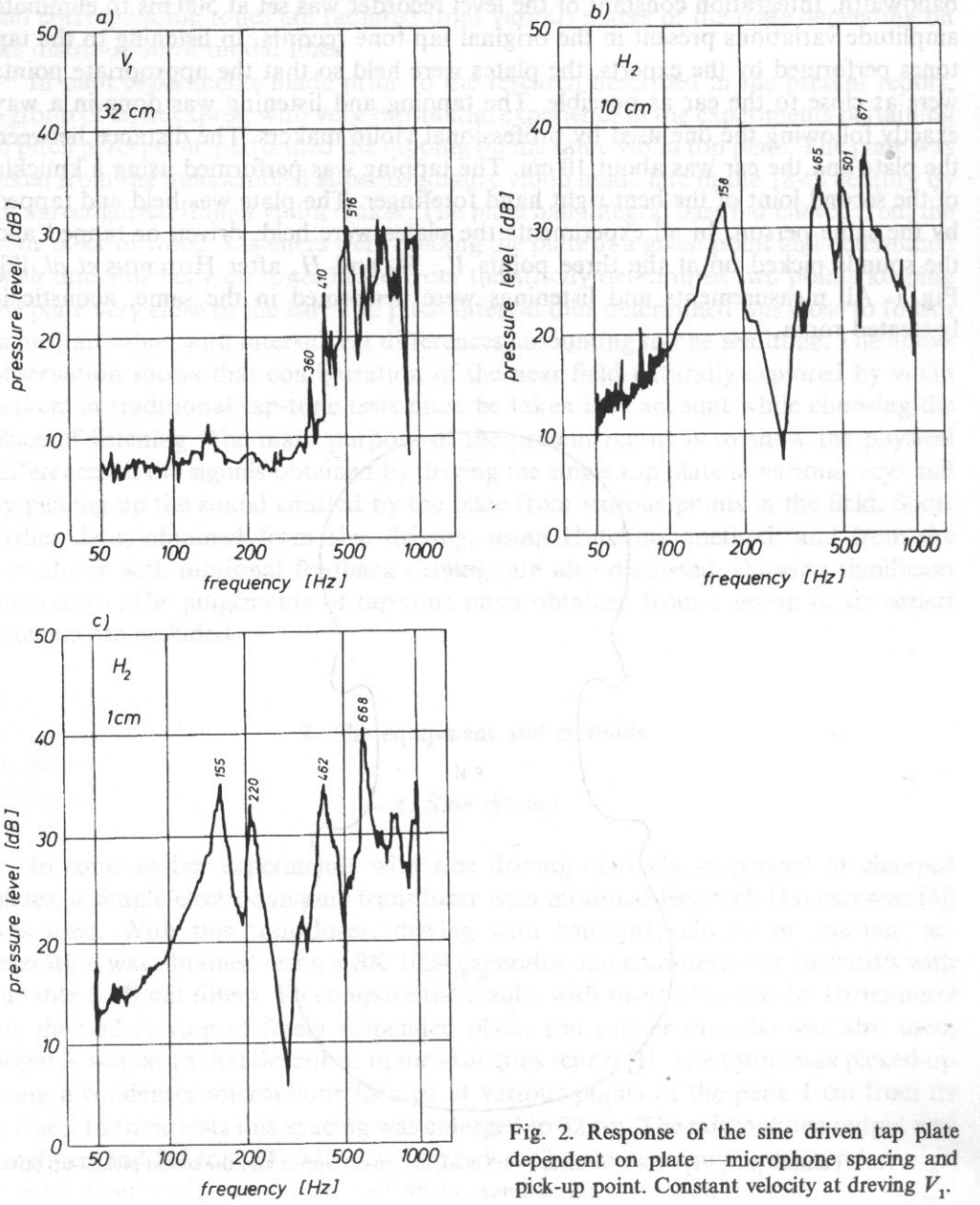

Fig. 2. Response of the sine driven tap plate dependent on plate —microphone spacing and pick-up point. Constant velocity at dreving V_1.

with speaker coil glued to the center /V_1/ of plates), are presented in Figs 2 to 5. Fig. 2 presents responses of the top plate of the superior quality violin (Italian make, late 18-century).

The plate was driven at V_1 with constant velocity and the sound emitted picked-up using a BK 4131 1" microphone at normal to V_1 and 32 cm from the plate surface. This response is similar to those that appear in the publications of HUTCHINS *et. al.*, in that the low frequency components are cut-off. For the case presented in Fig. 2 a, the lowest strong resonance should read as 360 Hz or perhaps even 410 Hz. Lower resonances were also not observed at normals to H_1 and H_2 of the same plate when the microphone was 32 cm from the plate surface. Also they were absent with different types of sine driving i.e. constant amplitude or acceleration. However, when the microphone is closer to the surface, the same plate driven also at constant velocity shows one or two well pronounced resonances lower that 360 Hz, and these are represented in Fig. 2 b and Fig. 2 c. How rapidly the field changes near the surface of the plate may be seen from the comparison of records obtained at two plate — microphone spacings, 1 cm and 10 cm (i.e. Fig. 2 b and Fig. 2 c respectively).

The effect of type of driving (i.e. constant velocity, constant acceleration) is shown in Figs. 3 a and 3b respectively. The 1/2" condenser microphone BK 4134 was located 1 cm from V_1 where the plate was driven. It can easily be seen that the amplitude relations between the individual resonances change as much as by 10 db.

The possibly accurate reproduction of the first method of plate driving introduced by HUTCHINS *et al.*[1] was used for driving the back plate of another violin, a low priced student's instruments. The driving coil was glued at V_1. The responses taken

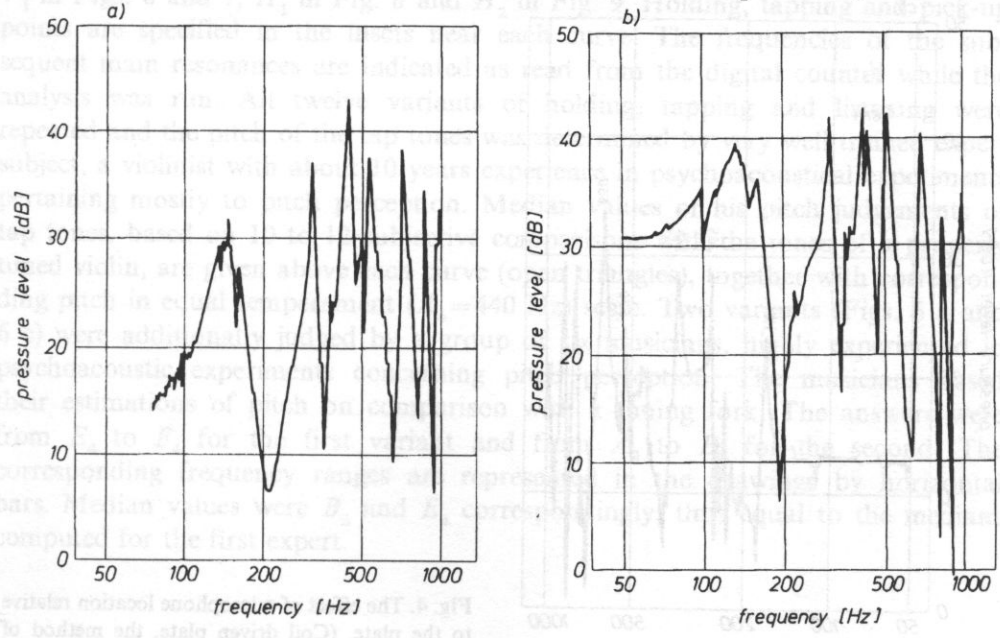

Fig. 3. The effect of driving, i.e. constant velocity *a*) and constant acceleration *b*).

from V_1, H_1 and H_2 using a BK 4145 1" microphone 1 cm from the plate are presented in Figs. 4 a, 4 b and 4 c respectively.

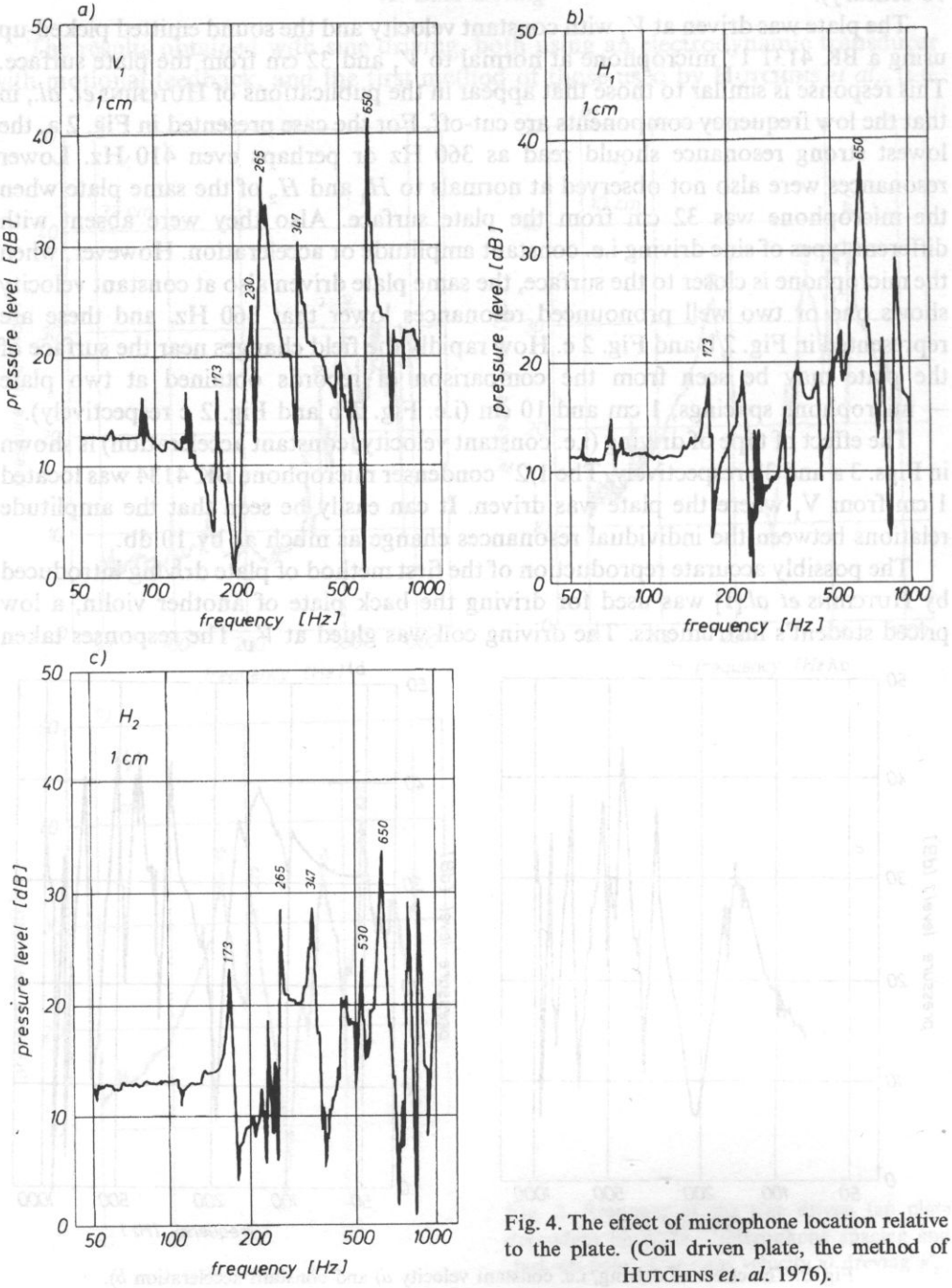

Fig. 4. The effect of microphone location relative to the plate. (Coil driven plate, the method of HUTCHINS *et. al.* 1976).

The effect of microphone placing along the plate can be seen in these results. It is evident that for V_1 the lowest strong resonance may well read 265 Hz whereas for H_1 it is 650 Hz for and H_2 perhaps 265 Hz. It seems worth pointing out that, whilst for H_2 the subsequent resonances are at 173, 265, 347, 530 and 650 Hz, for H_1 all resonances except for 650 Hz are strongly suppressed.

The responses picked-up the same way from the same back plate, but driven by electrodynamic transducer with constant velociti at V_1, are presented in Figs. 5a, 5b and 5c for pick-up points V_1, H_1 and H_2 respectively. The differences in these types of response are also observed particulary with reference to the relative pressure levels at the subsequent resonances. In all these cases, however, the pressure level for the lowest resonance at about 154 Hz is always substantial. Note that the microphone spacing in Figs. 5 a to 5 c is always 1 cm.

The differences observed between the data presented in Fig. 4 and Fig. 5 result both from the use of a different driver and its frequency response, and from the load of the plate introduced by the driver, which in both cases was different. In the case of an electrodynamic transducer with motional feedback the driving was constant over the frequency range investigated.

B. Tap tones

The results of the frequency analysis of tap tones picked up close to the plate surface and recorded on magnetic tape are presented in Figs. 6 to 9. The three curves presented in each figure were obtained using the same holding point, i.e.: V_1 in Figs. 6 and 7, H_1 in Fig. 8 and H_2 in Fig. 9. Holding, tapping and pick-up points are specified in the insets near each curve. The frequencies of the subsequent main resonances are indicated as read from the digital counter while the analysis was run. All twelve variants of holding, tapping and listening were repeated and the pitch of the tap tones was determined by very well trained expert subject, a violinist with about 10 years experience in psychoacoustical experiments pertaining mostly to pitch perception. Median values of his pitch judgements of tap tones, based on 10 to 12 subjective comparisons with the tones of a properly tuned violin, are given above each curve (open triangles), together with corresponding pitch in equal temperament (A_4=440 Hz) scale. Two variants (Figs. 6 a and 6 c) were additionally judged by a group of six musicians, highly experienced in psychoacoustic experiments concerning pitch perception. The musicians based their estimations of pitch on comparison with a tuning fork. The answers were from E_4 to F_4 for the first variant and from A_3 to B_3 for the second. The corresponding frequency ranges are represented in the drawings by horizontal bars. Median values were B_3 and E_4 correspondingly, thus equal to the medians computed for the first expert.

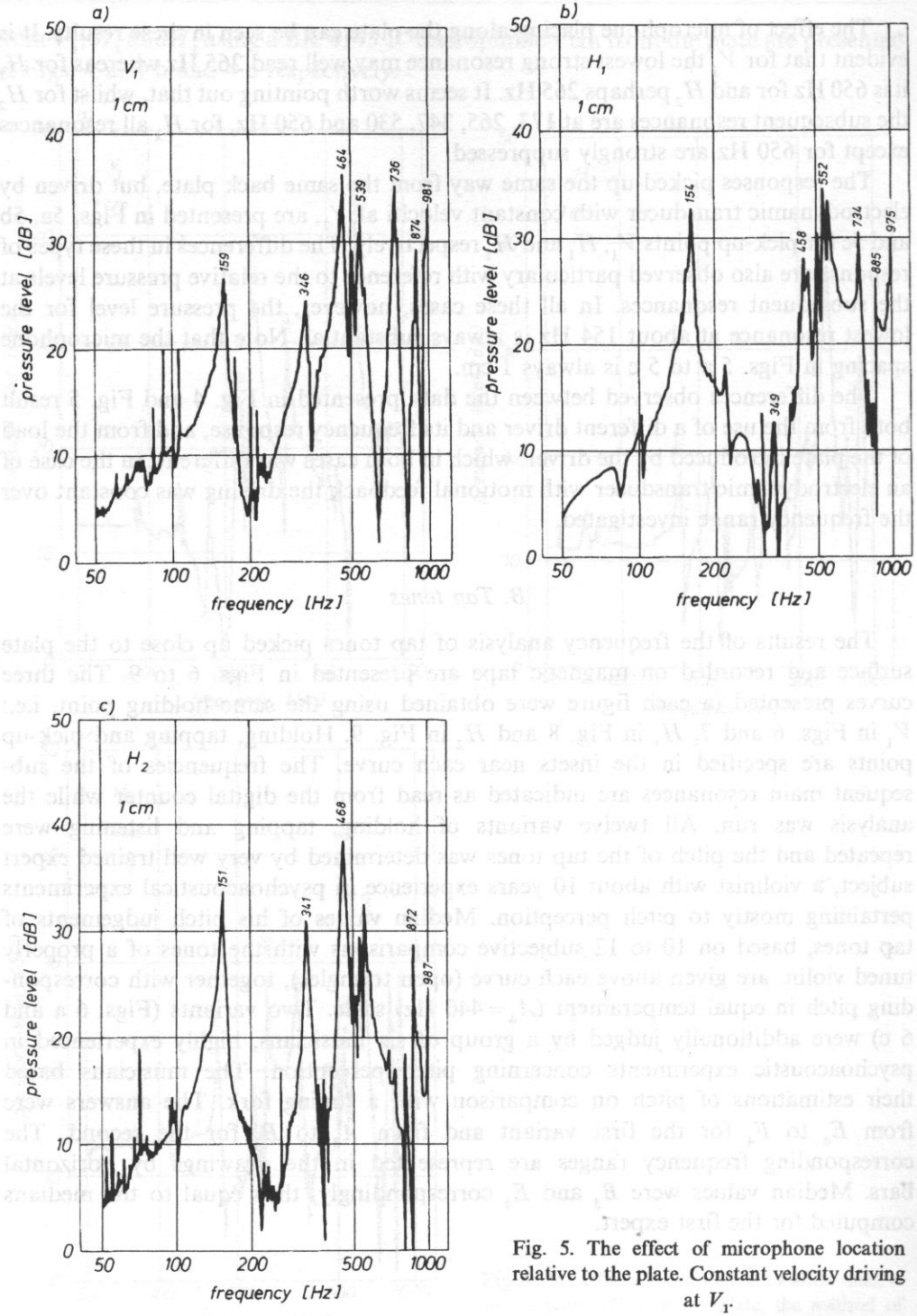

Fig. 5. The effect of microphone location relative to the plate. Constant velocity driving at V_1.

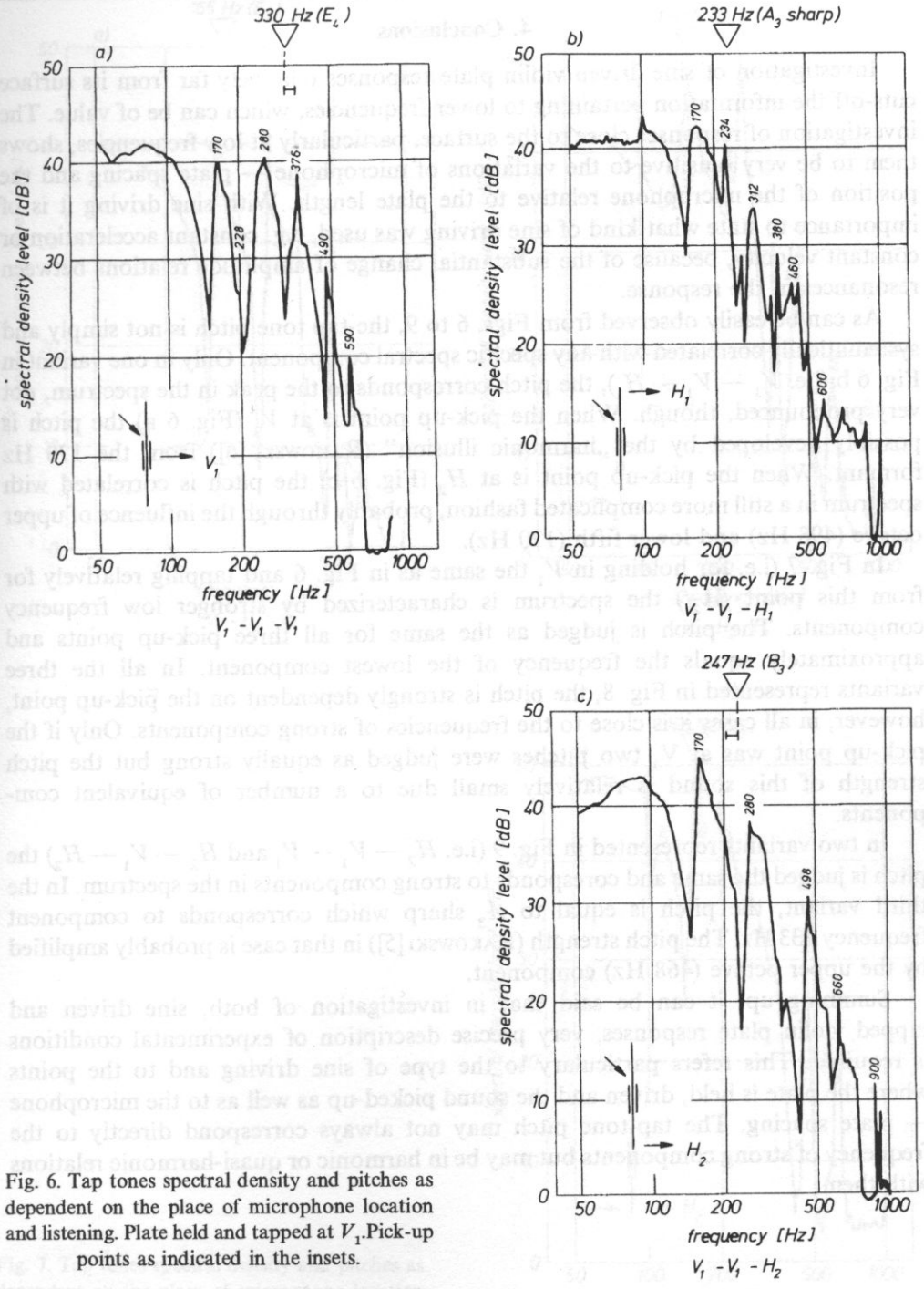

Fig. 6. Tap tones spectral density and pitches as dependent on the place of microphone location and listening. Plate held and tapped at V_1. Pick-up points as indicated in the insets.

4. Conclusions

Investigation of sine driven violin plate responses relatively far from its surface cuts-off the information pertaining to lower frequencies, which can be of value. The investigation of responses close to the surface, particularly at low frequencies, shows them to be very sensitive to the variations of microphone — plate spacing and the position of the microphone relative to the plate length. With sine driving it is of importance to state what kind of sine driving was used, e.g. constant acceleration or constant velocity, because of the substantial change of amplitude relations between resonances in the response.

As can be easily observed from Figs. 6 to 9, the-tap tone pitch is not simply and systematically correlated with any specific spectral component. Only in one variant in Fig. 6 b (i.e. $V_1 - V_1 - H_1$), the pitch corresponds to the peak in the spectrum, not very pronounced, though. When the pick-up point is at V_1 (Fig. 6 a) the pitch is possibly developed by the „harmonic illusion" (RAKOWSKI [6]) from the 170 Hz formant. When the pick-up point is at H_2 (Fig. 6 c) the pitch is correlated with spectrum in a still more complicated fashion, probably through the influence of upper octave (498 Hz) and lower fifth (170 Hz).

In Fig. 7 (i.e. for holding in V_1 the same as in Fig. 6 and tapping relatively for from this point /H_2/) the spectrum is characterized by stronger low frequency components. The pitch is judged as the same for all three pick-up points and approximately equals the frequency of the lowest component. In all the three variants represented in Fig. 8, the pitch is strongly dependent on the pick-up point, however, in all cases it is close to the frequencies of strong components. Only if the pick-up point was at V_1 two pitches were judged as equally strong but the pitch strength of this sound is relatively small due to a number of equivalent components.

In two variants represented in Fig. 9 (i.e. $H_2 - V_1 - V_1$ and $H_2 - V_1 - H_2$) the pitch is judged the same and coresponds to strong components in the spectrum. In the third variant, the pitch is equal to A_3 sharp which corresponds to component frequency 233 Hz. The pitch strength (RAKOWSKI [5]) in that case is probably amplified by the upper octave (468 Hz) component.

Summing up, it can be said that in investigation of both, sine driven and tapped violin plate responses, very precise description of experimental conditions is required. This refers particulary to the type of sine driving and to the points where the plate is held, driven and the sound picked-up as well as to the microphone — plate spacing. The tap-tone pitch may not always correspond directly to the frequency of strong components but may be in harmonic or quasi-harmonic relations with them.

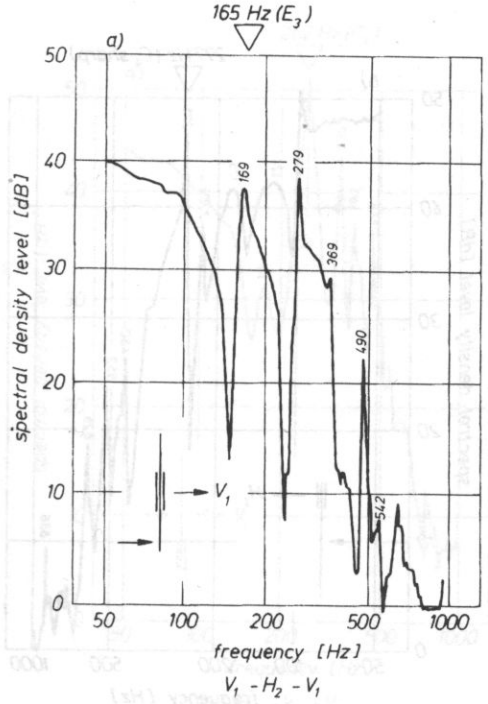

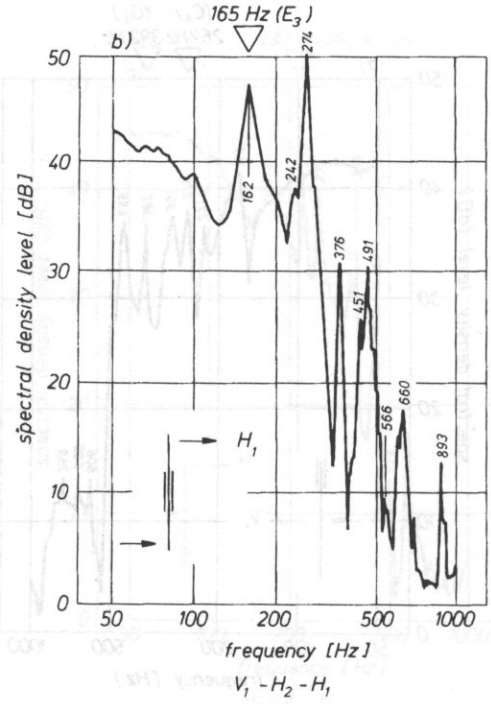

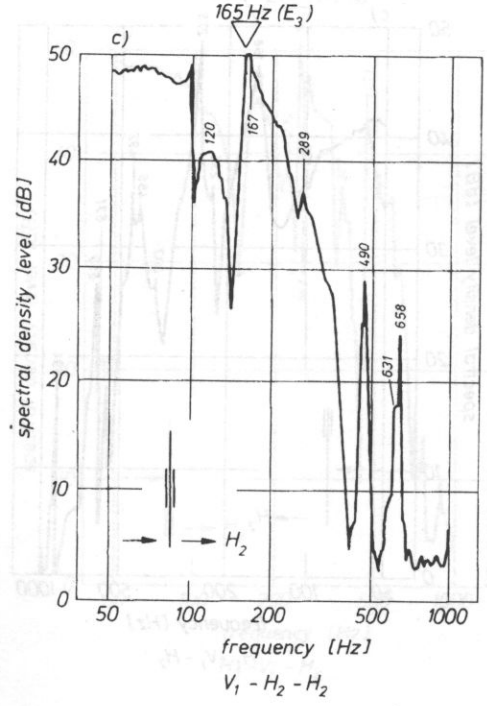

Fig. 7. Tap tones spectral density and pitches as dependent on the place of microphone location and listening. Plate held at V_1 and tapped at H_2. Pick-up points as indicated in the insets.

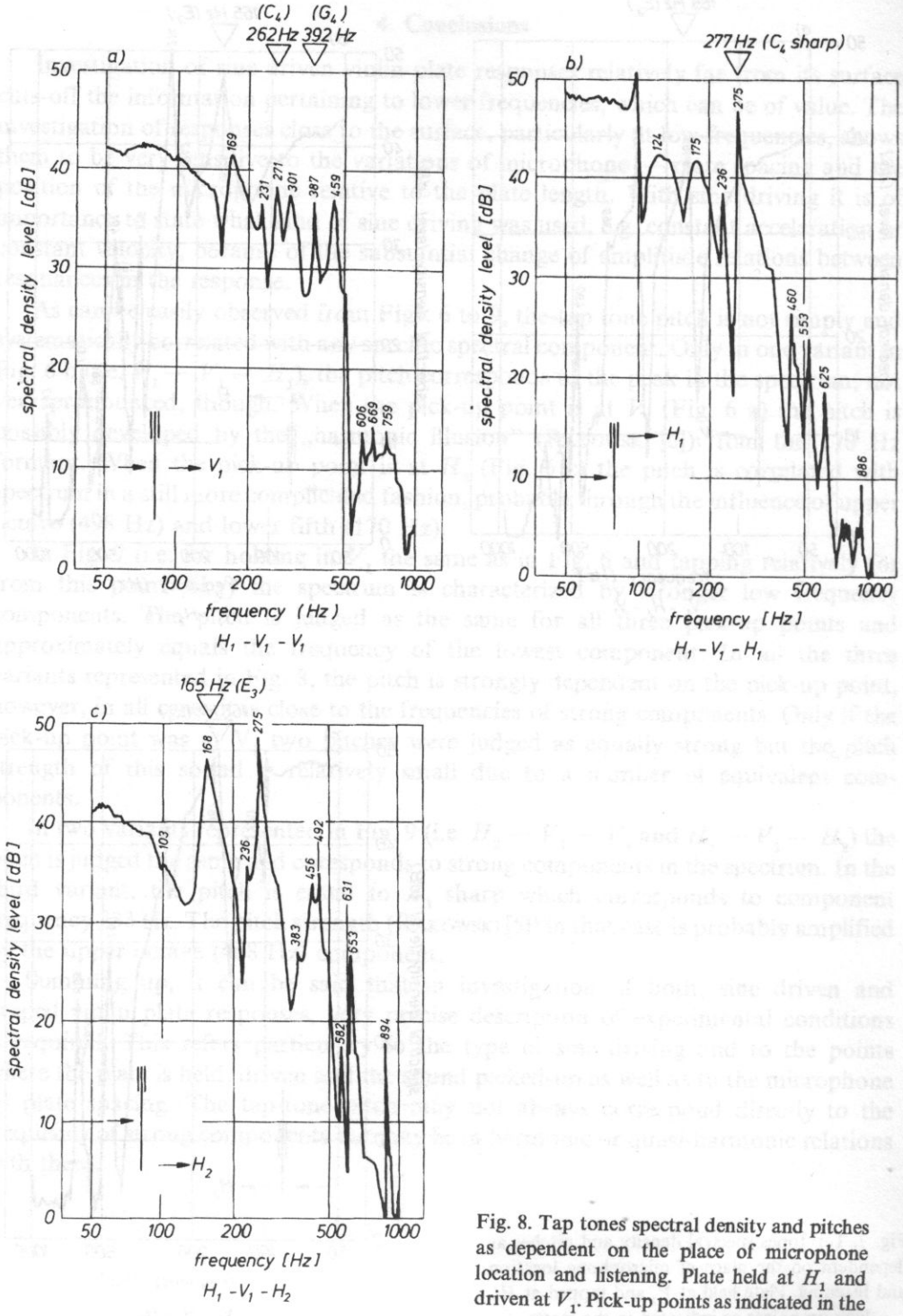

Fig. 8. Tap tones spectral density and pitches as dependent on the place of microphone location and listening. Plate held at H_1 and driven at V_1. Pick-up points as indicated in the insets.

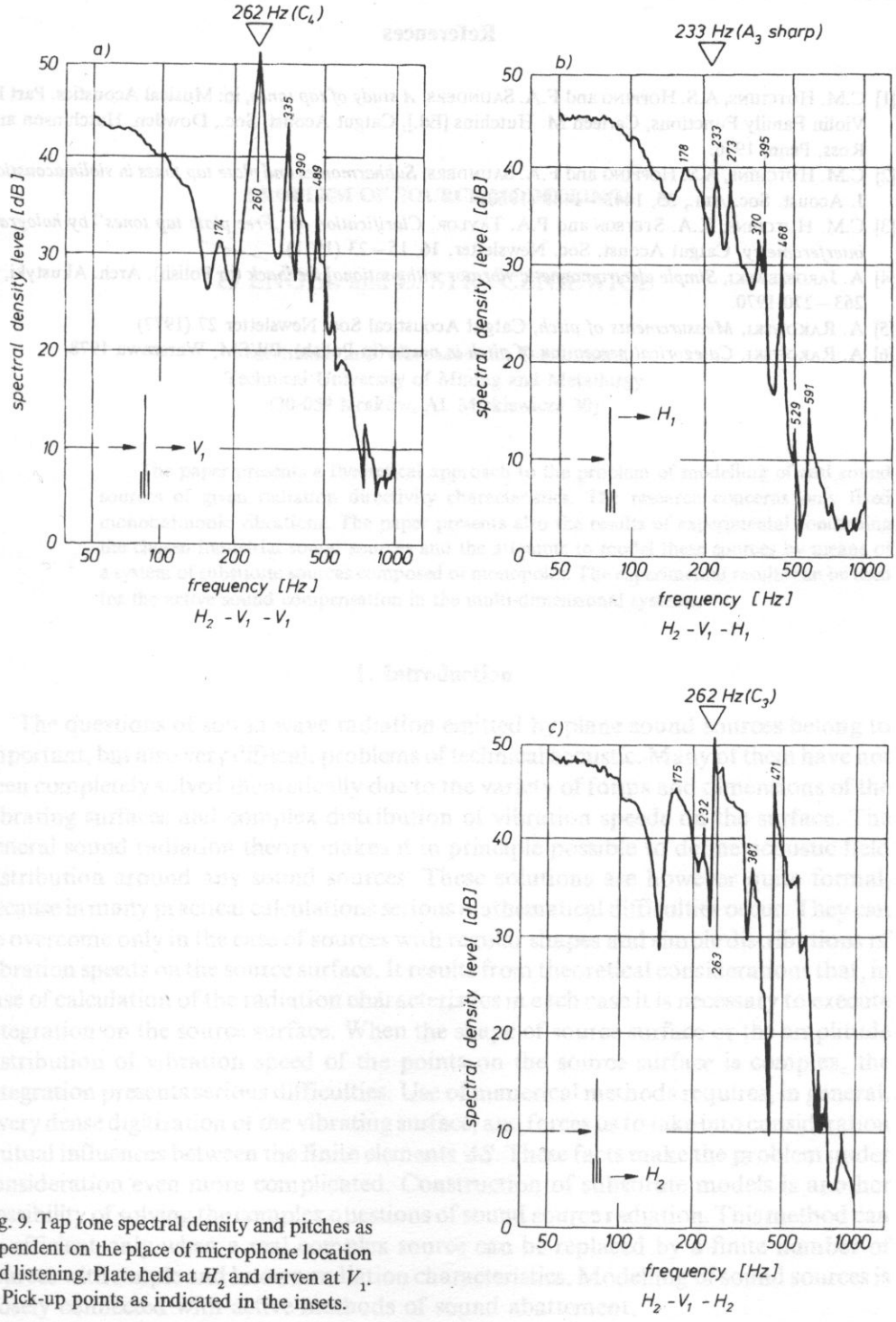

Fig. 9. Tap tone spectral density and pitches as dependent on the place of microphone location and listening. Plate held at H_2 and driven at V_1. Pick-up points as indicated in the insets.

References

[1] C.M. HUTCHINS, A.S. HOPPING and F.A. SAUNDERS, *A study of tap tones*, in: Musical Acoustics. Part II: Violin Family Functions, Carleen M. Hutchins [Ed.], Catgut Acoust. Soc., Dowden, Hutchinson and Ross, Penn, 1976.

[2] C.M. HUTCHINS, A.S. HOPPING and F.A. SAUNDERS, *Subharmonics and plate tap tones in violin acoustics*, J. Acoust. Soc. Am., **35**, 1443–1449 (1960).

[3] C.M. HUTCHINS, K.A. STETSON and P.A. TAYLOR, *Clarification of „Free plate tap tones" by hologram interferometry*, Catgut Acoust. Soc. Newsletter, **16**, 15–23 (1971).

[4] A. JAROSZEWSKI, *Simple electromagnetic vibrator with motional feedback* (in Polish), Arch. Akustyki, **2**, 263–270 1970.

[5] A. RAKOWSKI, *Measurements of pitch*, Catgut Acoustical Soc. Newsletter 27 (1977).

[6] A. RAKOWSKI, *Categorical perception of pitch in music* (in Polish), PWSM, Warszawa 1978.

ARCHIVES OF ACOUSTICS
20, 1, 27–37 (1995)

PROBLEM OF SOURCE MODELLING

Z. ENGEL and L. STRYCZNIEWICZ

Mechanics and Vibroacoustics Department
Technical University of Mining and Metallurgy
(30-059 Kraków, Al. Mickiewicza 30)

The paper presents a theoretical approach to the problem of modelling of real sound sources of given radiation directivity characteristics. The research concerns only fixed monoharmonic vibrations. The paper presents also the results of experimental concerning the chosen industrial sound sources and the attempts to model these sources by means of a system of substitute sources composed of monopoles. The experimental results can be used for the active sound compensation in the multi-dimensional systems.

1. Introduction

The questions of sound wave radiation emitted by plane sound sources belong to important, but also very difficult problems of technical acoustic. Many of them have not been completely solved theoretically due to the variety of forms and dimensions of the vibrating surfaces and complex distribution of vibration speeds on the surface. The general sound radiation theory makes it in principle possible to define acoustic field distribution around any sound sources. These solutions are however quite formal, because in many practical calculations serious mathematical difficulties occur. They can be overcome only in the case of sources with regular shapes and simple distributions of vibration speeds on the source surface. It results from theoretical considerations that, in case of calculation of the radiation characteristics in each case it is necessary to execute integration on the source surface. When the shape of source surface or the amplitude distribution of vibration speed of the points on the source surface is complex, the integration presents serious difficulties. Use of numerical methods requires, in general, a very dense digitization of the vibrating surface, and forces us to take into consideration mutual influences between the finite elements ΔS. These facts make the problem under consideration even more complicated. Construction of substitute models is another possibility of solving the complex questions of sound source radiation. This method can be efficient only when a real complex source can be replaced by a finite number of sources with simple and known radiation characteristics. Modelling of sound sources is closely connected with active methods of sound abattement.

2. Optimal parameters of substitute sound sources

When the radiation of any sound source is observed from a sufficiently great distance, i.e. from the Fraunhofer zone, the influence of geometrical dimensions of the source can be neglected and the sound source can be treated as quasi-pointwise. In the case of harmonic waves the three-dimensional distribution of acoustic pressure around the real source can be described by the formula [4]

$$p(r, \theta, \varphi) = p_0(r, 0, 0) \cdot R_0(\theta, \varphi) \text{ [Pa]} \tag{2.1}$$

Acoustic field generated by a system of substitute quasi-pointwise sources can be presented as a superposition of elementary waves emitted by individual sources.

$$p_z(r, \theta, \varphi) = \sum_{j=1}^{\infty} A_j \frac{e^{-ikr_j}}{r_j} R_j(\theta, \varphi) \quad \text{[Pa]} \tag{2.2}$$

where $A_j \frac{e^{-ikr_j}}{r_j}$ — complex amplitude of the acoustic pressure on the direction of (0, 0); r_j — distance between source j and the observation point.

Directivity indicator of source radiation depends on direction of coordinates. Dependence of radiation directivity indicator on the source localization can be presented in the form [1]:

$$\hat{R}(\theta,\varphi) = R(\theta,\varphi) \exp [ik(x_0 \cos\varphi \sin\theta + y_0 \sin\varphi \sin\theta + z_0 \cos\theta)], \tag{2.3}$$

where $\hat{R}(\theta,\varphi)$ — radiation directivity indicator of the source translated by relation to origin of coordinates by a distance of vector (x_0, y_0, z_0); $R(\theta,\varphi)$ — radiation directivity indicator of the source situated in the origin coordinates.

By comparing the distribution of acoustic fields generated by a real source and a system of substitute sources it is possible to select the parameters of source system A_n in such a way that the similarity is as strong as possible. For this purpose it is necessary to introduce a similarity criterion. One of the possible criteria is that described by the formula:

$$K = \frac{1}{4\pi A^2} \iint_S | p - p_z |^2 dS, \tag{2.4}$$

where $p = p_0(r,\theta,\varphi)$ — acoustic pressure generated by real source [Pa]; $p_z = p_z(r,\theta,\varphi)$ — total acoustic pressure of a sound source system [Pa]; A — real source moment [Pa·m]; S — surface of sphere with radius r [m²].

The functional K that was assumed can be compared by analogy with the mean square functional. Integration operation on the spherical surface can be approximated by summation. As a result, the quality functional would be proportional to the sum of squares of acoustic pressure differences. Mean square functional is often used for probability determination owing to well-developed mathematical tools. The assumed criterion has a global nature. It means that the compliance in one chosen

direction is not sufficient for the identity of acoustic fields of real source and the system of substitute sources. The simultaneous agreement in all directions is also required. The criterion assumed has also a physical interpretation. It can be interpreted as a relative acoustic power of a system of sound sources composed of a real source and substitute sources vibrating in the opposite phases. By analogy with active this is a relative acoustic power of a system with active noise compensation. Moreover, the assumed quality functional is a dimensionless quantity. In the case of absence of substitute source, the quality functional takes the value of 1, while for an ideal substitute source the functional value is equal 0.

For better interpretation, the concept of a functional level can be introduced in the form

$$L_K = -10 \log(K). \tag{2.5}$$

Functional level will assume the values from 0 in the case of absence of a substitute source, up to $+\infty$ in the case of ideal agreement between the real source and the substitute source. Similarity criterion level would correspond to the value of the decrease of acoustic power level for the system with active compensation used in active methods.

Using the functional assumed in that way it is possible to determine the optimal parameters of a system of substitute sound sources. Assuming the notation

$$\begin{aligned} A_{jx} &= \mathrm{Re}\,(A_j), \\ A_{jy} &= \mathrm{Im}\,(A_j), \end{aligned} \tag{2.6}$$

the following equations can be written in the form:

$$\frac{\partial K}{\partial A_{jx}} = 0, \qquad \frac{\partial K}{\partial A_{jy}} = 0. \tag{2.7}$$

These equations lead to the linear system of algebraic equations [6]

$$\begin{aligned} \sum_{i=1}^{m} A_{ix} U_{ji} - \sum_{i=1}^{m} A_{iy} V_{ji} &= U_{j0}, \\ \sum_{i=1}^{m} A_{ix} V_{ji} - \sum_{i=1}^{m} A_{iy} U_{ji} &= V_{j0}, \end{aligned} \tag{2.8}$$

where

$$\begin{aligned} U_{ji} &= \frac{1}{4\pi r^2} \iint_S (R_i \bar{R}_j + \bar{R}_i R_j)\, dS = U_{ij}, \\ V_{ji} &= \frac{1}{4\pi r^2} \iint_S (R_i \bar{R}_j - \bar{R}_i R_j)\, dS = -V_{ij}. \end{aligned} \tag{2.9}$$

In some cases the integrals (2.9) can be determined in an analytical way. Assuming that the substitute sources are all-directional sources (monopoles), the integrals (2.9) will equal (2.6)

$$U_{ji}=2\,\frac{\sin(kl_{ji})}{kl_{ji}}\,,\qquad V_{ji}=0\,, \tag{2.10}$$

where l_{ji} — distance between the all-directional substitute sources [m]; k — wave number [m^{-1}].

Since $V_{ij}=0$, in this case the equation system will be reduced to the form (2.11). This fact considerably simplifies the calculations.

$$\sum_{i=1}^{m} A_{ix}\,U_{ji}=U_{j0}\,,\qquad \sum_{i=1}^{m} A_{iy}\,V_{ji}=V_{j0}\,. \tag{2.11}$$

3. Experimental determination of the distribution of acoustic pressure emitted by selected industrial sound sources

The knowledge of real distribution of acoustic pressure around the industrial sound sources is necessary for calculation of parameters of the simplified emission models. For this purpose it is necessary to determine, on the hemispherical surface,

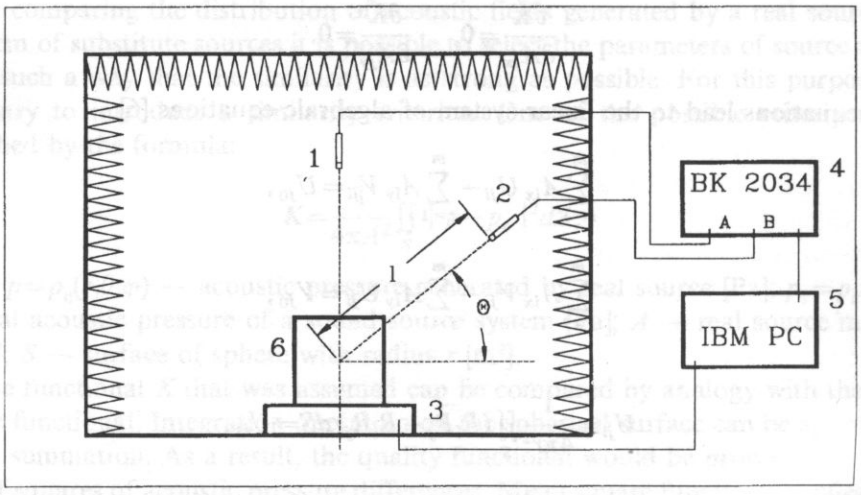

Fig. 1. Scheme of measurement system; *1, 2* — measurement microphone B&K4134 with preamplifier B&K2619; *3* — turntable B&K3921; *4* — bi-channel signal analyser B&K2034; *6* — tested object.

the distribution of acoustic pressure amplitude, as well as the distribution of angles of phase displacement between the acoustic signals. The measurement system, presented in Fig. 1, was constructed in an anechoic chamber of the Mechanics and Vibroacoustic Institute to determine the acoustic pressure distribution.

The floor in the anechoic chamber was covered by chipboard in order to secure the sound reflecting surface. The sound source tested was situated on the turntable *3*. Acoustic pressure was measured by the microphone *2*. This microphone was placed on a motionless stand at a constant distance $l=1.5$ m from the source. The angle between the line connecting the microphone with the source center and the horizon was assumed in the range from 0 to $\pi/2$ with the step of $\pi/14$. The sound source tested (situated on the turntable) rotated around its own axis. The microphone *1*, situated vertically above the sound source (in a constant direction in relation to the source) was used to compare the vibroacoustic signals. Owing to the simultaneous measurements of the signals from both microphones, it was possible to determine the phase displacements angles between the acoustic pressure occurring in a given direction (determined by the angle θ and the rotation angle of sound source φ) and the reference direction.

The measurements were executed simultaneously in the range from 20 to 20 000 [Hz]. Two-channel analyzer BK2034 was used for the simultaneous analysis of signals arriving from both microphones. Acoustic pressure amplitude was read-out from the proper spectral concentration function of the signal from the microphone *2*. In order to determine the displacement angles between signals, the functions of mutual spectral concentration between signals from microphones *1* and *2* was used. The phase displacement angle was determined from the ratio of imaginary and real parts of that function.

During the determination of acoustic pressure distribution, for each sound source the measurements were carried out in 197 measuring points. In each point 9 measurements were executed, and then the results were averaged. The amplitude of the acoustic pressure was read-out in linear units [Pa], and after averaging the pressure level was determined. By determining the average angle of phase displacement, the average value of the real part and average value of the imaginary part were first determined; then on this basis the angle was determined.

A computer was used for controlling the measurement process. It released the turntable 3 rotation. By the interface IEEE it also controlled the analyser operations. At precisely determined time instances (related with measurement point positions and turntable angular velocity), the computer released the process of registration and analysis of acoustic signals executed by the analyser. After the analysis, the data were read-out and averaged by the computer and then registered on a hard disk. The averaging was executed for 9 turntable rotations. After nine rotations the measurement process was interrupted and the arm of the microphone 2 was displaced (scheme in Fig. 1). Then the entire process was repeated up to the moment when the microphone reached the upper position (angle $= \pi/2$).

The following machines were tested

- industrial vacuum cleaner US4/20 made in Yugoslavia,
- bench grinder SZ-750 P-34/250,
- air compresor 1JS60 made by ASPO Wrocław.

For all the machines the acoustic pressure distribution were determined in frequencies of 200, 300, 400 and 500 [Hz]. The measurement results of the industrial vacuum cleaner obtained for the frequency of 200 Hz are presented in Fig. 2 as an example. The amplitude characteristic of acoustic pressure is presented in a logarithmic scale with dynamics of 50 dB, and the phase characteristic is presented in a linear scale with range $0-2\pi$ [rad].

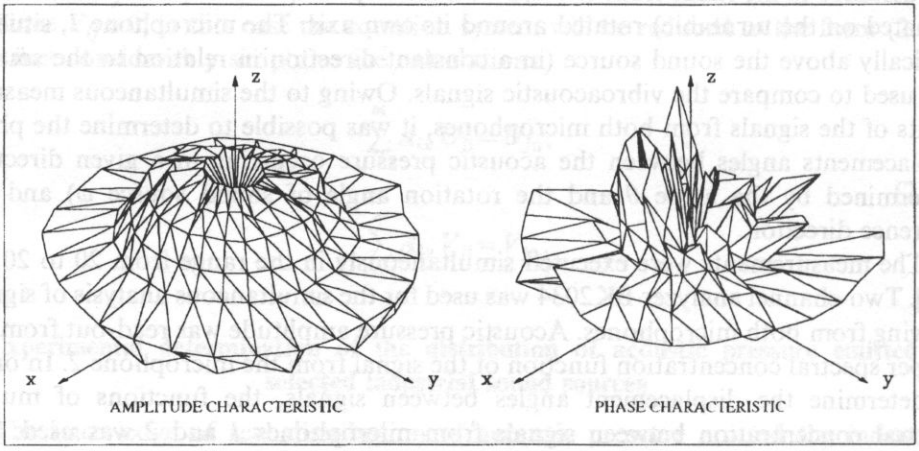

Fig. 2. Radiation directivity characteristic of bench grinder SZ-750 P-34/250. Frequency 200 [Hz].

Owing to the method of result averaging which was applied, small measurement fluctuations of the results were noticed during the experiments. It especially concerned the angle of phase displacement between the signals coming from both microphones. In several frequencies the obtained directivity characteristics of radiation are, however, very irregular. It can be observed, that in the places with significant fluctuation of the acoustic pressure amplitude, great fluctuation of phase displacement angle also occurs. Although the measurements in all frequencies were executed simultaneously, apart from the "wrenched" characteristics, very "smooth" characteristics were also obtained. The experiments were possible owing to application of the system composed of the analyser BK2034 and the computer. The computer was used to control the measurement process as well as the registration and the following result treatment.

4. The optimal arrangement and parameters of substitute sources in emission models of industrial sound sources

On the basis of measurements of acoustic pressure distribution around the chosen industrial sound sources, modelling of acoustic field of real sound sources was

executed by means of the acoustic field of all-directional source above the acoustic buffle. The calculations were executed according to the formulas (2.4), (2.10), (2.11). The modelling was done in such a way that the substitute source position was assumed to be within the cuboid with dimensions slightly large than the overall dimensions of the machine tested. For such a position the functional level and the optimal amplitude of substitute source was determined. The simulation for each machine was executed in two planes. The first (horizontal) was at the level of one half of the machine height, the second plane (vertical) ran through the source middle ($y=0$). The calculations for each machine were executed in frequencies 200, 300, 400 and 500 [Hz]. Directivity characteristic of the substitute source was determined by means of Eq. (2.3). An example of such simulation results is presented in Fig. 3.

It results from the research that only a small numbers (usually one) of local maxima of quality functional level and relative optimal amplitude occurs in the examined area. Points at which the local maxima of quality functional levels occurred, overlapped with the points, where maxima of relative optimal amplitude of substitute source occurred. In most of the cases the points of substitute source position for which the quality functional takes the greatest values can be connected with the points of machine structural elements position.

It can also be stated that at the points where quality functional maximum take place, also a maximum of amplitude occurs; however the diagram of optimal amplitude of substitute source are more irregular. It seems that the position of quality functional maximum is related to the position of dominating noise sources in the machine.

For unmistable statement of the connection between the doiminating noise sources in the machine and the maxima of the quality functional, some additional experimental research is necessary. The localization of functional maxima outside the machine can be caused by a noise of aerodynamic origin or the acoustic buffle vibrations.

Modelling of real sound sources by means of several substitute sources can be executed in many different ways. One of the possible methods is presented below. Its algorithm is shown in Fig. 4.

At the beginning it is assumed that the source characteristic is equal to the real source characteristic. It is also assumed that there is one substitute source, positioned in the origin of coordinates. The similarity criterion gradient and the optimal parameters of substitute source are determined. The substitute source is translated towards the maximal gradient direction. This operation is repeated until the local maximum is reached. Then it is verified whether the criterion is greater than required. If not, the source characteristic is changed in accordance with the relationship. The new substitute source situated in the origin of coordinates is also assumed and all the calculations are executed from the beginning, until the similarity criterion reaches the given value. As the result of this procedure, the minimal locations and with optimal parameters. An example of the result of such procedure for air compressor 1JS60 in frequency of 500 [Hz] is presented in Table 1.

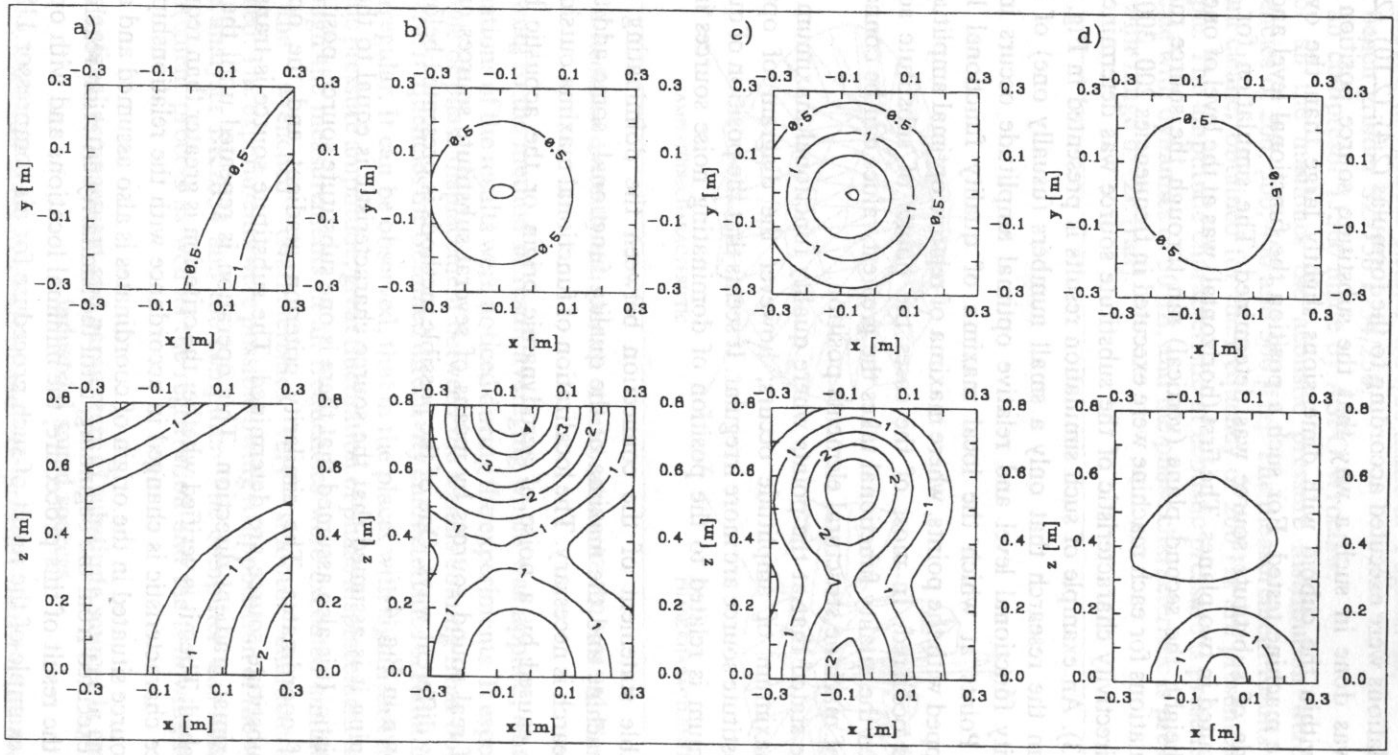

Fig. 3. Quality functional level with the real source replaced by a singular monopole. Industrial vacuum cleaner US4/20 made in Yugoslavia. Frequency: a) 200 [Hz], b) 300 [Hz], c) 400 [Hz], d) 500 [Hz].

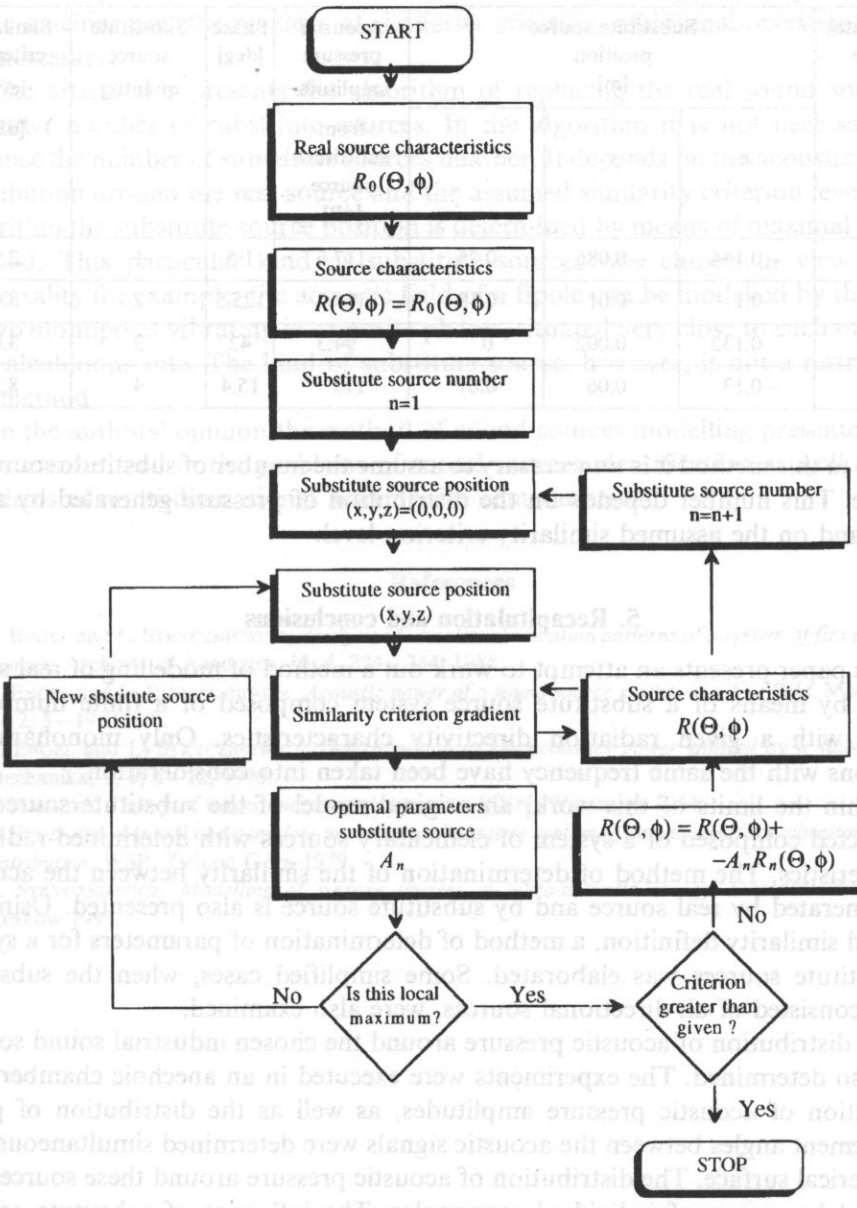

Fig. 4. Algorithm of sound source modelling by means of many substitute sources.

On the basis of the data presented in the Table, it can be noticed that when the air compressor is replaced by one monopole the functional level equals 2.9, by two monopoles — 3.4, by three — 3.6, and by four — 8.3 dB.

Table 1

Substitute source number	Substitute source position [m]			Acoustic pressure amplitude from substitute source [dB]	Phase [deg]	Substitute source quantity	Similarity criterion level [dB]
	x	y	z				
1	−0.144	−0.086	0.25	117.6	1.5	1	2.9
2	0.1	−0.01	0.19	105.3	125.5	2	3.45
3	0.132	0.002	0	94.3	42	3	3.63
4	−0.13	−0.06	0.67	113	15.4	4	8.3

Due to this method it is unnecessary to assume the number of substitute sources in advance. This number depends on the distribution of pressure generated by a real source and on the assumed similarity criterion level.

5. Recapitulation and conclusions

This paper presents an attempt to work out a method of modelling of real sound sources by means of a substitute source system composed of a finite number of sources with a given radiation directivity characteristics. Only monoharmonic vibrations with the same frequency have been taken into consideration.

Within the limits of this work, an original model of the substitute source was constructed composed of a system of elementary sources with determined radiation characteristics. The method of determination of the similarity between the acoustic field generated by real source and by substitute source is also presented. Using the assumed similarity definition, a method of determination of parameters for a system of substitute sources was elaborated. Some simplified cases, when the substitute source consisted of all-directional sources, were also examined.

The distribution of acoustic pressure around the chosen industrial sound sources were also determined. The experiments were executed in an anechoic chamber. The distribution of acoustic pressure amplitudes, as well as the distribution of phase displacement angles between the acoustic signals were determined simultaneously on the spherical surface. The distribution of acoustic pressure around these sources was modelled by means of individual monopoles. The influence of substitute sources arrangement on the quality of acoustic fields approximation, generated by the real source and the substitute source, was also examined. It results from these experiments that a small number usually one of local maxima of quality functional level and a relative optimal amplitude occurs in the examined area. The position points of substitute source in which the similarity criterion takes the largest values can be related, in most cases, to localization of the machine structural elements. In order to

determine explicitly the quantitative correlation between the dominating noise source in the machine and the maxima of similarity criterion, additional investigations are still necessary.

The article also presents the algorithm of replacing the real sound sources by a greater number of substitute sources. In the algorithm it is not necessary to in advance the number of substitute sources number. It depends on the acoustic pressure distribution around the real source and the assumed similarity criterion level. In this algorithm the substitute source position is determined by means of maximal gradient method. This particular kind of substitute sources was chosen in view of their universality for example: the acoustic field of a fipole can be modelled by the system of two monopoles vibrating in opposite phases, situated very close to each other, and the calculations rate. The kind of substitute source, however, is not a restriction of this method.

In the authors' opinion the method of sound sources modelling presented in this paper can be used in the problems of sound sources identification as well as in the problems of multi-dimensional active noise compensation.

References

[1] Z. ENGEL and L. STRYCZNIEWICZ, *Analysis of directional radiation patterns of a system of flat plane sound sources*, Archives of Acoustics, **10**, 4, 334–344, 1985.

[2] Z. ENGEL and L. STRYCZNIEWICZ, *Acoustic power of a sound source system in a free field*, Mechanika, **7**, 1–2, 5–19 (1989).

[3] Z. ENGEL and L. STRYCZNIEWICZ, *Determination as the acoustics power emitted by a vibrating plate*, Mechanika, **9**, 1, 5–12, 1990.

[4] I. MALECKI, *Theory of waves and acoustic systems*, PWN, Warszawa 1964.

[5] W. RDZANEK, *Mutual and complete impedance of a source system of variable surface vibration frequency distribution*, WSP, Zielona Góra 1979.

[6] L. STRYCZNIEWICZ, *Modelling of surface sources of vibro-acoustic energy*, Doctoral thesis, AGH, Kraków 1993.

ARCHIVES OF ACOUSTICS
20, 1, 39–56 (1995)

STATISTICAL ASPECTS OF ACOUSTIC RETURNS FROM A WIND-DRIVEN WATER SURFACE COVERED WITH ORGANIC FILMS

S.J. POGORZELSKI

Environmental Acoustics Laboratory
Institute of Experimental Physics
University of Gdańsk
(80-952 Gdańsk, Wita Stwosza 57)

The statistical properties of ultrasonic (10 MHz) signals scattered at a wind-driven water surface covered with different petroleum derivative films of well-defined and oceanographically relevant elastic surface properties were examined under laboratory and open-sea conditions. Evolution of the shape, skewness and kurtosis parameters of the signal distribution as a function of wind speed reflects a principal role played by the film elasticity. The elastic properties of composite sea surfaces likely to be present in nature and consisting of oil spills filled with a surface active material, floating solid particles, bubbles or drops of a third fluid with their important implications in remote sensing techniques are also discussed. A two-spatial scale irregularities distribution of the sea surface (capillary ripples present on tilted faces of long gravity waves) expresses itself in the corresponding signatures of at-sea experiment data.

1. Introduction

Ideally, a remote sensing system should be able to routinely detect unknown oil discharges and so act in a policing and alterting role, and also be able to accurately determine the location, extent, thickness and type of oil pollutant. No single sensor system is presently capable of performing all these tasks and so it seems that a multi-sensor approach is the optimum solution.

The hypothesis presented in a few papers by the author [1–3] could lead to a practical acoustic surveillance system for polluted sea areas. It has been demonstrated in open-sea experiments with artificial crude oil films spread over the Baltic Sea surface and a buoy-like high-frequency (10 MHz) acoustic system based on the specular forward scattering geometry that the viscoelastic film parameters can be recovered from the signal modulation spectra by means of the Marangoni damping theory and the 3-parameter best-fit procedure to the acoustic data.

Water wave attenuation by viscoelastic films is attributed to the Marangoni effect [4] which causes a strong resonance-type wave damping in the short gravity-capillary

wave region. It is evident that the Marangoni damping depends on the physicochemical nature and concentration of the film-forming substance [5]. Short gravity and capillary waves are characterized by a particular shape i.e., they have large stepness and rather small amplitudes [6]. A directional ultrasonic transducer of narrow transmitting characteristics which irradiates only a small area of the studied surface seems to form the most suitable acoustic tool to investigate scattering from such surfaces [7]. In the light of the high-frequency scattering theory the modulation spectrum of the acoustic scatter is linearly related to a wind-driven surface wave slope spectrum [8]. Although, the relationship between the ocean wave spectra and the (laser, radar, acoustic) image spectra (i.e., the transfer function) is still not satisfactory determined [9]. The same principle is fulfilled in sun glitter and laser surface probing measurements [10], where the wavelength of light is smaller than all other wavelengths on the rough surface in question [11].

Thus, the scattered signal signatures should be related (via wind waves damping) to the viscoelastic properties of the film.

So far, the smoothing effect of an oil film on a ruffled surface is expressed in the corresponding changes of statistical properties of the ultrasonic signal scattered at a wavy surface as has been already shown in laboratory and at-sea experiments [12–14]. Simultaneous analyses of all the statistical distribution parameters could be a starting point for determining the fraction weight of the given substance, its layer thickness, and finally a form of the oil pollutant (monolayer, thick layer or individual dispersed spots) [15].

This paper deals with further detailed statistical analyses of the amplitude fluctuations of the ultrasonic signal scattered from a wind-generated surface of clean water and water covered with a monolayer of well-defined oceanographically relevant elastic properties performed in a small wind-wave tank and in open-sea conditions with artificial oil slicks.

Several film-forming substances compirising a group of commercially available crude oil products which from a physicochemical point of view are characteristic of natural crude oil slicks were used in these studies. The decreases in surface tension of water i.e., surface pressure of the film caused by these material and by sea slicks were of the same order of magnitude. The same holds for the surface elasticity of the films formed by both types of materials [5]. To characterize the elastic properties of the film supplementary Langmuir through measurements were performed using the surface tension-time relatioship by means the procedure and set-up proposed by Loglio *et al.* [16, 17], and a novel sampler-elastometer was used to determine "in situ" artificial sea slicks [18].

In nature sea surfaces are often non-uniform. Such composite surfaces consisting of thick oil spills with "holes" filled with a surface-active material can also contain floating solid particles, bubbles or droplets of a third fluid. The composite dilational modulus of such a surface depends on the structure and wetting properties of the components in a complex way [19, 20], that should be borne in mind while interpreting any remote sensing data based upon the smoothing effect of the sea

surface due to the surface film. It is intended that the review presented in this paper may serve as a general overview and provide a guide to what is currently possible and what is being developed for future use.

2. Ultrasound scattering from a wind-driven water surface and its statistical features

The scattering of light, radio and acoustic waves by the sea surface depends on the slope distribution, either directly, as in the case of "specular point" scattering [21], or indirectly via tilting and hydrodynamic effects, as in the case of large-angle Bragg diffraction scatter [22]. Certainly, laser backscatter from the ocean surface is caused not by Bragg resonant reflection but by local specular reflection from surfaces (facets) on the small-wave structures that are oriented near normal to the incident laser propagation vector [11]. The same applies to high-frequency acoustic scattering [23, 24].

The scattering coefficient may be defined as the ratio of the received intensity when the acoustic wave is reflected by the surface under study to the received intensity when the wave is reflected in the specular direction by a plane surface [25]. Since the scattered waves are essentially planar over the receiver aperture their intensity is determined from acoustic pressure measurements, and assuming a linear dependence between the output voltage U of the hydrophone and the acoustic pressure the limiting scattering coefficient for a very rough surface (so-called high-frequency scattering) is given by Eq (15) in [2], and is related to the insonified surface area A, angle of incidence δ, and the mean-square slope of the wind-generated surface which can be derived from the omnidirecitional wave height spectrum $S(f)$ [26].

In the extreme cases for a very rough surface, there is only slight variation in scattered signal amplitudes with angle of incidence as the scattered field is totally diffuse and closely isotropic [27]. Recent measurements of high-frequency spectra of nd waves using a wave-following laser surface slope meter have been reported by ANT [10]. These results show that such spectra follow an $1/f$ law to a good proximation. It should be noted that the modulation spectra of the ultrasonic nal (10 MHz) specularly scattered from a wind-driven surface studied in ind-wave tank by the author [1] follow the same frequency dependence.

To sum up, the modulation spectrum of the specular scattering coefficient (see [2]) nerely linearly related to, and can be transformed into, a sea wave slope spectrum $k^2S(f)$, [8]). The relationship between the ocean wave spectra and the (radar or ustic) image spectra (i.e., the transfer function) is still not satisfactory determined The modulation spectra of the differential scatter examined in the previous nor's papers [2, 3] are derived from the spectra of low-frequency (1–40 Hz) olitude voltage fluctuations of the ultrasonic signal (10 MHz, acoustic wavelength .15 mm) specularly scattered from a wind-created surface of clean water $U_0(f)$ and ered with an oil substance film $U_c(f)$:

$$S_0(f)/S_c(f)=[U_c(f)/U_0(f)]^2 . \tag{2.1}$$

surface due to the surface film. It is intended that the review presented in this paper may serve as a general overview and provide a guide to what is currently possible and what is being developed for future use.

2. Ultrasound scattering from a wind-driven water surface and its statistical features

The scattering of light, radio and acoustic waves by the sea surface depends on the slope distribution, either directly, as in the case of "specular point" scattering [21], or indirectly via tilting and hydrodynamic effects, as in the case of large-angle Bragg diffraction scatter [22]. Certainly, laser backscatter from the ocean surface is caused not by Bragg resonant reflection but by local specular reflection from surfaces (facets) on the small-wave structures that are oriented near normal to the incident laser propagation vector [11]. The same applies to high-frequency acoustic scattering [23, 24].

The scattering coefficient may be defined as the ratio of the received intensity when the acoustic wave is reflected by the surface under study to the received intensity when the wave is reflected in the specular direction by a plane surface [25]. Since the scattered waves are essentially planar over the receiver aperture their intensity is determined from acoustic pressure measurements, and assuming a linear dependence between the output voltage U of the hydrophone and the acoustic pressure the limiting scattering coefficient for a very rough surface (so-called high-frequency scattering) is given by Eq (15) in [2], and is related to the insonified surface area A, angle of incidence δ, and the mean-square slope of the wind-generated surface which can be derived from the omnidirecitional wave height spectrum $S(f)$ [26].

In the extreme cases for a very rough surface, there is only slight variation in scattered signal amplitudes with angle of incidence as the scattered field is totally diffuse and closely isotropic [23]. Recent measurements of high-frequency spectra of wind waves using a wave-following laser surface slope meter have been reported by PLANT [10]. These results show that such spectra follow an $1/f$ law to a good approximation. It should be noted that the modulation spectra of the ultrasonic signal (10 MHz) specularly scattered from a wind-driven surface studied in a wind-wave tank by the author [1] follow the same frequency dependence.

To sum up, the modulation spectrum of the specular scattering coefficient (see [2]) is merely linearly related to, and can be transformed into, a sea wave slope spectrum ($=k^2S(f)$, [8]). The relationship between the ocean wave spectra and the (radar or acoustic) image spectra (i.e., the transfer function) is still not satisfactory determined [9]. The modulation spectra of the differential scatter examined in the previous author's papers [2, 3] are derived from the spectra of low-frequency (1–40 Hz) amplitude voltage fluctuations of the ultrasonic signal (10 MHz, acoustic wavelength = 0.15 mm) specularly scattered from a wind-created surface of clean water $U_0(f)$ and covered with an oil substance film $U_c(f)$:

$$S_0(f)/S_c(f)=[U_c(f)/U_0(f)]^2 . \tag{2.1}$$

The mean differential specular scatter $\langle DSC\rangle$ $(=20 \log [\langle U_c(f)\rangle/\langle U_0(f)\rangle]$ can be expressed in decibels in terms of the signal recorded at the receiver $\langle U\rangle$ (averaged over each run).

The authors' main concern being the estimation of the relative levels of the acoustic forward specular scatter in the film-covered water surface region, none of the transmission losses inherent to ocean sound propagation, namely geometric spreading and absorption, have been taken into account. Refraction and reflection at the oil-water interface are also neglected since the film thickness is small compared to the incident wavelength.

The principal characteristics of the scattered acoustic signal fluctuations i.e. the autocorrelation functions, the magnitude of signal amplitude variability and the form of the probability density function (p.d.f.) of signal distribution, depend on the value of the Rayleigh parameter R_a defined for specular scattering [6]:

$$R_a = 2k_a h \cos\delta, \tag{2.2}$$

where $k_a = 2\pi/\lambda$ — the wave number of an acoustic wave of length λ, h — the rms surface wave height.

The value of R_a also determines the statistics of the scattered signal. At small R_a ($R_a \ll 1$) the statistical distribution of amplitudes is Gaussian, at large ($R_a \gg 1$) and intermediate values of R_a, the generalized Rayleigh–Rice distribution, gamma, three-parameter lognormal distributions, etc. were postulated [27, 28]. The variety of p.d.f.s observed in many laboratory and field experiments results from the different character of the water wave motion in each case, as suggested by CLAY *et al.*, [29].

A good approximation of the experimental distribution of acoustic returns is obtained by expanding the Gaussian function $p_n(U)$ into a Gram–Charlier series taking into account statistical moments up to the fourth one. The p.d.f. polynomial function has the form [30]:

$$p(U) = p_n(U)\left[1 + \frac{A_1}{6} H_3(z) + \frac{A_2}{24} H_4(z) + \ldots\right], \tag{2.3}$$

where $p_n(U)$ — the Gaussian distribution, $\langle U\rangle$, U — the mean and temporal signal amplitudes, σ — the standard deviation, $z = [U - \langle U\rangle]/\sigma$ — the normalized random variable, $H_3(z) = z^3 - 3z$ and $H_4(z) = z^4 - 6z^2 + 3$ — Hermite polynomials, $A_1 = \mu_3/\sigma$ — the asymmetry coefficient (skewness), $A_2 = (\mu_4/\sigma) - 3$ — the flattening coefficient (kurtosis), μ_3, μ_4 — the third and fourth central statistical moments.

Parameters A_1 and A_2 describe in a regular way the deviations of the experimental distribution from the normal one, in which values of $\langle U\rangle$ and σ are introduced from the experimental data. The fluctuation coefficient η is a measure of signal amplitude variability and is defined as follows [6]:

$$\eta = \sigma/\langle U\rangle. \tag{2.4}$$

The statistical parameters $\langle U^2\rangle$, η, A_1, A_2 were chosen for further considerations.

3. Acoustic system and surface film characterization

Laboratory acoustic scattering experiments were performed in a small wind-wave flume described in detail elsewhere [1, 31]. In this paper we are largely concerned with very low stream speeds ($V=1-4$ m/s), for which the flow is aerodynamically smooth, i.e. the thickness of the viscous sublayer [26] exceeds the characteristic height of the surface waves for V below 4 m/s [32].

The scattering measurements were carried out for tank surfaces covered with films of commercially available crude oil products: Diesel oil, light engine oils (Extra 15, Selectol and Hipol 15), a heavy gear oil Lux.

Surface pressures of the monolayers under study were ranging from 3.4 to 4.7 mN/m, that was measured using a Wilhelmy plate method [33] directly through the window in a roof of the flume.

Each monolayer of a film-forming substance has certain viscoelastic rheological surface properties characterized by surface pressure P (a drop of water surface tension due to the film's presence, dilational elasticity modulus E ($=-A_0(dP/dA_0)$, where A_0 is the film area), and a structural diffusion parameter ω_d [4]. The magnitude of E depends only on the chemical nature and concentration of the substance composing the film, whereas ω_d is governed by the kinetics and mechanism of the rearrangement process which takes place within an insoluble monolayer during compression/expansion cycles [4].

These parameters were determined in the supplementary Langmuir through measurements by means of the surface pressure-time relationship applying the procedure and experimental set-up proposed by Loglio *et al.* [16, 17], for methodology details see [2, 3]. The surface parameters of oil films studied in this experiment are already collected in Table 1 of Refs. [1, 31].

The acoustic system applied in laboratory studies is based on high-frequency (10 MHz) and forward specular geometry scattering as described in detail elsewhere [1, 31].

The fluctuations of the scattered signal voltage amplitude peak value U are statistically analyzed using a computer IBM-aided system by means of a Statgraphics (ver. 5.0) program by Statistical Graphics Corporation. The p.d.f of the distribution was determined on the basis of 10.240 counts sorted out into 41 amplitude channels.

Studies of the effect of an artificial oil slick on the statistics of ultrasonic signals scattered from a rough sea surface were carried out in October 1989 on the Baltic Sea from aboard an oceanographic platform about 200 m off Oksywie under calm sea conditions ($V_{10}=1.7-2.3$ m/s).

The acoustic system — a free drifting, lightweight buoy — has already been applied in remote sensing and monitoring of polluted sea waters [14, 15], and has the same technical features (driving frequency, scattering geometry, data sampling and processing) as used in the laboratory studies.

It should be pointed out that the occurrence of floats can affect conditions of surface wave generation, result in non-uniform film coverage, and produce an additional turbulent flow over the surface screened by the floats as discussed in [2].

Open-sea scattering measurements were performed on a clean water surface and sea surface covered with films of different petroleum derivatives. Three crude oil products: gear oil Selectol, Gasoline 94, and Ethyline spread from hexane solutions were selected as artificial model film-forming materials in open-sea studies. The viscoelastic parameters characterizing artificial sea slicks were simultaneously measured during each acoustic scattering run using a novel film sampler-surface elastometer [18], to provide "ground truth" for the proper interpretation of the results recovered from remote acoustic surface probing.

4. Results and discussion

Figure 1 presents examples of the p.d.f. plots as a function of normalized random variable z, at different air stream speeds measured for a clean water surface in a wind-wave tunnel. The distributions are of very particular form different from that predicted by the theoretical Gaussian or Rayleigh functions. Although, it has been already found that the experimental points in the case of all both the film-coated and clean water surfaces are much closer to the Rayleigh curve than to the Gaussian one, in which values of $\langle U \rangle$ and σ emerge from the experimental data, as confirmed by the X^2 goodness of fit test by the author [14]. It is in agreement with the results of numerous authors [27, 29].

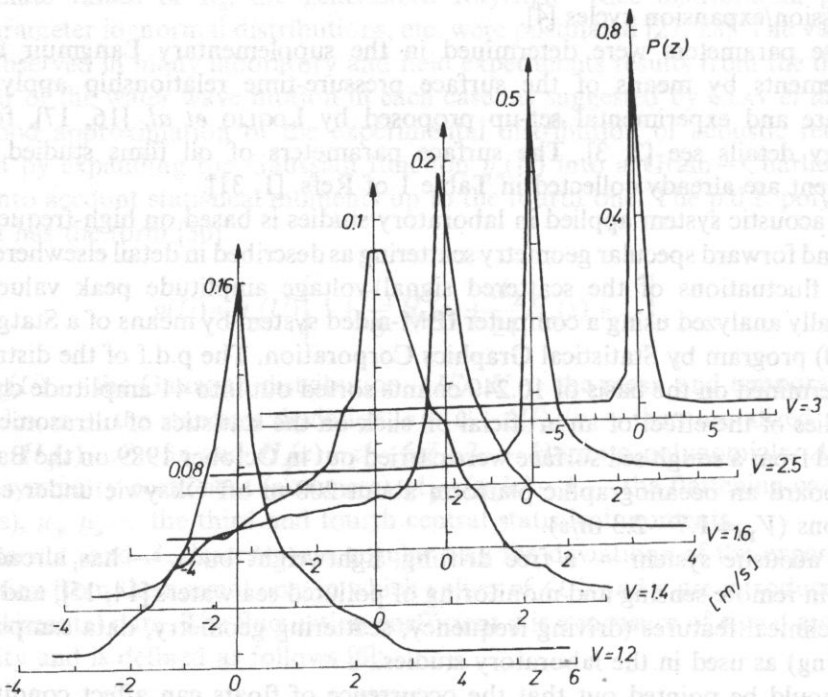

Fig. 1. Evolution of the p.d.f. plots, for a clean water surface as a function of normalized random variable z at different air stream speeds. Laboratory data.

The dependences have sole sharp maxima with wide wings and possess a large left-hand asymmetry. As V increases, a width of the distribution decreases and at the same time a height of the peak grows as well as a left-hand asymmetry is intensified (negative and increasing values of A_1). The effect is apparently related to a particular shape change of water waves being capillary ripples in a small water tank.

It is interesting to note that recent studies on statistics of very large amplitude echoes known as radar sea spikes performed using a ultra-wideband (4 GHz carrier frequency) radar in a wave tank have demonstrated very similar features (see Fig. 7 in [34]). The probability distributions of radar echo power are very peaked (the values of η are of the order of $3-6$) with a longer tail at the high value end. The statistics of open ocean radar sea spikes have been documented empirically as a function of wind speed for both fully-developed and random sea being associated with steep and breaking wave crests [35]. This similarity between the sea spikes and ultrasonic scatter distributions offers an additional argument for a strong dependence of the registered echo on curvature of particular small-scale water waves, and also suggests specular scatter as a dominant mechanism in these experiments in question [34].

In contrast, let us consider exemplary p.d.f.s obtained in at-sea experiments at low wind speeds ($V_{10}=1.7-2.3$ m/s) and depicted in Fig. 2. All the dependences exhibit two distinctly separated local maxima that means they consist of two overlapping each other distributions. This feature seems to support a model of a wavy sea surface of two-spatial scale structure irregularities assuming capillary ripples present on tilted faces of long gravity waves [26]. The film's presence leads to the sharpening of the distribution if compared to the clean reference case but a general shape remains unchanged. It can be noticed that the right-hand maximum for the light oil product (Ethyline) is higher whereas for the havier one (Selectol) the opposite situation is observed. A more detailed interpretation of the observed phenomena awaits precise and direct information on the wavy water surface shape.

Figure 3 presents the mean squared signal voltage amplitude $\langle U^2 \rangle$ as a function of wind speed, for wavy clean water and film-coated water surfaces obtained in laboratory conditions. The scattered power decreases with the wind speed, corresponding to the specular point scattering [36]. In contrast, at large incident angles the backscattered power increases with the wind speed as predicted by the Bragg scattering model [22], that is illustrated in [37], for instance. Higher values of $\langle U^2 \rangle$ for film-coated surfaces if compared to the clean surface reference case, exhibit the smoothing effect of wind waves by surface films attributed to the Marangoni phenomenon. Its strength depends on the ratio (dilational elasticity/surface pressure of the film i.e., E/P) as already discussed in [1]. This ratio is ranging from 2.1 (Hipol) to 4.1 (Selectol).

The mean differential scattering coefficient $\langle \mathrm{DSC} \rangle$ as a function of wind speed, for several oil substance-coated water surfaces again studied in laboratory conditions is presented in Fig. 4. The $\langle \mathrm{DSC} \rangle$ dependence increases continuously as wind speed increases in the range $1.3-3.5$ m/s. It suggests that the most convenient wind speed range for further at-sea applications of such a system would lie at rather higher V_{10} where values of $\langle \mathrm{DSC} \rangle$ are of the order of $10-15$ dB but under the limiting V_{10} ($\cong 7$ m/s, [26]) indicating breaking of wind waves and consequently film disruption.

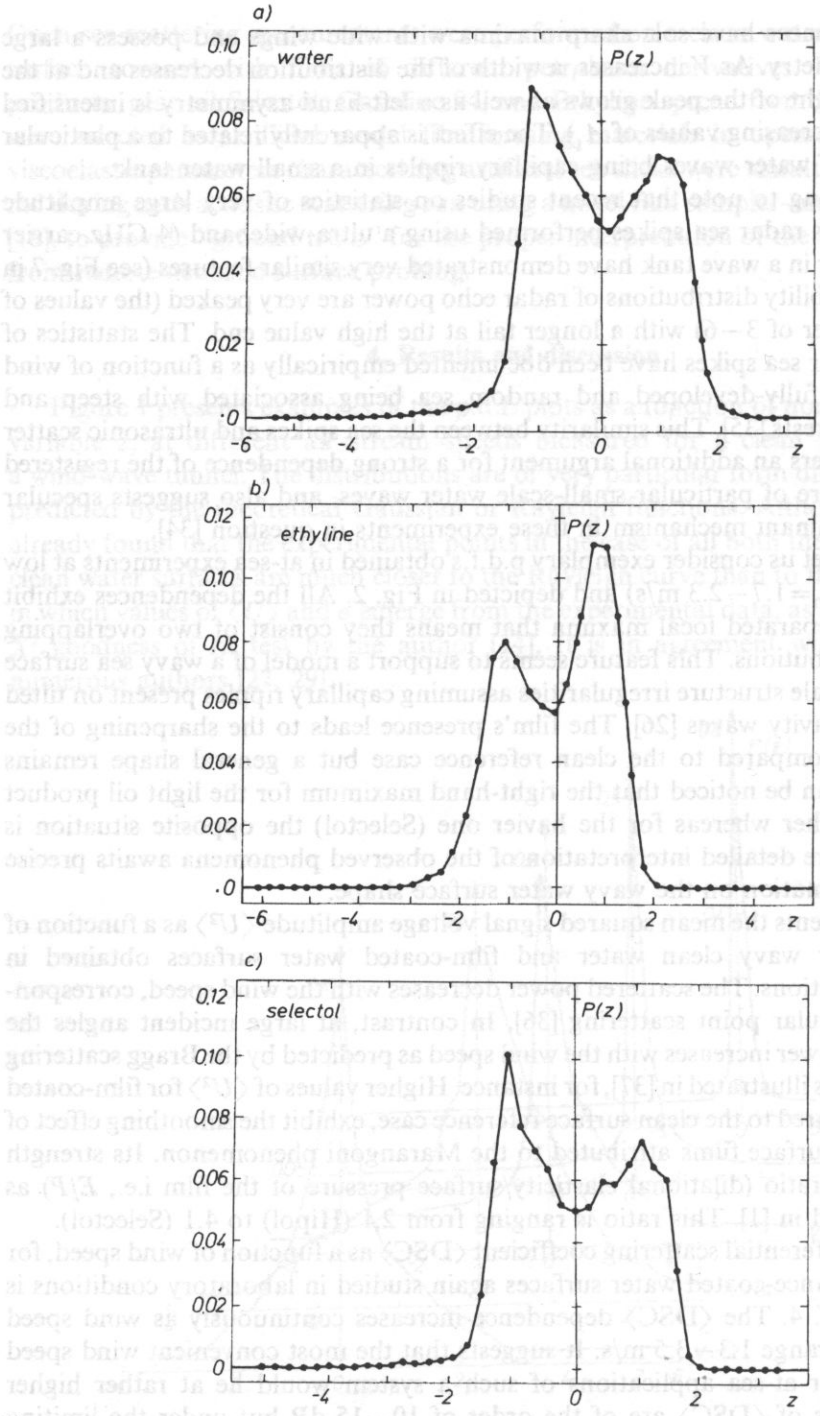

Fig. 2. Exemplary p.d.f.s. for clean (*A*), Ethyline (B), and Selectol (C) covered water surfaces. At-sea experiment data.

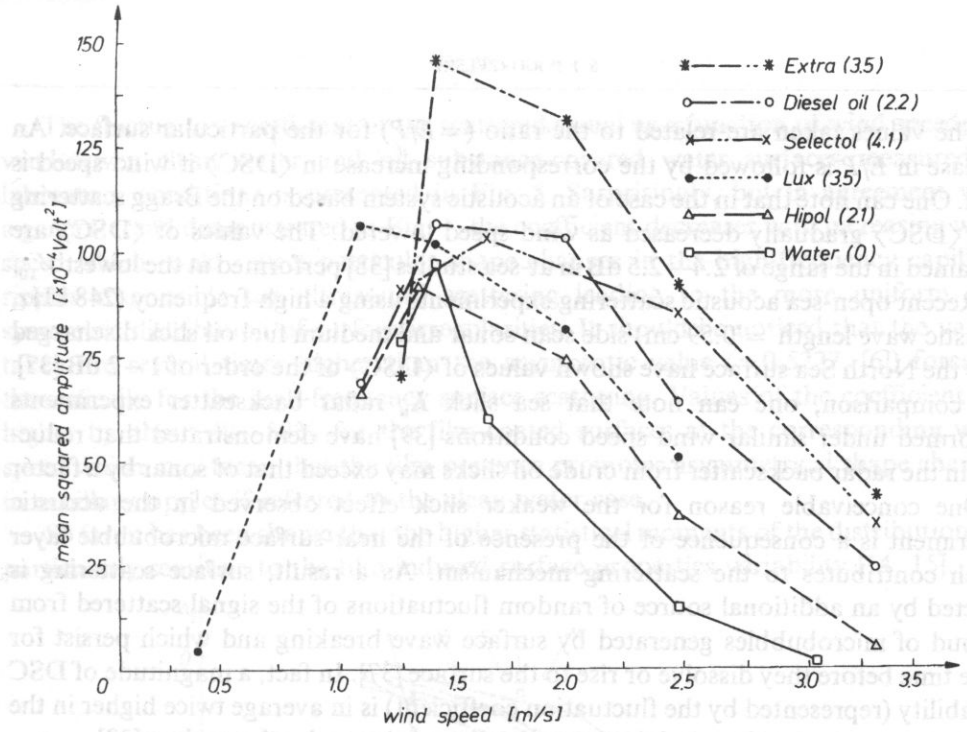

Fig. 3. Mean squared amplitude $\langle U^2 \rangle$ of the ultrasonic signal scattered at a wind-driven surface of clean water and covered with oil substance films versus air stream speed. The ratio E/P of each film is given in brackets. Laboratory data.

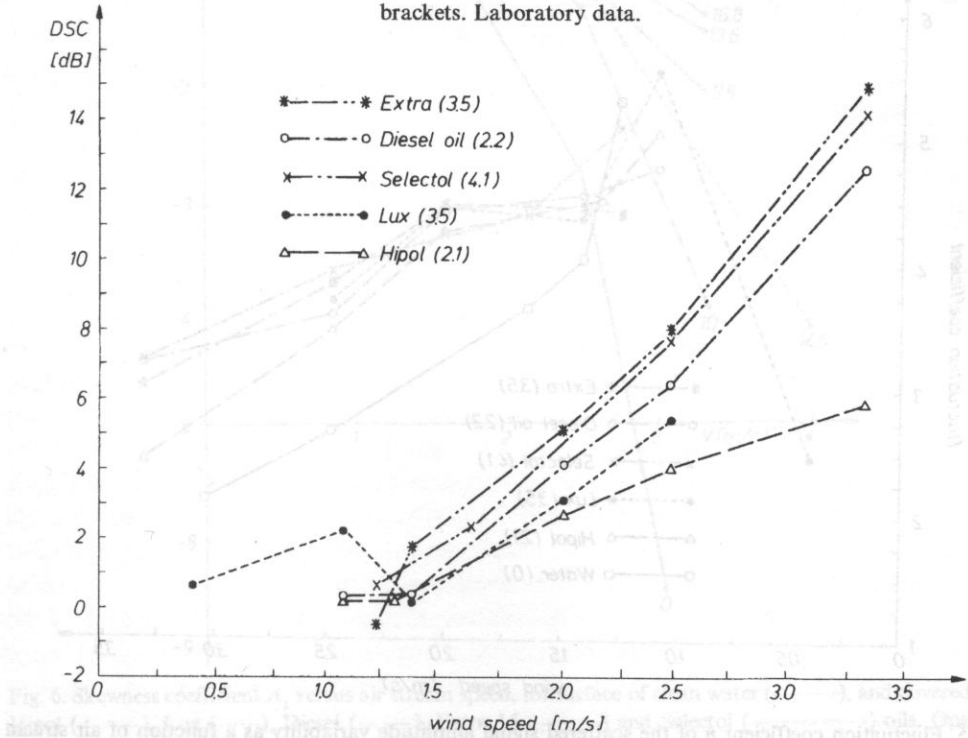

Fig. 4. Mean differential scattering coefficient $\langle DSC \rangle$ as a function of air stream speed. Denotations as in Fig. 3. Laboratory data.

The values taken are related to the ratio ($=E/P$) for the particular surface. An increase in E/P is followed by the corresponding increase in $\langle DSC \rangle$ if wind speed is fixed. One can note that in the case of an acoustic system based on the Bragg scattering [37], $\langle DSC \rangle$ gradually decreased as wind speed lowered. The values of $\langle DSC \rangle$ are contained in the range of $2.4-2.5$ dB in at-sea studies [38] performed at the lowest V_{10}.

Recent open-sea acoustic scattering experiments using a high-frequency (248 kHz, acoustic wave length = 0.59 cm) side scan sonar and medium fuel oil slick discharged onto the North Sea surface have shown values of $\langle DSC \rangle$ of the order of $1-2$ dB [37]. For comparison, one can note that sea slick K_u radar backscatter experiments performed under similar wind speed conditions [39] have demonstrated that reduction in the radar backscatter from crude oil slicks may exceed that of sonar by a factor 5. One conceivable reason for the weaker slick effect observed in the acoustic experiment is a consequence of the presence of the near-surface microbubble layer which contributes to the scattering mechanism. As a result, surface scattering is affected by an additional source of random fluctuations of the signal scattered from a cloud of microbubbles generated by surface wave breaking and which persist for some time before they dissolve or rise to the surface [37]. In fact, a magnitude of DSC variability (represented by the fluctuation coefficient) is in average twice higher in the open-sea experiment than in laboratory studies as shown by the author [38].

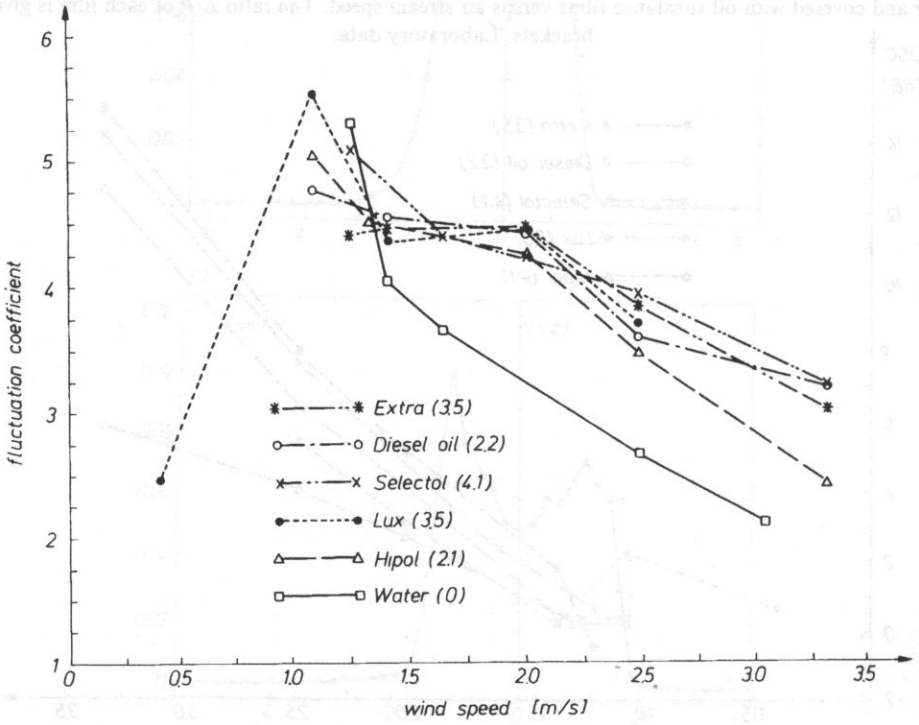

Fig. 5. Fluctuation coefficient η of the scattered signal amplitude variability as a function of air stream speed. Denotations as in Fig. 3. Laboratory data.

The fluctuation coefficient of the scattered signal as a function of wind speed, for wind-driven clean water and oil substance-covered water surfaces measured in laboratory conditions is presented in Fig. 5. Surprisingly, but in agreement with a general trend demonstrated in Fig. 1, the coefficient decreases with increasing wind speed which could reflect particular shape changes in the high-frequency capillary ripples responsible for ultrasound scattering leading to the more uniform and symmetric distribution of surface irregularities. It should be noticed that the values taken are several times higher than the asymptotic value ($=0.5227$, [6]) foreseen theoretically for the high-frequency surface scattering. Values of the coefficient are higher by about $40-50\%$ for the film-coated surfaces at the corresponding wind speed which may mean that the film presence promotes asymmetrical shape changes in capillary ripples if referred to the clean water case.

So far, it has been shown that the higher statistical moments of the distribution are particularly sensitive to the film-induced surface properties variability [14, 15].

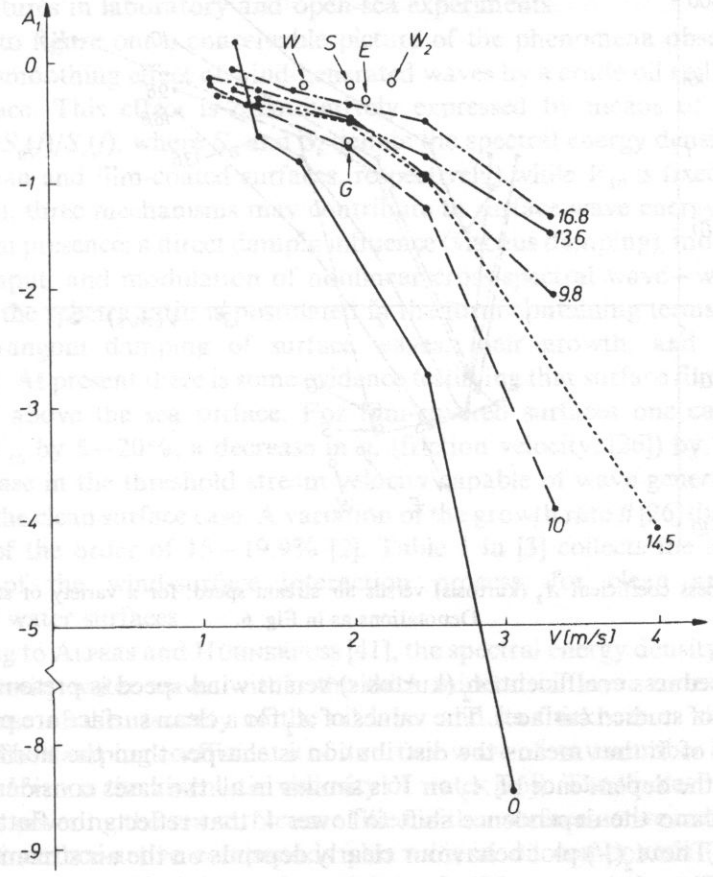

Fig. 6. Skewness coefficient A_1 versus air stream speed, for surface of clean water (———), and covered with Hipol (– – –), Lux (·····), Diesel (– · –), Extra 15 (—·—·—) and Selectol (———··———) oils. Open-sea experiment data points: clean sea water (W), contaminated sea water (W_2); sea water covered with Gasoline 94 (G), Ethyline (E), and Selectol (S) films. The film elasticity modulus E is given for each film.

Figure 6 presents the asymmetry (skewness) coefficient A_1 as a function of V for clean and film-coated water surfaces. For all speeds, the coefficient has negative values that means that the distribution has a strong left-hand asymmetry if compared to the normal reference one, in which values of $\langle U \rangle$ and σ are introduced from the experiment data. An increase in V intensifies a left-hand asymmetry ($| A_1 |$ grows). The presence of an oil film symmetrizes the distribution (the values of A_1 are higher and closer to zero for the covered surfaces, while the air speed is fixed). The difference between the curves for the control and film-coated surfaces evidently depends on the film elasticity modulus E (given in the end of each curve), and increases with increasing E.

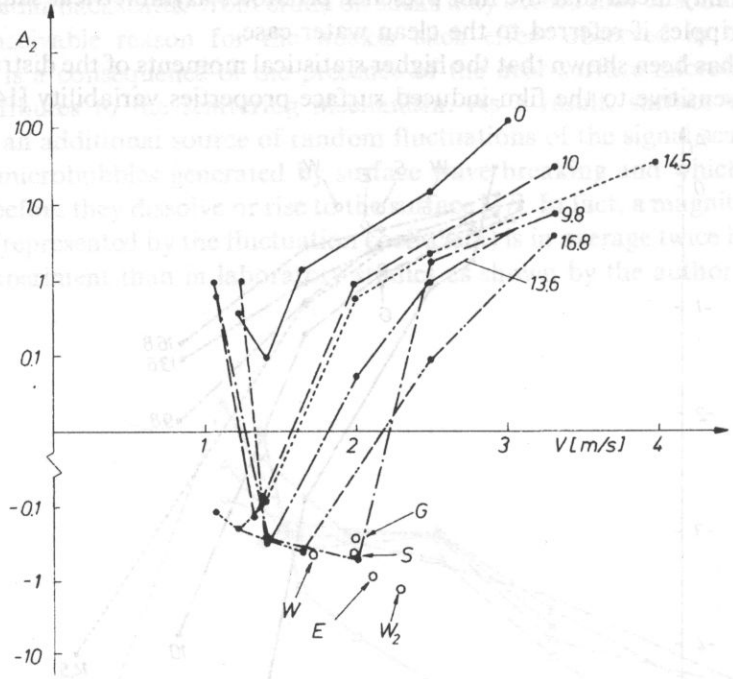

Fig. 7. Peakedness coefficient A_2 (kurtosis) versus air stream speed, for a variety of studied surfaces. Denotations as in Fig. 6.

The peakedness coefficient A_2 (kurtosis) versus wind speed is presented in Fig. 7, for a variety of studied surfaces. The values of A_2 for a clean surface are positive in the whole range of V that means the distribution is sharper than the normal one. The character of the dependence of A_2 on V is similar in all the cases considered. The film presence leads to the dependence shift to lower V that reflects the flattening of the distribution. The $A_2(V)$ plot behaviour clearly depends on the air stream speed range in question. There is a range of V where A_2 is negative. A width of this region expands with an increase of E. The curves minima are shifted to higher V with increasing E of the covered surfaces.

The assumption that the experimental distribution can be approximated by the polynomial function according to Eq. (2.3) seems to be very rough. Since absolute values of both A_1 and A_2 are lower than 1 only in the lowest speed range, thus for stronger winds the statistical moments of higher orders than the fourth one should be included in order to reproduce the distribution in a more representative form.

Figures 6 and 7 also contain data points corresponding to the open-sea experiment. They are located very close to the laboratory dependences which reflects selfconcidence of both scattering experiments and suggests that artificial sea slicks formed films of comparable elasticity moduli ranging from 9.8 to 16.8 mN/m as laboratory-studied surfaces did. In fact, the values of E for artificial sea slicks determined "in situ" were equal to 7.1 mN/m (Ethyline 94), 9.2 mN/m (Gasoline), 15.1 mN/m (Selectol), and 9.4 mN/m (contaminated sea water region). Moreover, it seems that capillary ripples responsible for high-frequency scattering have similar statistical features in laboratory and open-sea experiments.

In order to figure out a conceivable picture of the phenomena observed, let us consider the smoothing effect of wind-generated waves by a crude oil spill floating on the sea surface. This effect is quantitatively expressed by means of the relative spectrum ($=S_0(f)/S_c(f)$, where S_0 and S_c denote the spectral energy densities of wind waves for clean and film-coated surfaces, respectively) while V_{10} is fixed [5].

In general, three mechanisms may contribute to surface wave energy dissipation due to the film presence: a direct dampig influence (viscous damping), modification of wind-wave input, and modulation of nonlinear cross-spectral wave–wave interactions. In [3], the spectra ratio is postulated in the form containing terms responsible for the Marangoni damping of surface waves, their growth, and spatial film homogeneity. At present there is some evidence testifying that surface films transform a wind field above the sea surface. For film-covered surfaces one can notice an increase in V_{10} by 5–20%, a decrease in u_* (friction velocity, [26]) by 7–9%, and a large increase in the threshold stream velocity capable of wave generation [40] in reference to the clean surface case. A variation of the growth rate β [26] due to the film presence is of the order of 15–19.9% [2]. Table 1 in [3] collects the aerodynamic parameters of the wind-surface interaction process, for clean and different film-covered water surfaces.

According to ALPERS and HÜHNERFUSS [41], the spectral energy density of capillary and short gravity water waves within the thick mineral oil layer zones is modified mainly because of the viscosity of the oil layer and its thickness as shown by the author [42]. The damping coefficient α of a surface wave of wavenumber k follows the k^2 law ($\alpha=4\,k^2\nu$, ν is the kinematic viscosity of water [26]). The "holes" between the thick patches covering the sea surface are filled with a surface-active material and/or a mixture of surface-active compounds plus mineral oil compounds (Hühnerfuss, personal communication). Such surface-active substances are always encountered in crude oil as "impurities" or detergent additives in engine oils, in particular in "weathered" crude oils. Crude oil spills drifting on the sea surface do not consist of

pure hydrocarbon fractions but they contain considerable amounts of surfactant-type materials which are being formed by photo-oxidation processes and bacterial decomposition [43]. They tend to spread very easily from the thick oil spill centers over the surrounding sea surface. Only within the sea surface area covered with these monomolecular organic films surface tension gradients and thus the Marangoni wave damping can be induced in a rough surface. The result is the resonance-like behaviour of the damping coefficient α as a function of surface wave frequency f. The $\alpha(f)$ dependence attains a maximum in the frequency range 3 – 20 Hz i.e., for capillary and short gravity waves, depending on the elastic properties of the spread film [5, 41]. The relative spectrum is postulated in terms of the film viscoelasticity (E and ω_d parameters), and the film homogeneity represented by the film filling factor F [3].

It has been found for natural films that F appears to be a linear function, as a first approach, of wind speed V_{10} [44]. It is believed that artificial crude oil films follow the same $F(V)$ pattern as naturally-formed ones do. The modulus E playing a principal role in the intensity of the damping effect is often assumed to be single-valued. In nature, sea surface films experience high surface pressure variations of the order of 12 – 14 mN/m, that leads to the formation of multilayers and phase transitions within the film, and is accompanied by a steep rise in the elasticity modulus E. It would appear that the aforementioned assumption can lead to a wrong result if introduced to the Marangoni damping relation.

As a consequence, two zones exhibiting different mechanisms of wave attenuation can be specified within a mineral oil spill.

The properties of surface in dilation and compression, as expressed by their dilational moduli E, have so far been studied only for uniform homogeneous surfaces. In real systems, however, surfaces are often non-uniform. Such composite surfaces can contain floating particles, bubbles or droplets of a third phase. Floating solid particles in fluid-fluid interfaces will interact with one another if they have an irregular wetting perimeter which disturbs the smoothness of the interface. Any deformation of this system (liquid surface covered with "rough-edged" solid particles) will be resisted, and this leads to finite values of E even in the total absence of a surfactant [19, 20]. Thus the anticipated dilational modulus is of the order of the surface tension multiplied by the square of the ratio between the roughness amplitude and particle size. For the simplest case of non-interacting floating particles, the smaller the fraction of the interface which is not covered with particles, then the larger is the perceived modulus of the entire interface. For a more complicated system with solid particles, which can cover a variable area, the particle will adopt a position in a fluid-fluid interface which is determined by its contact angle ϑ. While the range of contact angles for natural particles in seawater is not known yet, the advancing contact angles for various other substances have been reported [45], and include Teflon (98 – 112°), polyethylene (88 – 103°), paraffin (110°), TFE-methanol telomer wax (100 – 160°) and human skin (90°). It may be concluded that the presence of partially-wetter ($\vartheta < 180°$) spherical particles can either increase or decrease the apparent modulus of the whole surface [20]. Thus, when the contact angle is close to

90° or when the ratio between the modulus E (surface without particles) and surface tension T of the air-liquid interface is small, there will be an increase.

The effect of contact angle on the composite modulus is illustrated in [20], and on the basis of a number of assumptions (number of particles per $mm^2 = 50$, particle radius = 50 μm) at $\vartheta = 90°$, an increase by 60% of the composite modulus is predicted where $E/T = 0.1$.

For oil droplets in air-water interfaces, when easily extensible droplets emerge into the surface, we find for the composite modulus a sudden decrease. This decrease is more pronounced when the area covered with the droplets is larger. It seems likely that capillary interaction plays a large and underestimated role in the various interfacial systems what should be borne in mind while interpreting any remote sensing data based upon the smoothing effect of the sea surface due to the Marangoni damping. Several ideas presented above are in agreement with studies of EBUCHI *et al.*, [46]. They have concluded that fine structures of short wind waves surfaces (a 3-dimensional rhombic structure, a train of capillary waves on the forward face with wavelengths gradually decreasing with distance from the crest, and a streaky structure on backward face in the direction of the wind) are not symmetrical with the wind direction but are the main contributor to high-frequency scattering. In the specular point scattering model the normalized cross section is proportional to the probability density of surface slope normal to the incident direction. Usually, the distribution of the surface slopes is assumed to be the Gaussian one, which may no longer be valid for the mentioned surfaces. So there is still a great need for research to understand signatures of the ultrasound specular scatter at "real" sea water surfaces.

Further conceivable sources of the discrepancy between the acoustic data and theoretical predictions may be related to the simplified model of the air-sea interaction commonly adopted but neglecting the surface drift effect on the wind wave growth, parasitic capillary and instability waves (known as "cat's paws") which increase more rapidly than regular waves and are expected to roll up and to form breakers at very modest steepness [47, 48].

In addition, nonlinear interactions can affect the shallow-water spectrum of wind waves. The offshore frequency spectrum is bimodal with peaks at swell f_1 and sea f_2 frequencies, whereas the observed shallow-water spectrum has additional peaks at frequencies corresponding to harmonics $2f_1$, $2f_2$, $3f_1$... and combination tones f_1+f_2, $2f_1+f_2$, f_1+2f_2... of the deep-water swell and sea [49]. As a result, the relative spectrum may not be a smooth function of frequency.

It may be helpful to add that the applied directional ultrasonic system consisting of two transducers based on a forward specular scattering geometry has two features of significant importance in future applications at sea [1, 2], and can provide far better resolution in studies of small spatial scale air–sea interaction processes taking place at the sea surface than radar and may be more convenient and less costly to use.

5. Conclusions

In general, the scattered ultrasonic signal signatures can be explained in the framework of the "specular point" scattering theory applicable also to laser and microwave surface probing.

The signal distributions are of very particular form that differ significantly from any of the standard functions (Gaussian or Rayleigh). So, for stronger winds the statistical moments of higher orders than the fourth one should be included in the Gram – Charlier series.

As V increases, a width of the distribution decreases and at the same time a height of the maximum grows that is apparently related to a particular shape change of water waves being capillary ripples in a small water tank. Moreover, the fluctuation coefficient decreases with increasing winds that points to a more uniform or symmetric distribution of surface irregularities. Although, the values of η are higher by about 40 – 50% for the film-coated surfaces, while the wind speed is fixed, which may mean that the film presence promotes asymmetrical shape changes in capillary ripples in reference to the clean surface case.

In contrast, all the distributions registered in open-sea experiments exhibit two distinctly separated local maxima that means they consist of two overlapping each other distributions. This feature seems to support a commonly accepted model of a wavy sea surface of two-spatial scale structure irregularities assuming capillary ripples present on tilted faces of long gravity waves.

The smoothing film effect expresses itself in the wind speed dependences of $\langle \mathrm{DSC} \rangle$. The particular values taken are related to the ratio E/P (elasticity modulus/surface pressure of the film), and an increase in E/P is followed by the corresponding increase in $\langle \mathrm{DSC} \rangle$.

The presence of an oil film symmetrizes the distribution the values of A_1 are higher and closer to zero for the covered surfaces in reference to the clean surface case, and leads to the flattening of the distribution (the values of $|A_2|$ are lower for the coated surfaces) at the fixed V. The difference between the wind speed dependences of A_1 and A_2 for the control and film-coated surfaces depends on the film elasticity E, and increases with increasing E.

The open-sea experiment data points are located very close to the laboratory $A_1(V)$ and $A_2(V)$ dependences which reflects selfcoincindence of both scattering experiments, suggests the same range of E taken by the artificial sea slicks, and points to the similar statistical features exhibited by capillary ripples in the laboratory and open-sea experiments.

Acknowledgments

The author wishes to thank Dr A. CHRIST (Martin Luther Universitat Halle – Wittenberg, Germany) for acoustic data computer processing. The work was supported in the part concerning characterization studies of natural films at sea by the grant BW/5200-5-0161-4 from the Polish Council for Scientific Research (KBN).

References

[1] S.J. POGORZELSKI, *Characteristics of acoustic scattering from a wind-created water surface covered with monomolecular organic films*, Dyn. Atmos. Oceans, **17**, 63–78 (1992).

[2] S.J. POGORZELSKI, *Acoustic signatures of organic films floating on the sea surface*, Arch. Acoust., **19**, 85–108 (1994).

[3] S.J. POGORZELSKI, *Ultrasound scattering for oil slicks characterization at sea*, Marine Geodesy (1994) (in press).

[4] R. CINI, P.P. LOMBARDINI, C. MANFREDI and E. CINI, *Ripple damping due to monomolecular films*, J. Colloid Interface Sci., **119**, 74–80 (1987).

[5] W. ALPERS and H. HÜHNERFUSS, *The damping of ocean waves by surface films: A new look at an old problem*, J. Geophys. Res., **94**, 6251–6265 (1989).

[6] L.M. BREKHOVSKIH, *Akustika Okeana*, Nauka, Moscow 1974.

[7] I. TOLSTOY and C.S. CLAY, *Ocean Acoustics*, Mc Graw–Hill, New York 1966.

[8] G.J. RIJCKENBERG, R. BERNARD and G. CAUDAL, *Radar measurement of directional ocean wave spectra at low incident angles*, Int. J. Remote Sensing, **13**, 2961–2974 (1992).

[9] D.P. KASILINGAN and O.H. SHEMDIN, *The validity of the composite surface model and its applications to the modulation of radar backscatter*, Int. J. Remote Sensing, **13**, 2079–2104 (1992).

[10] W.J. PLANT, *A relationship between wind stress and wave slope*, J. Geophys. Res., **87**, 1961–1967 (1982).

[11] A.J. PALMER, *Delta-k-lidar sensing of the ocean surface*, Appl. Opt., **31**, 4275–4279 (1992).

[12] S.J. POGORZELSKI, *Detection of oil-derivative contamination of water surfaces by statistical analysis of scattered acoustical signals*, J. Acoust. Soc. Am., **85**, 2383–2387 (1989).

[13] S.J. POGORZELSKI, *Statistics of underwater acoustic signals scattered by the rough water surface covered with a layer of oil substances*, Oceanologia, **27**, 45–60 (1989).

[14] S.J. POGORZELSKI, *Remote sensing of the sea oil pollution by means of high-frequency surface scattering*, Arch. Acoust., **15**, 437–446 (1990).

[15] S.J. POGORZELSKI, *The influence of crude oil spills on the sea surface on ultrasound scattering*, Oceanologia, **31**, 107–118 (1991).

[16] G. LOGLIO, U. TESEI and R. CINI, *Viscoelastic dilatation processes of fluid/fluid interfaces: Time domain representation*, Colloid Polymer Sci., **264**, 712–718 (1986).

[17] G. LOGLIO, U. TESEI and R. CINI, *Measurement of interfacial dilational properties: A software-driven apparatus*, Rev. Sci. Instrum., **59**, 2045–2050 (1988).

[18] S.J. POGORZELSKI, *Isotherms of natural sea surface films: A novel device for sampling and properties studies*, Rev. Sci. Instrum., **63**, 3773–3776 (1992).

[19] J. LUCASSEN, *Capillary forces between solid particles in fluid interfaces*, Colloids and Surfaces, **65**, 131–137 (1992).

[20] J. LUCASSEN, *Dynamic dilational properties of composite surfaces*, Colloids and Surfaces, **65**, 139–149 (1992).

[21] F.C. JACKSON, *The reflection of impulses from a nonlinear random sea*, J. Geophys. Res., **84**, 4939–4943 (1979).

[22] W.J. PLANT, *A two-scale model of short wind-generated waves and scatterometry*, J. Geophys. Res., **91**, 735–749 (1986).

[23] J.A. OGILVY, *Wave scattering from rough surfaces*, Rep. Prog. Phys., **50**, 1553–1608 (1987).

[24] G.V. BLESSING, J.A. SLOTWINSKI, D.G. EITZEN and H.M. RYAN, *Ultrasonic measurements of surface roughness*, Appl. Opt., **32**, 3433–3437 (1993).

[25] P. BECKMANN and A. SPIZZICHINO, *The scattering of electro-magnetic waves from rough surfaces*, Mc Milan, New York 1963, pp. 22–23.

[26] O.M. PHILLIPS, *The Dynamics of the upper ocean*, Cambridge University Press, New York 1977.

[27] T.K. STANTON and C.S. CLAY, *Sonar echo statistics as a remote sensing tool: volume and seafloor*, J. Ocean Engn. IEEE, **OE-11**, 79–96 (1986).

[28] C.W. HORTON, *A review of reverberation, scattering and echo structure*, J. Acoust. Soc. Am., **51**, 1049–1061 (1972).

[29] C.S. CLAY, H. MEDWIN and W.M. WRIGHT, *Specularly scattered sound and the probability density function of a rough surface*, J. Acoust. Soc. Am., **53**, 1677–1682 (1973).

[30] H. CRAMER, *Random variables and probability distributions*, Cambridge University Press, 3rd Edition, Chapter 4, New York 1970.

[31] S.J. POGORZELSKI, *Monomolecular organic film effect on wind-driven waves deduced from ultrasound scattering*, J. Acoust. Soc. Am., **90**, 965–972 (1991).

[32] H. SCHLICHTING, *Boundary-Layer theory*, Mc Graw–Hill, New York 1968.

[33] A.W. ADAMSON, *Physical chemistry of surfaces*, Wiley, New York 1982.

[34] D.B. TRIZNA, J.P. HANSEN, P. HWANG and J. WU, *Ultra-wideband radar studies of steep crested waves with scanning laser measurements of wave slope profiles*, Dyn. Atmos. Oceans, **20**, 33–53 (1993).

[35] D.B. TRIZNA, *Statistics of low grazing angle radar sea scatter for moderate and fully developed ocean waves*, IEEE Trans. Antennas Propag., **39**, 1681–1690 (1991).

[36] D.E. BARRICK, *Rough surface scattering based on the specular point theory*, IEEE Trans. Antennas Propagat., **AP-16**, 449–454 (1968).

[37] M.B. BELLOUL and S.A. THORPE, *Acoustic observation of oil slicks at sea*, J. Geophys. Res., **97**, 52165–5220 (1992).

[38] S.J. POGORZELSKI, *Ultrasound scattering from a wind-driven organic film-coated water surface*, Cont. Shelf. Res., (1993) (submitted).

[39] K.P. SINGH, A.L. GRAY, R.A. HAWKINS and R.A. O'NEIL, *The influence of surface oil on C- and K_u-band ocean backscatter*, IEEE Trans. Geosci. Remote Sens, **GE-24**, 738–743 (1986).

[40] S.J. POGORZELSKI, B. LINDE and A. ŚLIWIŃSKI, *Interrelationship between the process of surface wave generation caused by an air stream and wave attenuation process on water covered with a monolayer of crude oil derivative*, Oceanologia, **24**, 29–39 (1986).

[41] W. ALPERS and H. HÜHNERFUSS, *Radar signatures of oil films floating on the sea surface and the Marangoni effect*, J. Geophys. Res., **93**, 3642–3648 (1988).

[42] S.J. POGORZELSKI, B. LINDE and A. ŚLIWIŃSKI, *The effect of thickness of crude oil layers on the attenuation of the sufrace capillary wave,*, Oceanologia, **24**, 41–46 (1988).

[43] H. HÜHNERFUSS, W. ALPERS, A. CROSS, W.D. GARRETT, W.C. KELLER, P.A. LANGE, W.J. PLANT, F. SCHLUDE, D.L. SCHULER, *The modification of X and L band radar signals by monomolecular sea slicks*, J. Geophys. Res., **88**, 9817–9822 (1983).

[44] S.J. POGORZELSKI, A.M. STORTINI and G. LOGLIO, *Natural surface film studies in shallow coastal waters of the Baltic and Mediterranean Sea*, Cont. Shelf Res., **14**, (1994) (in press).

[45] B.D. JOHNSON and P.J. WANGERSKY, *Microbubbles: stabilization by monolayers of adsorbed particles*, J. Geophys. Res., **92**, 14641–14647 (1987).

[46] N. EBUCHI, H. KAWAMURA and Y. TOBA, *Physical processes of microwave backscattering from laboratory wind wave surfaces*, J. Geophys. Res., **98**, 14669–14681 (1993).

[47] G.H. WHELESS and G.T. CSANDY, *Instability waves on the air-sea interface*, J. Fluid Mech., **248**, 363–381 (1993).

[48] M. PERLIN, H. LIN and C.-L. TING, *On parasitic capillary waves generated by steep gravity waves: an experimental investigation with spatial and temporal measurements*, J. Fluid Mech., **255**, 597–620 (1993).

[49] S. ELGAR, R.T. GUZA and M.H. FREILICH, *Observations of non-linear interactions in directionally spread shoaling surface gravity waves*, J. Geophys. Res. **98**, 20299–20305 (1993).

ARCHIVES OF ACOUSTICS
20, 1, 57–63 (1995)

NON-INVASIVE ESTIMATION OF WALL SHEAR RATE IN HUMANS BY MEANS OF ULTRASOUND

R.S. RENEMAN*, P.J. BRANDS, S. SAMIJO AND A.P.G. HOEKS

Departments of Physiology* and Biophysics,
Cardiovascular Research Institute Maastricht
University of Limburg, Maastricht, the Netherlands

1. Introduction

In both arteries and arterioles the wall is not only subjected to pressure, acting perpendicular to the vessel wall, but also to stress tangential to the surface of the wall in the direction of flow. This shear stress, being shear rate times the local viscosity where shear rate is defined as the velocity gradient relative to the vessel radius (dv/dr), strongly influences function and structure of the endothelial cells lining the artery wall. Shear rate or shear stress makes the endothelial cells to align with flow (NEREM [8]), induces the production of, for example, endothelium-derived relaxing factor (EDRF) (RUBANYI *et al.* [11]), being nitrous oxide, and prostacyclin (FRANGOS *et al.* [3]), and activates K^+ channels (OLESEN *et al.* [9]). Most of the information about the effect of shear rate or stress on endothelial cell function has been obtained in *in vitro* studies, hampering conclusions regarding the role of shear rate or stress in vascular disorders as atherosclerosis. To obtain insights into this role of shear rate or stress, one needs to have at one's disposal a method to assess wall shear rate *in vivo*. To assess wall shear rate reliably one must be able to determine the low blood flow velocities close to the wall accurately. Accurate determination of the low, near wall velocities is hampered by contamination due to the high power signals reflected by the slowly moving artery walls. Suppression of these artery wall reflections is generally achieved by static high-pass filtering, ignoring the time-dependent aspect of these reflections. This type of filtering also eliminates the scattering as induced by the blood cells flowing at low velocity near the vessel wall.

In the present study we introduce adaptive vessel wall filtering to suppress artery wall signals while maintaining most of the flow velocity information near the artery wall, allowing the estimation of shear rate relatively close to this wall.

2. Principle of adaptive filtering

To determine the blood flow velocity distribution in a blood vessel the velocities along the ultrasound beam are generally assessed at discrete time-intervals in subsequent sample volumes as in multi-gate pulsed Doppler systems (HOEKS *et al.* [7], RENEMAN *et al.* [10]). In these systems the sample volumes are fixed in size and place. Therefore, tracking of the artery wall during its displacement in the cardiac cycle is not possible, resulting, among others, in contamination of the low velocity scattering signals near the wall by the low frequency high power reflections from the artery wall. Separation of these reflections and the scattering is difficult to achieve with static high-pass filtering, generally used in these systems, but can largely be attained with adaptive vessel wall filtering.

To be able to apply adaptive vessel wall filtering, taking into account the time-dependent aspects of artery wall reflections, the system must be able to track the artery wall. To this end the velocities along the ultrasound beam are determined more or less continuously, basically using overlapping sample volumes. The difference between regular and adaptive blood flow velocity estimation along the ultrasound beam is depicted schematically in Fig. 1. In adaptive vessel wall filtering the power of

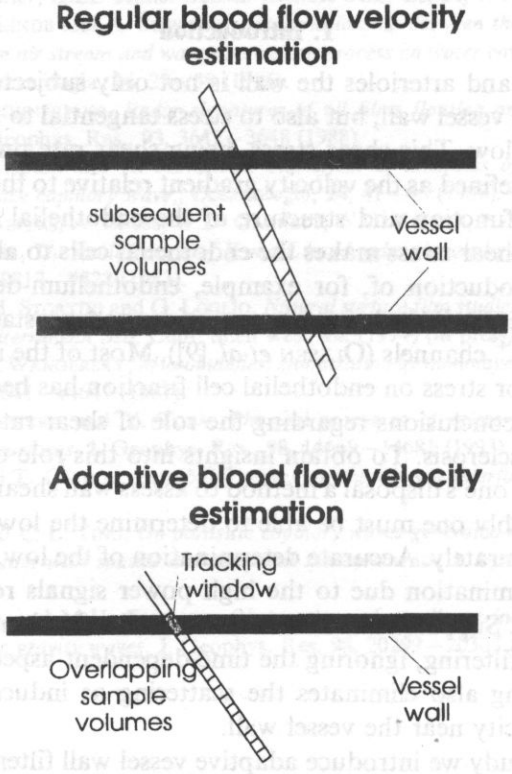

Fig. 1. Regular blood flow velocity estimation (top) and blood flow velocity estimation using adaptive vessel wall filtering (bottom).

the reflections induced by the artery wall is suppressed by shifting the temporal frequency distribution of the reflections to zero frequency, the shift being given by the estimated mean frequency of the reflected signals. Subsequently high-pass filtering with a low cut-off frequency is used to suppress the reflections centered around zero frequency; the bandpass filter apparently adapts its central frequency to the mean frequency of the slowly moving artery wall. The principle of adaptive vessel wall filtering is depicted schematically in Fig. 2. After adaptive filtering the RF signal, containing reflections, scattering and noise, is converted to a signal consisting of scattering and noise alone.

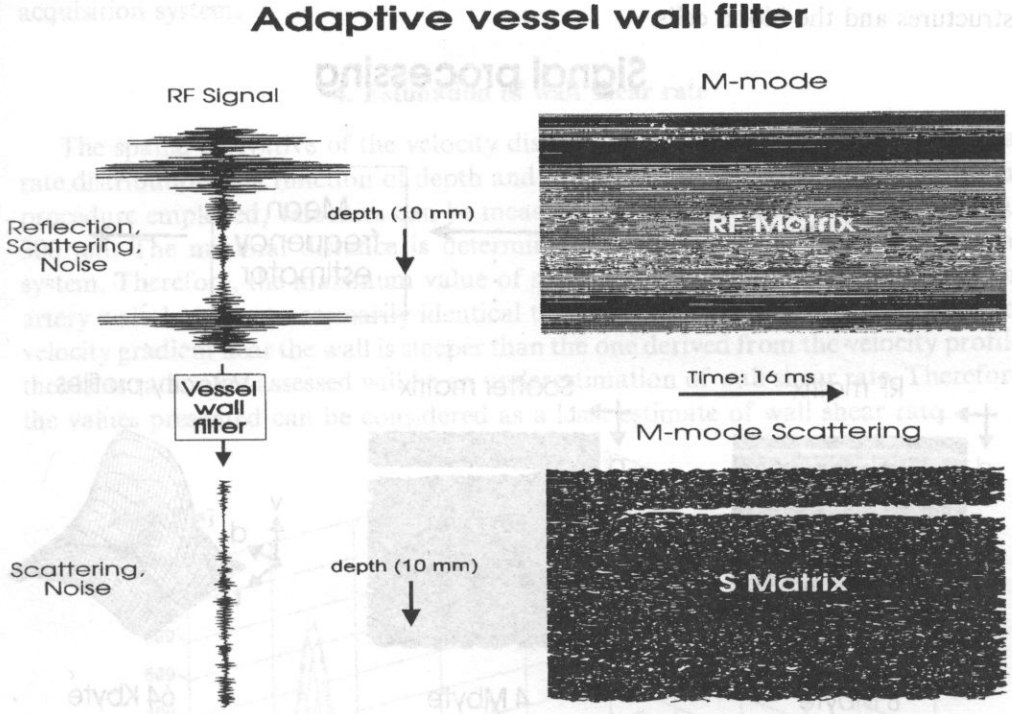

Fig. 2. Principle of adaptive vessel wall filtering.

In adaptive vessel wall filtering the cut-off frequency is fixed but can be set at a rather low value, because the centre frequency of the vessel wall signal is shifted downward to zero and the bandwidth of the vessel wall signal is marginal (all parts of the structure move at the same instantaneous speed). The main restriction for the cut-off frequency is the length of the time-window considered. A low cut-off frequency of, for example, a second order high-pass filter has the advantage that effective suppression of at least 36 dB is reached within a short frequency range. The same type of filter used in a conventional approach, where the cut-off frequency is related to the anticipated highest Doppler frequency of the wall, would require

a substantially larger transition zone, resulting in a cut-off frequency 3 octaves higher than the maximum frequency.

The mean velocity at each site in the artery is assessed off-line by means of an RF-domain velocity estimator (HOEKS *et al.* [4, 5]; DE JONG *et al.* [2]), providing velocity profiles (Fig. 3). The details of adaptive vessel wall filtering and mean velocity estimation have been described elsewhere (BRANDS *et al.* [1]). Off-line processing of the acquired RF-signals has the advantage that all the data can be retained on tape, remaining them available to test and implement new algorithms for signal processing; for example, to estimate artery wall displacement and shear rate. Moreover, the processing procedure requires sequential analysis of the velocity of the structures and the blood cells.

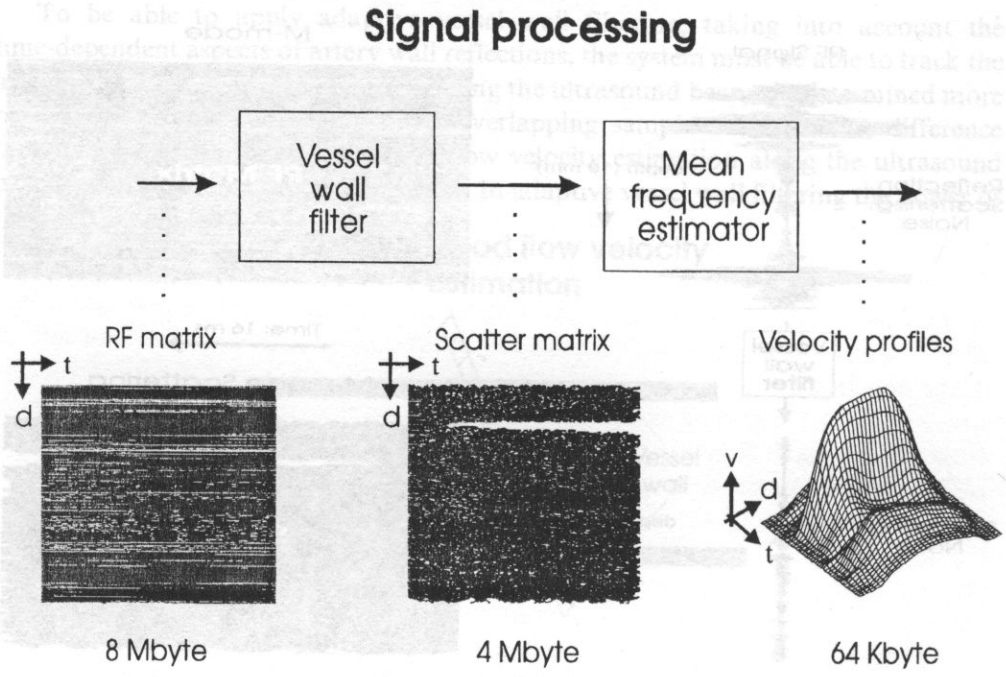

Fig. 3. Schematic representation of signal processing in the ultrasound system.

3. Measurement system

The measurements are basically performed with the M-mode of an echo system (ATL-Mark V), with an emission frequency of 5 or 7.5 MHz, connected to a data acquisition and a computer system. The acquisition system samples and stores the RF-signals in real-time. It has a sample frequency (synchronously with the emission trigger of the attached echo system) with a maximum of 50 MHz, an acquisition memory of 4 Mword (1 word is 10 bit) and a dynamic range of 60 dB (10 bit). Data

acquisition is enabled by a footswitch and starts synchronously with a trigger derived from the R-wave of an ECG-signal. The acquisition of each RF-signal received starts after a selected delay with respect to the emission trigger, allowing free selection of the range of interest. The echo system is connected to the acquisition system by three signals: 1) the RF-signal after amplification and bandpass filtering according to the quality factor of the ultrasound transducer used; 2) a trigger to indicate the moment of ultrasound transmission; 3) a sample clock synchronous with the emission trigger and with a frequency of at least four times the emission frequency ($f_S = 20$ MHz). The latter is necessary to retain the phase information in the sampled RF-signals. If the echo system does not provide the required clock signal, it can be regenerated by the acquisition system.

4. Estimation of wall shear rate

The spatial derivative of the velocity distribution in an artery provides the shear rate distribution as a function of depth and time (Fig. 4). With the adaptive filtering procedure employed, velocities can be measured as close to the artery wall as about 300 μm. The minimal distance is determined by the axial resolution of the echo system. Therefore, the maximum value of shear rate can be determined close to the artery wall, but is not necessarily identical to wall shear rate. For example, when the velocity gradient near the wall is steeper than the one derived from the velocity profile, the shear rate value assessed will be an underestimation of wall shear rate. Therefore, the values presented can be considered as a least estimate of wall shear rate.

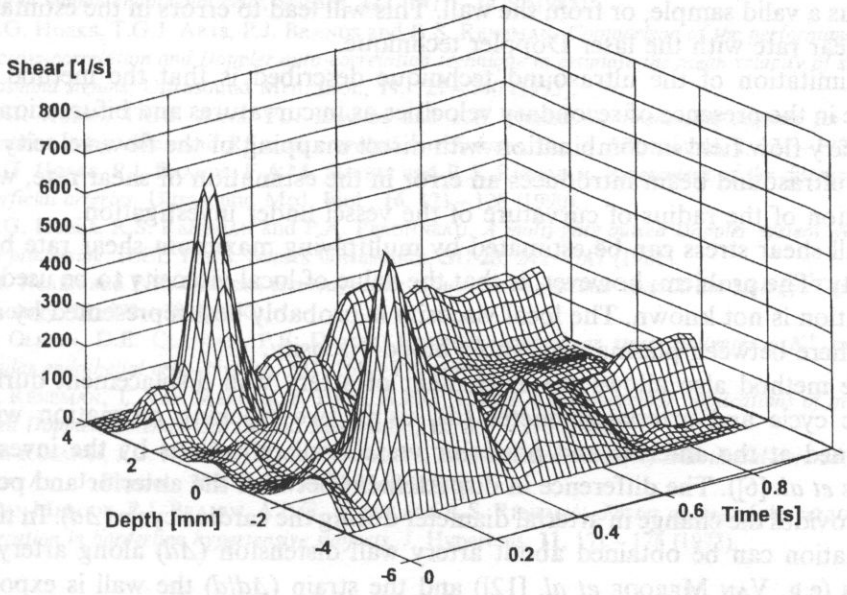

Fig. 4. The time dependent shear rate distribution as derived from the time dependent velocity distribution in the common carotid artery of a young presumed healthy volunteer.

The blood flow velocity in a blood vessel is a vector with an axial, a lateral (radial) and an azimuth component, the estimated velocity being a projection of the vectorial components on the ultrasound beam. The azimuth component may be ignored when the line of observation passes through the axis of the vessel, which is generally aimed at. The lateral component will act oppositely on the anterior and posterior sides of the lumen. Therefore, to estimate wall shear rate resulting from only the axial blood flow velocity component, shear rates at the anterior and posterior vessel walls have to be averaged.

The maximum shear rate values — the average of the anterior and posterior wall values — as found in the common carotid arteries of 5 young (aged: 18–34 years) presumed healthy volunteers ranged from 393–982 s^{-1} for center line velocities ranging from 637–1157 $mm.s^{-1}$. The coefficient of variation of 6 repeated measurements in the 5 volunteers varied between 2 and 8% (mean: 4.8%), which can be considered to be low.

An additional validation of the shear rate estimation was performed by comparing the results obtained with the ultrasound technique with those obtained with laser Doppler anemometry in an *in vitro* study using Newtonian fluid containing microspheres (10–30 μm in diameter), elastic tubing and non-stationary flow. The difference in wall shear rate as determined with the two techniques was found to be about 11% (BRANDS *et al.* [1]). This difference is surprisingly high. One explanation for the discrepancy may be that in laser Doppler anemometry signals from the slowly moving wall and the slowly moving fluid near the wall are difficult to distinguish. Therefore, it is difficult to determine whether a sample is taken from inside the tubing, and thus a valid sample, or from the wall. This will lead to errors in the estimation of wall shear rate with the laser Doppler technique.

A limitation of the ultrasound technique described is that the method is less reliable in the presence of secondary velocities as in curvatures and bifurcations. This secondary flow field in combination with direct mapping of the flow velocity vector on the ultrasound beam introduces an error in the estimation of shear rate, which is a function of the radius of curvature of the vessel under investigation.

Wall shear stress can be estimated by multiplying maximum shear rate by local viscosity. The problem, however, is that the value of local viscosity to be used in this calculation is not known. The local viscosity is probably best represented by a value somewhere between plasma and whole blood viscosity.

The method also allows the assessment of artery wall displacement during the cardiac cycle and arterial diameter (d), using two tracking estimation windows positioned at the anterior and posterior vessel wall reflections by the investigator (HOEKS *et al.* [6]). The difference in displacement between the anterior and posterior wall provides the change in arterial diameter during the cardiac cycle (Δd). In this way information can be obtained about artery wall distension (Δd) along artery bifurcations (e.g. VAN MERODE *et al.* [12]) and the strain ($\Delta d/d$) the wall is exposed to. Moreover, insight can be obtained into the relation between distension, blood flow velocity and wall shear rate, if any.

5. Conclusions

By means of adaptive vessel wall filtering velocities in arteries can be measured as close to the wall as about 300 μm, allowing the estimation of wall shear rate. The shear rate values, being the maximum value obtained, can be determined reliably in humans (coefficient of variation of 6 measurements in 5 volunteers varies from 2–8%), but is an underestimation of wall shear rate when the velocity gradient near the wall is steeper than the one derived from the velocity profile. The method described is less accurate in the presence of secondary velocities, limiting its use in arterial bifurcations.

Acknowledgements

The authors are indebted to Jos Heemskerk and Karin Van Brussel for their help in preparing the manuscript.

References

[1] P.J. Brands, A.P.G. Hoeks, L. Reneman and R.S. Reneman, *A non-invasive method to estimate wall shear rate using ultrasound*, Ultrasound Med. Biol., [in press].

[2] P.G.M. De Jong, T.G.J. Arts, A.P.G. Hoeks, R.S. Reneman, *Determination of tissue motion velocity by correlation interpolation of pulsed ultrasonic echo signals*, Ultrasonic Imaging, **12**, 84–98 (1990).

[3] J.A. Frangos, S.G. Eskin, L.V. McIntyre, C.L. Ives, *Flow effects on prostacyclin production by cultured human endothelial cells*, Science, **227**, 1477–1479 (1985).

[4] A.P.G. Hoeks, T.G.J. Arts, P.J. Brands and R.S. Reneman, *Comparison of the performance of the RF cross-correlation and Doppler auto-correlation technique to estimate the mean velocity of simulated ultrasound signals*, Ultrasound Med. Biol., **19**, 727–740 (1993).

[5] A.P.G. Hoeks, T.G.J. Arts, P.J. Brands and R.S. Reneman, *Processing scheme for velocity estimation using ultrasound RF cross correlation techniques*, Eur. J. Ultrasound, **1**, 171–182 (1994).

[6] A.P.G. Hoeks, P.J. Brands, F.A.M. Smeets and R.S. Reneman, *Assessment of the distensibility of superficial arteries*, Ultrasound Med. Biol., **16**, 121–128 (1990).

[7] A.P.G. Hoeks, R.S. Reneman and P.A. Peronneau, *A multi-gate pulsed Doppler system with serial data processing*, IEEE Trans. Sonics Ultrasonics, **SU-28**, 242–247 (1981).

[8] R.M. Neren and P.R. Girard, *Hemodynamic influences on vascular endothelial biology*, Toxicologic Pathology, **18**, 572–582 (1990).

[9] S.P. Olesen, D.E. Clapham, P.F. Davies, *Haemodynamic shear stress activates a K^+ current in vascular endothelial cells*, Nature, **331**, 168–170 (1988).

[10] R.S. Reneman, T. Van Merode, P. Hick, A.P.G. Hoeks, *Cardiovascular applications of multi-gate pulsed Doppler systems*, Ultrasound Med. Biol., **12**, 357–370 (1986).

[11] G.M. Rubanyi, J.C. Romero, P.M. Vanhoutte, *Flow-induced release of endothelial-derived relaxing factor*, Am. J. Physiol., **250**, H 1145–H 1149 (1986).

[12] T. Van Merode, P.J. Brands, A.P.G. Hoeks and R.S. Reneman, *Faster ageing of the cerotid artery bifurcation in borderline hypertensive subjects*, J. Hypertens, **11**, 171–176 (1973).

ARCHIVES OF ACOUSTICS
20, 1, 65–76 (1995)

AN EFFECTIVE ALGORITHM FOR MEASURING DIASTOLIC ARTERY DIAMETERS

A.P.G. HOEKS, XU DI, P.J. BRANDS and R.S. RENEMAN*

Departments of Biophysics and* Physiology Cardiovascular Research Institute
Maastricht, University of Limburg, The Netherlands

The assessment of the distensibility or compliance of an artery by means of ultrasound involves the determination of the instaneous change in diameter as well as the initial diamter. The change in diameter as function of time (distension waveform) can be assessed accurately using sample volumes tracking the positions of the vessel wall-lumen boundaries. However, manual positioning of these sample volumes poses specific problems related to the pulsatile behavior of the lumen diameter. Intermediate storage of rf data over a few seconds will eliminate these problems but this will limit recording time and will increase hardware complexity. A method is described to detect the wall-lumen interface synchronously with ECG allowing for automatic positioning of the sample volumes. The user interference is restricted to a rough identification of the lumen position using the envelope of the received signal. Starting from within the lumen the sample volumes are forced outward until the local envelope exceeds a threshold dynamically adjusting to the peak value of the nearby vessel wall signals. The accuracy and reproducibility of the method has been verified using tubes with various internal diameters in a water tank and repetitive measurements from the common caroid artery of young presumed healthy subjects. The results show that the proposed method is consistent with a standard deviation of 150 micrometers which is on the order of the axial resolution of the ultrasound system used.

Key words: artery diameter, distension, envelope, M-mode, rf-processing, ultrasound.

1. Introduction

Atherosclerosis changes the structure and composition of vessel walls. At a progressed state it may lead to a reduced lumen area (stenosis) and eventually to occlusion. The presence of a stenosis with a diameter reduction of more than 50% can be diagnosed reliably and non-invasively using conventional ultrasound Doppler techniques. These techniques are based on the evaluation of spectral broadening of the Doppler signal originating from the disturbed flow pattern distal to the stenosis. The detection of changes in wall structure and composition without substantial reduction in lumen area requires more refined techniques. Some of these methods are based on the notion that the local elasticity of the vessel wall may be modified by atherosclerotic changes. Moreover, the assessment of the elasticity may provide evidence about the response of the vessel wall to pharmaceutical agents administered,

for example, for treatment of hypertension. A third application of elasticity assessment may be the evaluation of the time-dependent wall tonus under the influence of neural, hormonal, and hemodynamic (wall shear stress) activation.

The compliance and distensibility of an artery have been proposed as measures for the elastic behavior of a vessel wall. The compliance C is defined as:

$$C = \frac{\partial V}{\partial p} \tag{1.1}$$

whereas the distensibility D is given by:

$$D = \frac{\partial V}{V \partial p} \tag{1.2}$$

with V the volume of an artery segment and p the blood pressure. Under the assumptions that both quantities are independent of blood pressure and that a change in volume is predominantly caused by a change in diameter rather than elongation of the vessel the above definitions may be modified to:

$$\begin{aligned} CC &= \frac{dA}{dp} \\ DC &= \frac{dA}{A_d dp} \end{aligned} \tag{1.3}$$

where A_d is the cross-sectional area at end-diastole and CC and DC are the compliance and distensibility coefficient per unit of length, respectively. Assuming a circular cross-section the CC and DC can be expressed as a function of diameter at end-diastole and the pulsatile change in diameter due to a pulsatile change in blood pressure. The latter quantity may be difficult to assess non-invasively at the site of measurement and is then replaced by a value measured nearby.

The local change in diameter as function of time (distension waveform) as well as the initial diameter can be measured non-invasively with the use of ultrasound techniques. Hokanson used a zero crossing tracking technique applied to the received radio frequency (rf) signal (Hokanson *et al.* [9]). A basic problem with this approach is that the initial selection of the signal windows is problematic. It requires positioning of windows on moving structures where the distance between the first zero-crossing within the windows at the anterior and posterior walls provide a direct measure for the time-dependent diameter. Moreover, phase interference of signals originating from closely spaced structure interfaces may cause temporary loss of a zero-crossing. In another approach the rf lines acquired in M-mode are temporarily stored and processed afterwards (Hoeks *et al.* [6], Hoeks [7]). The frozen information allows for accurate positioning of the sample windows while the type of processing employed (Doppler processing, rf correlation) reduces the sensitivity for phase interference because the mean phase of the signal within the window is considered rather than the

instantaneous phase. A disadvantage of the latter approach is the short time segment that can be evaluated (usually on the order of 5 seconds). This is insufficient to study, for example, the time-dependent changes in wall tonus.

Apparently there is a need for a processing algorithm capable to locate fast and reliably periodically the wall-lumen interface and to position the sample windows for signal processing. The procedure should require minimal user interaction, has to be rather insensitive to the signal level and should not interfere with the assessment of the change in diameter as function of time. The present paper describes a technique to establish a signal threshold, acting on the envelope of the received of the received signal at enddiastole where the rate of change in diameter is minimal, that adjusts dynamically to the signal level of the nearby walls. At the beginning of a measurement the user has to identify the lumen only once. At the start of each cardiac cycle, signaled by a trigger derived from the R-wave of the ECG, the sample windows are forced outward from the point indicated until the local envelope exceeds the local threshold, giving the initial diameter. From there the displacement detection algorithm will take over resulting in displacement waveforms for both the anterior and posterior walls while the difference between both provides the distension waveform. To ensure that always the signal from the same acoustic interface is evaluated, the sample windows track the structures using the displacement signals observed.

2. Envelope detection

The proposed algorithm for the identification of the wall-lumen interface utilizes the envelope of the rf signal. For a good contrast between wall and lumen (distinct change in amplitude level) the ultrasound beam should be aimed perpendicular to the vessel. Localization of a vessel segment of interest using landmarks as a bifurcation and proper positioning of the M-mode line is executed in 2D B-mode. A commercially available ultrasound scanner (ATL Ultramark-5), operating at 5 MHz, is connected to a real-time data-acquisition system (DAS), developed in our institute. It digitizes with a dynamic range of 8 bits the rf signal received in M-mode synchronously with the emission trigger at a sampling frequency of 20 MHz, i.e., four times the assumed carrier frequency of the ultrasound signal. To reduce the time required for data transfer from the DAS to a computer (PC486-DX2/66) the signal transfer is restricted for a preset depth range starting at a preselected delay with respect to emission. Normally the depth range would be on the order of 10 mm for peripheral vessels. For a signal with a 5 MHz carrier frequency, sampled at 20 MHz, a depth range of 10 mm corresponds with 260 samples per line.

If the rf signal has a narrow bandwidth with respect to the carrier frequency and if the signal is sampled at four times the carrier frequency a subsequent pair of sample values may be considered as a sample of a complex signal. This reduces the computation of the envelope to the square root of the sum of squares of the complex

components. For wide bandwidth signals and/or an improper ratio of sample frequency and carrier frequency the instantaneus mismatch will result in a modulation of the envelope related to the instantaneous phase of the received signal. The modulation can be effectively removed by smoothing the calculated envelope with a sliding window with a width corresponding to the axial resolution of the ultrasound system. Figure 1 depicts the calculated envelope using a smoothing over 2 periods, i.e., 8 sample points (0.3 mm). The error due to the assumptions (narrow relative signal bandwith, proper sampling frequency) is hardly visible while the computational complexity is minimal, especially if a look-up table is used for the square root of the sum of squares.

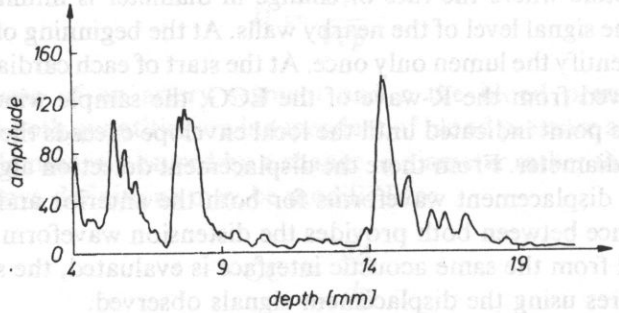

Fig. 1. The envelope of the received signal as function of depth (arbitrary offset, arbitrary amplitude) calculated as the square root of the sum of squares of a subsequent sample pair followed by a smoothing over 8 points (rectangular sliding window).

3. Vessel wall detection

Blood particles have a size considerably smaller than the wavelenght of the ultrasound in the medium and will, therefore, scatter the impinging signal in all directions (point reflector). Moreover, the impedance mismatch of blood particles and the surrounding plasma is low causing only marginal scattering. For both reasons the echogenicity of blood is low. On the other hand the layers of the artery wall of act as strong reflectors. Especially the adventitia returns a strong signal while the signal originating from the intima is considerably lower in amplitude. The media appears usually with a low intensity on a B-mode image of a high resolution system indicating the weak echogenicity of the layer. In Fig. 1 the signal from the adventitia of the anterior and posterior walls of the carotid artery of a young healthy volunteer is clearly visible. Apparently the axial resolution of the system used is too low to show the media and intima as distinct layers. The lumen has a relatively low signal amplitude but close to the anterior wall some reverberated signals can be seen. These artifacts make it difficult to identify the position of the anterior wall-lumen interface.

The echo level of the anterior and posterior walls is different due to a difference in echogenicity or a different gain setting (correction for the depth dependent attenuation). Because the absolute signal level may vary from person to person and from measurement to measurement an absolute signal threshold will be inadequate to detect the position of arterial wall signals. For correct detection the amplitude threshold should dynamically adjust to the value of a local maximum, independent of the local gain setting and intensitive to incidental reverberations or probe movements. This problem may be solved by considering the maximum within a window, with a given width, sliding over the envelope. Then starting from a point somewhere within the lumen, the first crossing in either direction of the actual envelope and a threshold, expressed as a percentage of the local maximum, will indicate the location of the wall-lumen interface. However, the selection of the window width for the determination of the local maximum needs careful consideration. If it is narrower than the lumen diameter, the local maximum may be temporarily dominated by a reverberation. On the other hand, a window width considerably larger than the artery diameter will give preference to either the anterior wall amplitude, whichever is larger. Moreover, a large number of time consuming comparisons will be involved using the sliding window approach discussed above.

Another possibility is to generate a reference signal decaying exponentially as function of depth. If the reference level falls below the current envelope it will be reset to the instataneous amplitude (sustain-attack low pass filter). In this way the reference level is always related to the last dominant echo and it will follow gradual changes in echo level along the ultrasound beam. The decay time (or response time) should be selected according to the expected maximum rate of change in gain level. For most systems this is on the order of 40—60 wavelengths, i.e., for a 5 MHz system about 10 mm. Thus only steep changes in amplitude level, considerably faster than can be explained by changes in gain setting, will be explored for wall-lumen interface detection. Short echoes of low amplitude within the lumen, possibly due to reverberations, will be ignored because they will not reach the threshold level T given as:

$$\begin{aligned} T_i &= \alpha R_i \\ R_i &= (1—2000\frac{f_s}{\beta c})\, R_{i-1} \end{aligned} \tag{3.4}$$

where c is the velocity of sound in the medium (1540 m/s)—, f_s is the sampling frequency given in MHz, i is the sampling index, β is the decay given in mm, and α the fraction (fractional threshold) to convert the reference level R to a threshold T. The parameters α and β may depend on the characteristics of the echo system used. The recursive operation for R is only executed if R_i is greater than the local envelope level (sustain), otherwise it will be set to that level (attack).

The algorithm above will be used to detect adaptively the location of the anterior wall-lumen interface. Starting from somewhere within the lumen (Fig. 2, top) the first

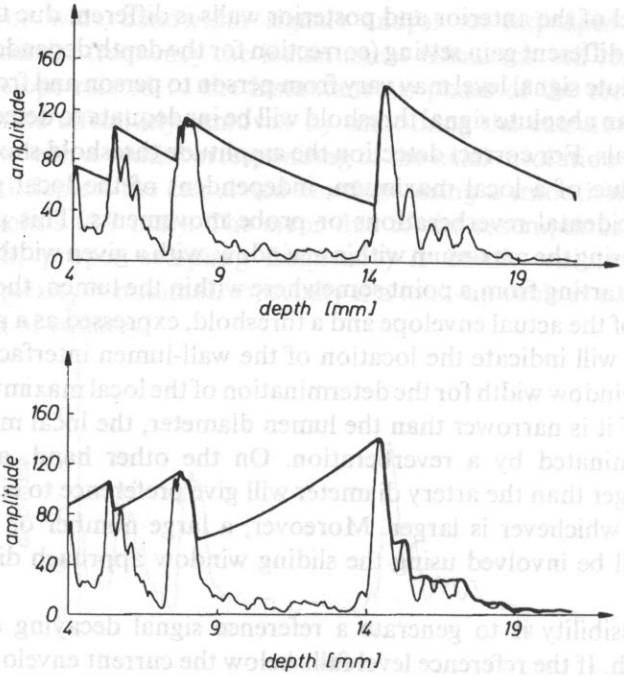

Fig. 2. The reference level (bold) as function of depth in the (top) forward and (bottom) reverse direction with a decay rate of 7 mm, superimposed on the envelope distribution. Starting from within the lumen the first crossing of the envelope and the threshold level (fraction of reference level) indicates the position of the wall-lumen interface.

crossing of the envelope and the threshold level T_i derived from the reference level R_i will signal the position of the wall. This position ought to be corrected for the resolution of the echo system because the trailing edge of the echo is considered. The algorithm will not work for the posterior wall-lumen interface because the threshold level to be applied should be independent of the anterior wall amplitude. To solve this problem a threshold level is generated in the opposite direction (Fig. 2, bottom) and the same procedure as for the anterior wall is followed. No correction is necessary for the axial resolution of the system. The estimated diameter of the blood vessel is then the distance between the detected threshold crossings corrected for the resolution of the system. Subsequently, the observation windows are positioned to track the wall positions and to estimate the wall displacement as function of time. The procedure is repeated once every cardiac cycle, triggered by the R-top of the ECG. This initialization reduces accumulating tracking errors and provides an updated estimate for the diameter on a beat-to-beat base. Of course, user interaction (identification of a point within the lumen) is only required at the start of a measurement. For the following heart beats the system will be able to select a start point based on the initial setting and the detected (accumulated) changes in wall positions.

4. Evaluation

To validate the proposed processing scheme silicon/rubber tubes with know internal diameters of 8.55, 5.70 and 3.87 mm and with a wall thickness of 1.6, 1.0 and 1.0 mm, respectively, were placed in a water tank at a distance of 2 cm from the transducer face. Measurements were carried out with a 5 MHz ATL Ultramark-5, the rf signal of which was digitized at 20 MHz. The length of the smoothing window for the envelope calculation was set at 4 sample points (1 period). The fractional threshold α was varied from 0.3 to 0.8, while the decay β was varied from 3.8 to 10.6 mm. The experimental results are depicted in Fig. 3, where the estimated diameters are plotted as function of α for different β values without correction for the system axial resolution. Each estimate given is based on the median of 5 independent measurements. It can be concluded from Fig. 3 that for a given α, a smaller decay β results in a smaller estimated diameter. The same holds for a fixed decay: a smaller fractional threshold α gives a smaller estimated diameter. Figure 3 clearly shows that the diameter estimation procedure is more sensitive to the selected threshold α than to the decay parameter β. Considering the bias in the estimate, after correction for an assumed system resolution of 0.3 mm, it can be inferred that a reasonable choice for α would be in the range of 0.5 to 0.7, while the value of the decay parameter should be on the order of the diameter of the tube investigated.

The results, as presented in Fig. 3, indicate that the bias in the estimate after correction for the resolution will be smaller than the resolution of the echo system employed. However, these results can not be used to draw conclusions about the consistency of the estimation algorithm under realistic conditions. For that purpose rf signals from the common carotid artery, about 2 cm proximal to the flow divider, of 4 young healthy volunteers were recorded and used for the evaluation of the algorithm. Eleven arbitrary files were obtained, each of them covering a time period of about 5 seconds (5 to 7 cardiac cycles). Figure 4 depicts the estimated internal diameter, based on the end-diastolic diameter of the second heart beat of file F03, as function of the fractional threshold and decay parameter. The detected diameters are consistent for α values ranging from 0.5 to 0.7 and β values ranging from 6 to 9 mm. These results are in accordance to the results obtained in the tube experiment.

In a further evaluation the parameters were set at $\alpha=0.5$ and $\beta=7$ mm and applied to all beats of all recorded files (estimation of end-diastolic diameter). The results, as listed in Table 1, indicate that the standard deviation of the estimate is on the order of 0.1 mm, implying a good repeatability and stability of the processing algorithm. However, these results can not be used to deduce a possible bias in the estimate. Moreover the observed standard deviation may also originate from true changes in end-diastolic diameter, due to a change in blood pressure level or vessel wall tonus, rather than from an error in the estimation procedure. To eliminate the

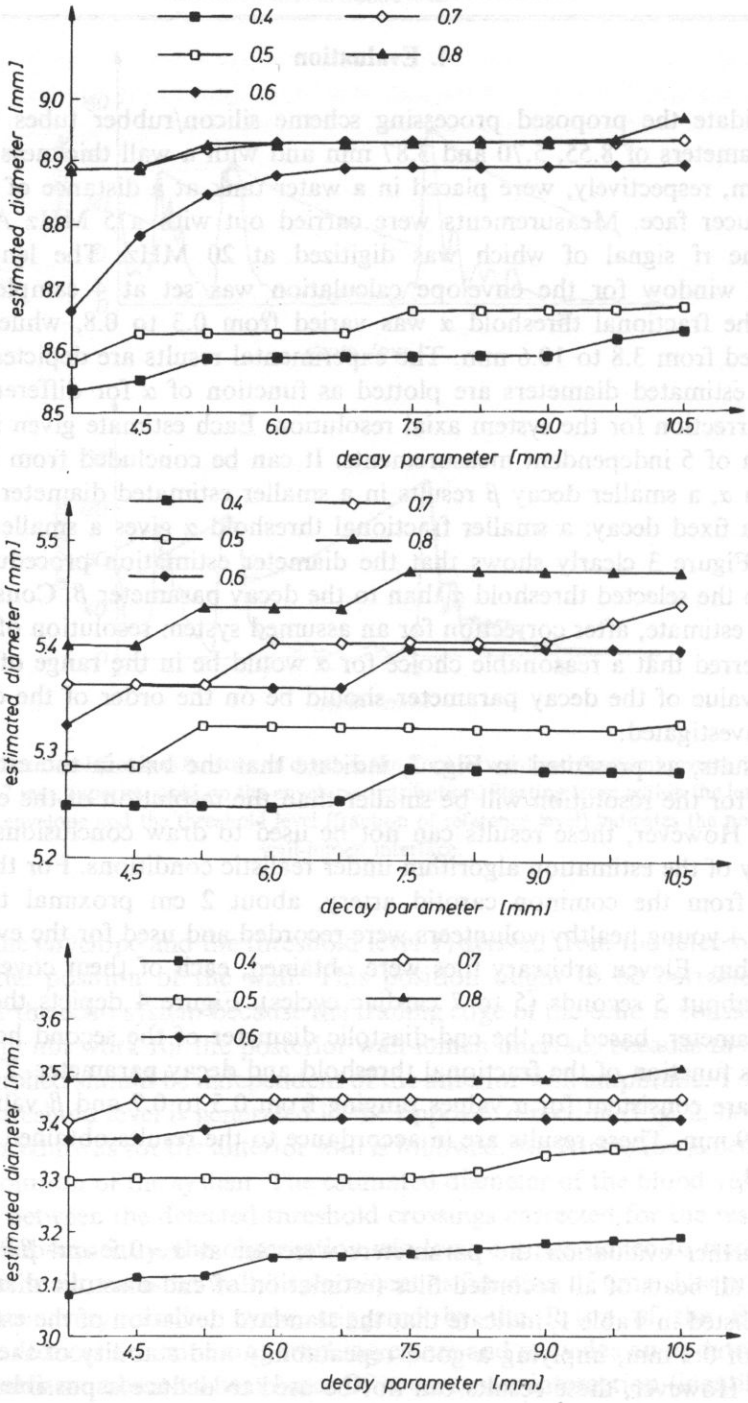

Fig. 3. The observed diameter as function of the decay parameter and the fractional threshold for a tube with an internal diameter of (top) 8.55 mm, (middle) 5.7 mm, and (bottom) 3.87 mm. The values presented are not yet corrected for the axial resolution of the echo system employed.

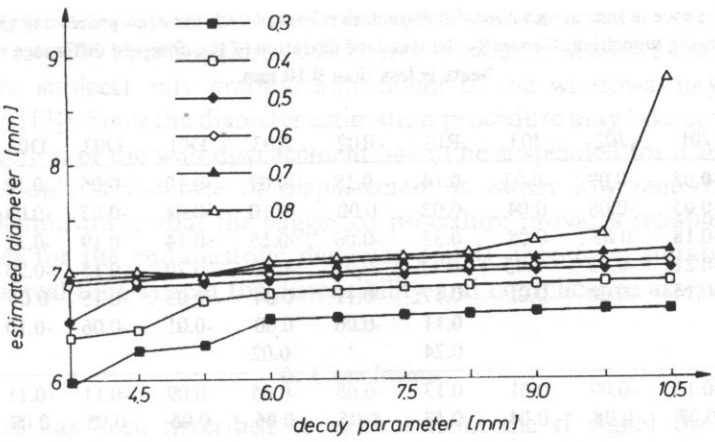

Fig. 4. The estimated diameter of the common carotid artery of a young healthy volunteer at the end of the second heart beat (file F03) as function of the decay parameter and the fractional threshold without correction for the axial resolution of the echo system.

Table 1. The estimated diameter in mm of the common carotid artery of 4 young healthy volunteers for a fractonal threshold of 0.5 mm and a decay parameter of 7.7 mm. Generally, the observed standard deviation is less than 0.15 mm. Note the minor differences for repeated measurements on the same subjects (same letter).

File	J01	J02	J03	R01	R02	R03	D01	D02	D03	F02	F03
beat	5.70	5.31	5.42	6.49	6.92	6.47	6.62	7.11	6.96	6.75	7.17
2	5.66	5.43	5.43	6.68	6.81	6.49	6.60	7.06	6.77	6.85	6.94
3	5.85	5.33	5.44	6.43	6.96	6.43	6.81	7.05	6.98	6.79	7.13
4	5.89	5.54	5.67	6.92	6.97	6.34	6.94	7.09	7.05	6.80	7.05
5	5.81	5.66	5.69	6.76	6.83	6.30	6.85	7.10	6.96	6.75	7.12
6				6.97	6.84	6.34	6.95	7.13	7.02		
7				6.99		6.45					
mean	5.78	5.45	5.53	6.75	6.89	6.40	6.79	7.09	6.95	6.79	7.08
std	0.09	0.13	0.12	0.21	0.06	0.07	0.14	0.03	0.09	0.04	0.08
max-min	0.23	0.35	0.28	0.57	0.16	0.19	0.35	0.08	0.28	0.10	0.23

latter source of error the algorithm for the detection of the wall displacement, based on cross-correlation of rf signal segments (De Jong *et al.* [3] Hoeks *et al.* [7]) was applied. Using this algorithm an estimate for the end-diastolic diameter can be derived from the sum of the initial diameter and the cumulative change in diameter over the cardiac cycle. This value is then compared to the end-diastolic value obtained with the diameter estimation algorithm. The results, listed in Table 2, confirm that the observed difference between both methods and its standard deviation are generally less than 0.1 mm, demonstrating a good repeatability and consistency of both methods. Moreover, comparing Table 2 with Table 1 reveals that the standard deviation of the estimate corrected for a possible change in end-diastolic diameter (Table 2), is indeed systematically lower than the uncorrected one (Table 1),

Table 2. The difference in mm in end-diastolic diameters observed with the echo processing (Table I) and the displacement tracking algorithm. Generally the standard deviation of the observed difference over consecutive beats is less than 0.10 mm.

File	J01	J02	J03	R01	R02	R03	D01	D02	D03	F02	F03
beat 1	-0.05	-0.09	-0.02	0.14	-0.18	-0.07	-0.10	-0.06	-0.18	-0.05	-0.38
2	-0.05	-0.08	0.04	0.02	0.00	-0.10	-0.04	-0.05	-0.04	-0.05	-0.13
3	-0.18	0.05	0.08	0.32	-0.06	-0.15	-0.14	-0.19	-0.12	0.00	-0.20
4	-0.21	-0.13	-0.05	-0.11	-0.05	-0.03	-0.20	-0.15	-0.23	0.01	0.03
5	-0.14	-0.20	0.01	0.17	-0.11	0.04	-0.05	-0.15	0.04	0.11	0.01
6				0.11	-0.06	0.00	-0.01	-0.06	-0.10		
7				0.24		-0.02					
mean	-0.13	-0.09	0.01	0.13	-0.08	-0.05	-0.09	-0.11	-0.11	0.00	-0.13
std	0.07	0.08	0.04	0.13	0.05	0.06	0.06	0.05	0.09	0.06	0.15

confirming that part of the observed random error is caused by true changes in end-diastolic diameter.

5. Discussion

Since the first reported non-invasive measurement of human artery pulsations with ultrasound (ARNDT [1]) many non-invasive studies concerning the mechanical properties of human arteries have been carried out (RENEMAN *et al.* [11]; VAN MERODE *et al.* [12]; BUNTIN and SILVER [2]; LÄNNE *et al.* [10]). The initial artery diameter was determined either by letting the user identify the wall positions using a displayed signal (HOKANSON *et al.* [9]; ERIKSEN [4]; HOEKS *et al.* [6]) or by using a fixed signal threshold to find the positions automatically (ARNDT [1] GUSTAFSSON *et al.* [5]; WILSON *et al.* [13]). Both methods have obvious drawbacks. Unless the signal is frozen, accurate manual identification of vessel wall positions is problematic, while a fixed threshold will fail if the vessel wall signal is not distinct, is too low or varies considerably over time.

The proposed detection algorithm intends to improve the diameter detection procedure in two aspects. Firstly, to provide a method that can detect the wall positions automatically on a beat-to-beat base, allowing for a continuous recording of the change in diameter as function of time. Secondly, a dynamic threshold signal is employed that adjusts its level to the level of the current signals. The only user interaction required is a rough identification of the position of the lumen at the start of a measurement. In a practical configuration a computer screen would display the envelope of the captured rf signal repetitively allowing the user to adjust the signal level and to identify the lumen. The last action starts the estimation procedure for both the internal diameter as well as the change in wall positions over time yielding the distension waveform. The diameter estimation procedure will be carried out at the start of each cardiac cycle signaled by a trigger derived from the R-wave of the ECG.

Thus every cycle the windows for the displacement algorithm will be repositioned. To reduce the possibility that the lumen will be lost (sudden transducer movements with respect to the subject) only gradual adjustment of the windows may be allowed (WILSON *et al.* [13]). Since the diameter estimation procedure may take some computer time the detection of the wall displacement has to be suspended for a short time but this happens only if the rate of displacement is rather low (end-diastole). The evaluation demonstrates that the suggested procedure provides reliable and consistent estimates for the end-diastolic diameter and is, therefore, suitable for incorporation in a real-time system for distensibility and complicance assessment.

6. Conclusion

A method has been described to extract from the rf signal the diameter of a peripheral vessel at end-diastole. The threshold level adjusts dynamically to the signal level of nearby vessel walls, making the procedure insensitive to the effects of gain setting and depth dependent attenuation. In *in vitro* and *in vivo* test measurements the proposed procedure showed a good consistency of 0.15 mm, which is on the order of the axial resolution of the ultrasound echo system used. The selection of the processing parameters (decay and fractional threshold) is not critical. The computational complexity is only moderate allowing for the incorporation of the estimation algorithm in real-time distensibility and compliance measurement systems.

Acknowledgement

This work was supported by the Technology Foundation (STW) of the Netherlands, grant MGN80.1483.

References

[1] J.O. ARNDT, *Über die Mechanik der intakten A. Carotis Communis des Menschen unter verschiedenen Kreislaufbedingungen*, Archiv für Kreislaufforschung, **59**, 153—197 (1968).

[2] C.H. BUNTIN and F.H. SILVER, *Noninvasive assessment of mechanical properties of peripheral arteries*, Annals of Biomedical Engineering, **18**, 549-566 (1990).

[3] P.G.M. DE JONG, T. ARTS, A.P.G. HOEKS and R.S. RENEMAN, *Determination of tissue motion velocity by correlation interpolation of pulsed ultrasonic echo signals*, Ultrasonic Imagining, **12**, 84—98 (1990).

[4] M. ERIKSEN, *Noninvasive measurement of arterial diameters in humans using ultrasound echoes with prefiltered waveforms*, Med. and Biol. Eng. and Comput., **25**, 189—194 (1987).

[5] D. GUSTAFFSON, H. STALE, J.A.BJÖRKMANN and G. GENNSER, *Derivation of haemodynamic information from ultrasonic recordings of aortic diameter changes*, Ultrasound Med. Biol., **15**, 189—199, (1989).

[6] A.P.G. HOEKS, P.J. BRANDS, F.A.M. SMEETS and R.S. RENEMAN, *Assessment of the distensibility of superficial arteries*, Ultrasound Med. Biol., **16**, 121—128 (1990).

[7] A.P.G. HOEKS, *Noninvasive study of the local mechanical arterial characteristics in humans*, in: The arterial system in hypertension [Eds.] M.E. Safar and M.F.O'Rourke, Kluwer Academic Publ. 1993, pp. 119—134.

[8] A.P.G. HOEKS, T.G.J. ARTS, P.J. BRANDS and R.S. RENEMAN, *Comparison of the performance of the cross corelation and Doppler autocorrelation technique to estimate the mean velocity of simulated ultrasound signals*, Ultrasound Med, and Biol., **19**, 727—740 (1993).

[9] D.E. HOKANSON, D.J. MOZERSKY, D.S. SUMNER, D.E. STRANDNESS, *A phase locked echo-tracking system for recording arterial diameter changes in vivo*, J. of Appl. Physiology, **32**, 728—733, (1972).

[10] T. LÄNNE, H. STALE, H. BENGTSSON, D. GUSTAFSSON, D. BERGQVIST, B. SONESSON, H. LECEROF and P. DAHL, *Noninvasive measurement of diameter changes in the distal abdominal aorta in man*, Ultrasound Med. Biol., **18**, 451—457 (1992).

[11] R.S. RENEMAN, T. VAN MERODE, P. HICK and A.P.G. HOEKS, *Flow velocity patterns in and distansibility of the carotid artery bulb in subjects of various ages*, Circulation, **71**, 500—509 (1985).

[12] T. VAN MERODE, P.J.J. HICK, A.P.G. HOEKS and R.S. RENEMAN, *The diagnosis of minor to moderate atherosclerotic lesions in the carotid artery bifurcation by means of spectral broadening combined with the direct detection of flow disturbances using a multigate pulsed Doppler system*, Ultrasound Med. Biol. **14**, 459—464 (1988).

[13] L.S. WILSON, M.J. DADD and R.W. GILL, *Automatic vessel tracking and measurement for Doppler studies*, Ultrasound Med. Biol. **16**, 645—652 (1990).

ARCHIVES OF ACOUSTICS
20, 1, 77–90 (1995)

ENHANCED BANDWIDTH MULTILAYER TRANSDUCERS FOR IMAGING APPLICATIONS

Q. ZHANG AND P.A. LEWIN

Biomedical Engineering and Science Institute and
Department of Electrical and Computer Engineering
Drexel University, Philadelphia, PA 19104, U.S.A

The operating frequency of the presently used PZT or PZT composite ultrasound imaging transducers is determined by the half wavelength resonance or fundamental thickness mode of vibration. This resonance frequency together with the two quarter wavelength matching layers governs the bandwidth of the transducer and hence control the overall resolution capabilities of the imaging system. This paper describes a new generation of multilayer ultrasound imaging transducers which are intentionally designed for off-resonance operation. The design makes use of the exceptionally wideband properties of the thin PVDF polymer film and offers excellent resolution. Moreover, such non-resonant design allows transducer to produce an image at virtually and clinically relevant frequency and can provide resolution tailored to clinician's needs. In addition, the design examined here offers pulse-echo sensitivity comparable to that achievable using PZT piezoceramic transducers. The design principle of the enhanced bandwidth transducer along with the transducer model specially developed to predict key electromechanical parameters of multilayer transducers is presented. These parameters include insertion loss, pulse-echo sensitivity, impulse response and electrical impedance. A few prototypes of this non-resonant tranducer design were built and tested. The experimental results were found to be in good agreement with those obtained from the computer simulations. Fundamental limitations of the design are pointed out and recommendations for future work are outlined.

1. Introduction

The use of ultrasound in clinical diagnosis has been steadily increasing in the past years. The excellent safety record of ultrasound made it a preferred diagnostic tool in the disciplines of cardiology, obstetrics and gynecology. At present, ultrasound is one of the most frequently employed clinical imaging modalities. This achievement in clinical ultrasound diagnosis can be ascribed, to a certain extent, to the constant advancements made in the transducer technology. However, while transducer design has become more and more sophisitcated., the transducer's basic operation principle remained the same. In other words, currently available ultrasound imaging transducers are all designed for operation at fundamental half wavelength resonance

frequency, which eventually sets the limitation on transducer bandwidth and hence the axial resolution of the image.

This paper presents an alternative design of ultrasound imaging transducers which operate below their resonance frequency. While the design discussed here employs a multilayer structure, it differs significantly from the designs reported in the literature [1 – 7]. Briefly, the multilayer design proposed by YAMAMIZU *et al.* [1, 2] contained two to three polymer films with alternate polarization direction and weighted thicknesses. While this approach broadened the bandwidth of a polymer transducer it also increased the two-way insertion loss [1, 2]. Several groups form United Kingdom and United States have considered folded multilayer approach, in which several identical piezoelectric layers were stacked together with alternating vibration polarity [3 – 5]. Although this approach improved the sensitivity of the transducer through a better electrical matching between the transducer and the transmitting/receiving circuits, it also decreased its resonance frequency. This is because in this construction the resonance frequency of the folded transducer is determined by the overall thickness of the stack [3, 5]. Hence, it appears that any increase in the pulse-echo sensitivity can only be achieved at the expense of the bandwidth. Other multilayer approaches involved the combination of PZT and PVDF layers [6] and the use of active matching layers [7], but all of these designs were based on a half wavelength resonant design approach and employed PZT ceramics as piezoelectric materials.

In contrast, the multilayer transducer design examined here uses multiple piezopolymer films which feature acoustic impedance close to that of the human tissue. The film layers are arranged in such a way that their polarization pattern complies with a given Barker code sequence [8]. Since the transducer operates in a non-resonant mode, it allows image to be produced at virtualy and clinically relevant frequencyl. Also, the use of PVDF polymer film provides a basis to achieve an ultrasound image with the highest possible resolution. Finally, the design analyzed here offers pulse-echo sensitivity comparable to that achievable with PZT piezoceramic transducers.

This paper presents a systematic extension of the work described in [9 – 11]. SUNG's work [9] focused primarily on the application of ultrasound pulse compression technique and hase been carried out using PZT ceramics. Also, since his transducer design required the use of a separate transmitter and receiver, the results presented were not immediately applicable in the medical imaging field. PLATTE's research [10, 11] involved development of the pulse-echo Barker code transducer which is further examined in this paper. While the work described in [10, 11] focused mainly on the experimental approach, the work presented here provides a more systematic investigation of the factors governing Barker code transducer performance. Attention is given to a systematic, step-by-step approach including design, construction and testing of the Barker code transducers. In particular, the principle of operation of the multilayer pulse-echo Barker code transducers is thoroughly explained based on the simulations obtained using specially developed transducer model. This model is

particularly suited to simulate a complex, multilayer structure in the context of medical ultrasonic imaging requirements. Key electromechanical parameters including two-way insertion loss, impulse response and electrical impedance are presented and their importance in optimizing the transducer performance is carefully discussed.

In the following, the operation principle of an alternative non-resonant transducer design is outlined together with a brief description of a transducer model developed in this work. The computer simulations of the behaviour of the switchable Barker code transducers were carried out, and the results were compared with those corresponding to the optimized PZT transducers. Based on the simulation results, several prototypes of the Barker code transducers were fabricated and tested. The experimental results are presented and compared with the data obtained from the computer simulations. Advantages and disadvantages of the proposed transducer design are also discussed.

2. Operation principle of the switchable Barker code transducers

As already mentioned, the switchable Barker code transducers presented here make use of multiple piezopolymer layers, and the polarization pattern of the layers is consistent with a given length of a Barker code sequence. Prior to the presentation of the principle of operation of the switchable Barker code transducers, a brief description of Barker code may be useful.

Barker codes are binary codes named after R.H. BARKER, who developed them for synchronization purpose in digital communication systems [8]. The maximum code length was found to be 13 and Table 1 lists the known Barker codes.

Table 1. The known Barker codes

Length of Code	Code Elements	Peak of autocorrelations
1	+	1
3	++−	3
7	+++−−+−	7
11	+++−−−+−−+−	11
13	+++++−−++−+−+	13

One of the important properties of the Barker codes is that the complementary code can be obtained by reversing the sign of every other element in the original code [10]. This feature was extremely useful in developing a pulse-echo Barker code transducer described here. Fig. 1 shows a schematic diagram of a switchable Barker code transducer. The individual piezoelectric layers are stacked according to a Barker code pattern and, for convenience, a Barker code of length 7 is used. The electronic switches connected to each piezoelectric layer are operating in the following way. During the transmitting period, the switches are set to "on" position and the resulting equivalent polarization pattern of the transducer is shown in Fig. 1b. Since each

piezoelectric layer is connected electrically in parallel and acoustically in series, the electrical impedance of the transmitter is inversely proportional to the number of active layers. This is important, because, in general, a single layer PVDF transducer exhibits high electrical impedance due to PVDF film's low dielectric constant. This high impedance prevents an appropriate electrical matching between the transducer and a driving circuit, and hence worsens the PVDF transducer's sensitivity. The use of switches in Fig. 1 improves the electrical matching and hence the transmitting sensitivity of the switchable Barker code transducer. In the receiving mode, the switches are set to "off" position, and the equivalent transducer configuration is shown in Fig. 1c. It is worth noting that since the individual piezopolymer layers are connected electrically in series during the receiving period, the transducer presents a high impedance to the receiver's input. Also, the polarization pattern of the switchable Barker code receiver mirrors that of the transmitter (see Fig. 1b, c). This lays the foundation for designing a practical pulse-echo transducer with exceptionally wide bandwidth and pulse-echo sensitivity comparable with that achievable with the currently available conventional PZT scanheads. The principle of operation of the switchable Barker code transducer can be conveniently explained by referring to Fig. 2.

When the excitation voltage is applied to the transmitter, an acoustic wave is generated in each piezoelectric layer (see Fig. 2; all layers have identical thickness). To simplify the analysis, it is assumed that the interrogated medium is linear and lossless. The generated acoustic pulses are launched into the medium with a delay governed by the propagation time of an acoustic wave through a given number of piezoelectric layers. When the transmitted waves arrive at the surface of the Barker code receiver, they sequentially generate electrical voltage in each individual piezoelectric layer in the receiving assembly. Since the polarization pattern of the receiver mirrors that of the transmitter (see Fig. 1), there will be a time, say $t=tp$, when each of the individual acoustic waves or pulses launched will reach its corresponding receiving layer. When this occurs, the voltage generated in each individual layer will exhibit the same polarity. Consequently, the output voltage produced at the terminals of the Barker code receiver will be n times larger than that generated by a single layer (see Fig. 2). At all other times, the voltage generated in each individual layer exhibits different polarity and some of the voltages are canceled out. The remaining voltages manifest themselves as ripples in the output waveform of the Barker code transducer (see Fig. 2). As a result, the sensitivity of the switchable Barker code transducer is proportional to the number of active layers, and its bandwidth is determined by the thickness of a single layer in the assembly.

In the next section, computer simulations along with a transducer model developed in the course of this work are presented. The results of the computer simulations of the multilayer assembly are compared with those corresponding to the optimized PZT transducer.

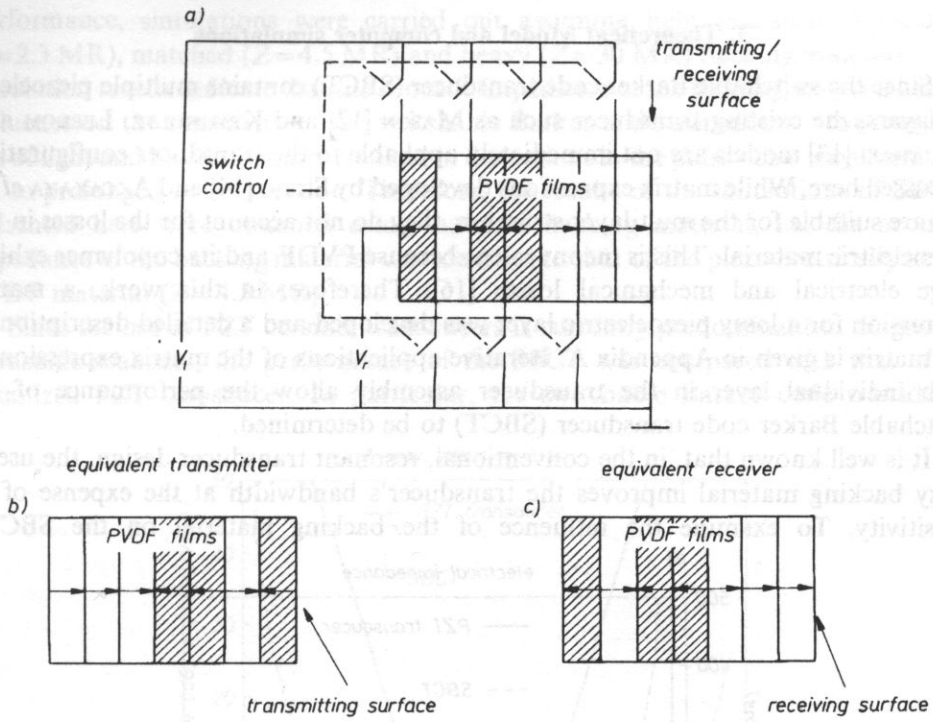

Fig. 1. A schematic diagram of a 7 layer switchable Barker code transducer SBCT. a) Switchable Barker Code Transducer; b) Equivalent polarization pattern of a SBCT transmitter; c) Equivalent polarization pattern of a SBCT receiver; → — polarization direction *Vt* — excitation voltage, *Vr* received voltage.

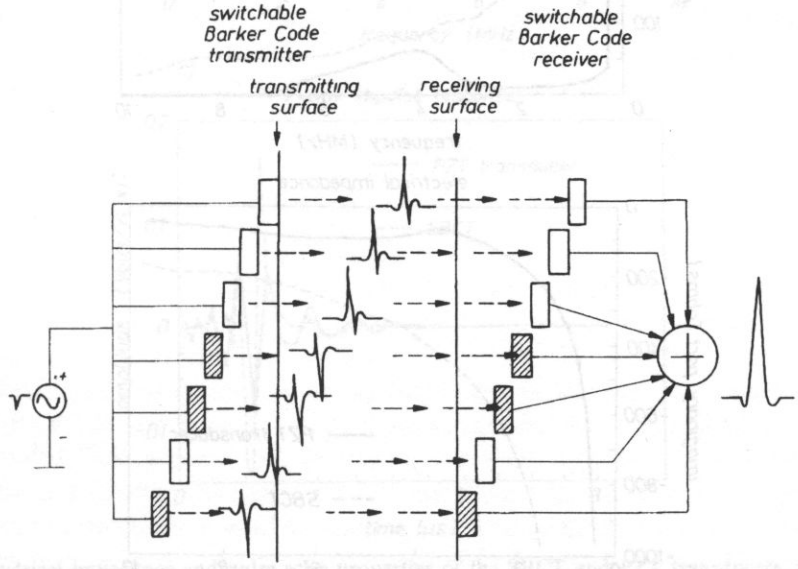

Fig. 2. Principle of operation of Switchable Barker Code Transducers SBCT.

3. Theoretical Model and computer simulations

Since the switchable Barker code transducer (SBCT) contains multiple piezoelectric layers, the existing transducer such as MASON [12] and KRIMHOLTZ, LEEDOM and MATTHAEI [13] models are not immediately appliable to the transducer configuration discussed here. While matrix expressions developed by SITTIG [14] and AKCAKAYA *et al.* [15] are suitable for the multilayer structure, they do not account for the losses in the piezoelectric material. This is inconvenient because PVDF and its copolymer exhibit large electrical and mechanical losses [16]. Therefore, in this work, a matrix expression for a lossy piezoelectric layer was developed and a detailed description of the matrix is given in Appendix A. Iterative applications of the matrix expression to each individual layer in the transducer assembly allow the performance of the switchable Barker code transducer (SBCT) to be determined.

It is well known that, in the conventional, resonant transducer design, the use of lossy backing material improves the transducer's bandwidth at the expense of its sensitivity. To examine the influence of the backing material on the SBCT's

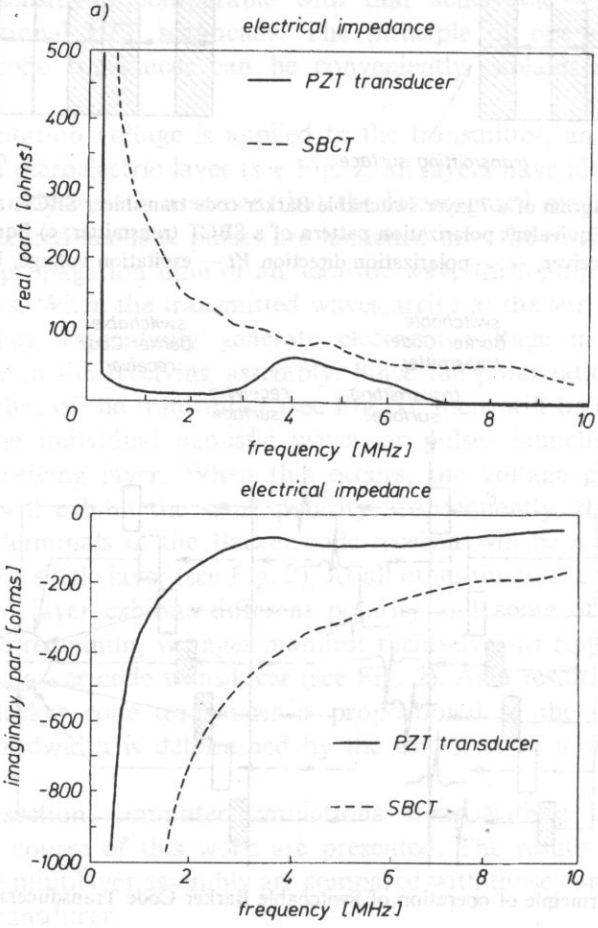

performance, simulations were carried out assuming light (acoustic impedance: $Z=2.3$ MR), matched ($Z=4.5$ MR) and heavy ($Z=30$ MR) backing materials. The simulation results indicate that the acoustic impedance of the backing material has no influence on the sensitivity of the switchable Barker code transducer. However, the use of light and heavy backings resulted in distortions in the pulse-echo waveform and led to prolonged pulse duration. Therefore, the results of the simulations of SBCTs presented here were obtained using matched backing material, i.e. the acoustic impedance of the backing material was identical to that of the piezoelectrically active PVDF material ($Z=4.5$ MR).

Since the use of PZT ceramic transducers is currently predominant in diagnostic ultrasonic scanners, the performance of the SBCT was compared with that of an optimized PZT transducer. In particular, the switchable Barker code transducer

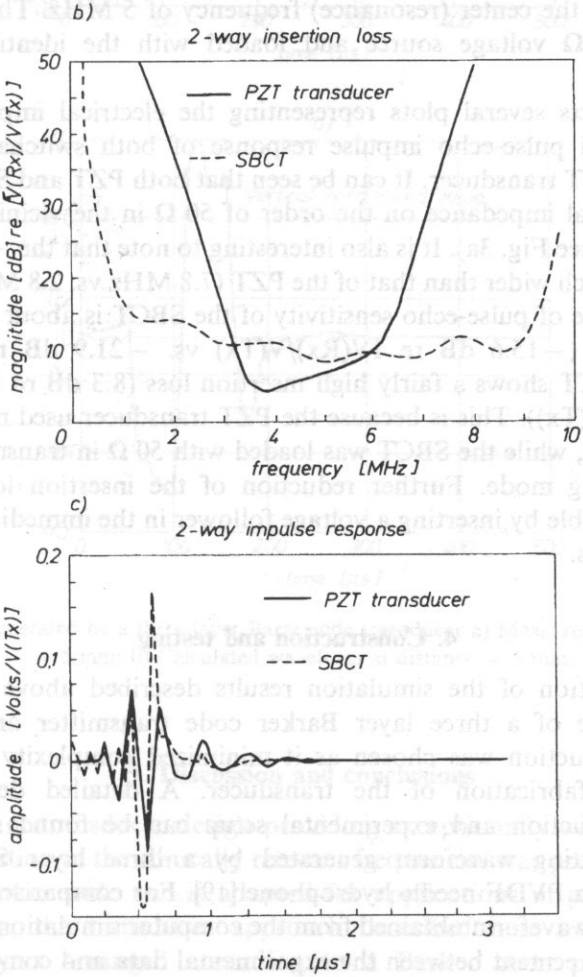

Fig. 3. Electrical impedance and pulse-echo properties of the SBCT and PZT transducers, a) Electrical impedance; b) Two-way insertion loss; c) Pulse-echo impulse response.

simulated here used eleven P(VDF-TrFE) copolymer layers, and was backed by piezoelectrically inactive P(VDF-TrFE) rod. The thickness of a single copolymer layer was 120 μm which corresponds to 10 MHz resonance frequency. It is worth noting that since the switchable Barker code transducer operates in off-resonance mode here, its corresponding center frequency is 5 MHz. In addition, the transducer simulated here was excited by a 50 Ω voltage source and terminated with a 1 MΩ resistance in receiving mode in order to maximize its pulse-echo sensitivity.

The PZT transducer simulated was air backed and used two quarter wavelength front matching layers for optimal performance. The acoustic impedance of these matching layers was chosen based on the procedure suggested in [17]. To facilitate direct comparison between the two designs considered, the PZT transducer operated at the center (resonance) frequency of 5 MHz. The transducer was excited by a 50 Ω voltage source and loaded with the identical resistance in receiving mode.

Figure 3 depicts several plots representing the electrical impedance, two-way insertion loss and pulse-echo impulse response of both switchable Barker code transducer and PZT transducer. It can be seen that both PZT and SBCT transducers exhibit an electrical impedance on the order of 50 Ω in the vicinity of the 5 MHz center frequency (see Fig. 3a). It is also interesting to note that the −6 dB bandwidth of the SBCT is much wider than that of the PZT (7.8 MHz vs. 2.8 MHz). In addition, the peak amplitude of pulse-echo sensitivity of the SBCT is about 6 dB higher than that of the PZT (−15.6 dB re 1V(Rx)/V(Tx) vs. −21.9 dB re 1V(Rx)/V(Tx); However, the SBCT shows a fairly high insertion loss (8.3 dB re 1V(Rx)/V(Tx) vs. 4 dB re 1V(Rx)/V(Tx)). This is because the PZT transducer used matched electrical loads (50 Ω, 50 Ω), while the SBCT was loaded with 50 Ω in transmitting mode and 1 MΩ in receiving mode. Further reduction of the insertion loss in the SBCT transducer is possible by inserting a voltage follower in the immediate vicinity of the piezoelectric layers.

4. Construction and testing

Initial verification of the simulation results described above was carried out using a prototype of a three layer Barker code transmitter and receiver. This three layer construction was chosen as it minimized complexity of the assembly and accelerated fabrication of the transducer. A detailed description of the transducer construction and experimental setup can be found in [18]. Figure 4 shows a transmitting waveform generated by a three layer SBCT transducer and measured by a PVDF needle hydrophone [19]. For comparison, the corresponding transmitting waveform obtained from the computer simulations is also shown in Fig. 4. A good agreement between the experimental data and computer simulations can be seen. The noise observed was traced to be due to an inadequate electrical shielding.

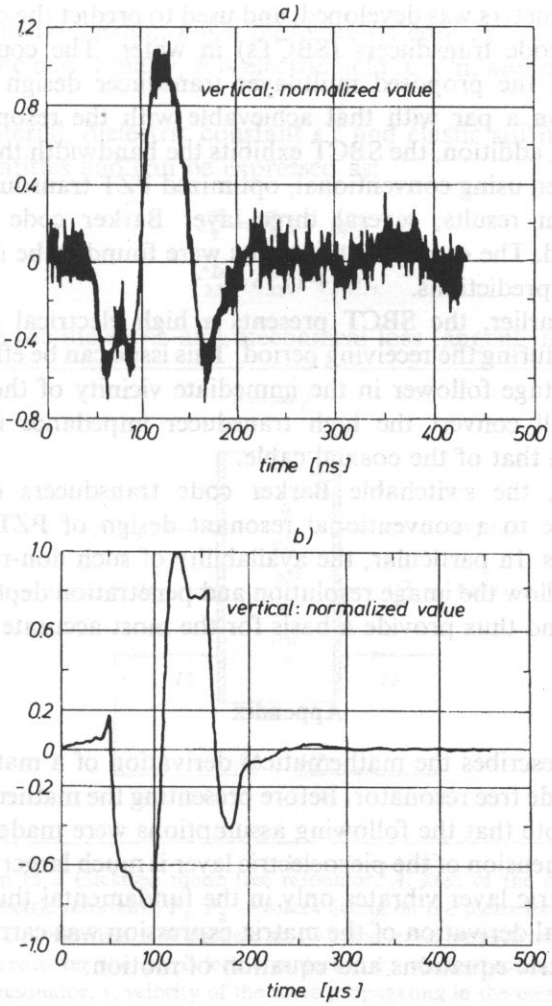

Fig. 4. Waveforms generated by a three layer Barer code transducer a) Measured waveform at distance = 5 mm; b) Calculated waveform at distance = 5 mm.

5. Discussion and conclusions

A non-resonant transducer design providing exceptionally wide bandwidth and suitable for operation at the clinically relevant frequencies was presented. The design makes use of Barker code and is adapted for applications in pulse-echo imaging. More specifically, the transducer approach described here uses multiple active piezopolymer layers arranged according to a Barker code pattern. The work presented here extended the approach published in [10, 11]. In particular, a transducer model capable to predict the transducer behaviour in terms of the relevant

electroacoustic parameters was developed, and used to predict the performance of the switchable Barker code transducers (SBCTs) in water. The computer simulation results indicate that the proposed multilayer transducer design will provide pulse-echo sensitivity on a par with that achievable with the resonant PZT or PZT composite design. In addition, the SBCT exhibits the bandwidth that is twice as large as that obtained when using conventional, optimized PZT transducers. To verify the computer simulation results, several three layer Barker code transducers were fabricated and tested. The experimental results were found to be in good agreement with the theoretical predictions.

As mentioned earlier, the SBCT presents a high electrical impedance to the associated circuitry during the receiving period. This issue can be effectively overcome by integrating a voltage follower in the immediate vicinity of the transducer. This voltage follower will convert the high transducer impedance into 50 Ω output impedance to match that of the coaxial cable.

Once optimized, the switchable Barker code transducers could provide an attractive alternative to a conventional resonant design of PZT ceramic or PZT composite scanheads. In particular, the availability of such non-resonant wideband transducers would allow the image resolution and penetration depth to be tailored to the clinical needs, and thus provide a basis for the most accurate diagnosis.

Appendix

This appendix describes the mathematical derivation of a matrix expression for a lossy thickness mode free resonator. Before presenting the mathematical derivation, it is important to note that the following assumptions were made:

1. The lateral dimension of the piezoelectric layer is much larger than its thickness.
2. The piezoelectric layer vibrates only in the fundamental thickness mode.

The mathematical derivation of the matrix expression was carried out by making use of the piezoelectric equations and equation of motion:

$$T_3 = c_{33}^{*D}\xi_3' - h_{33}D_3, \tag{A.1}$$

$$E_3 = -h_{33}\xi_3' + \frac{D_3}{\varepsilon_3^{*S}}, \tag{A.2}$$

$$-\omega^2\xi_3 = \frac{c_{33}^{*D}}{\rho}\xi_3''. \tag{A.3}$$

The prime indicates differentiation with respect to X_3 which is along the z axis (poling direction) and is normal to the plane of the active piezoelectric layer. T is the stress in N/m^2; c^D is the elastic stiffness constant in N/m^2 measured with D constant; ξ is the particle displacement in direction X_3 in meters; D is the electric flux density in the direction X_3 in C/m^2; ε is the permittivity in F/m (the product of the relative permittivity of the material and the permittivity of a vacuum, 8.85×10^{-12} F/m),

measured under constant strain; h is a piezoelectric constant of the material in N/C and is assumed to be real. Finally, E is electric field in V/m and ρ is the density of the layer in kg/m^3.

For a lossy material, dielectric constant ε^{*S} and elastic stiffness constant c^{*D} are both complex quantities and can be expressed as:

$$\varepsilon_3^{*S}=\varepsilon_3^S(1-j\phi), \tag{A.4}$$

$$c_{33}^{*D}=c_{33}^D(1+j\varphi), \tag{A.5}$$

where ϕ and φ are the dielectric and mechanical loss tangent, respectively.

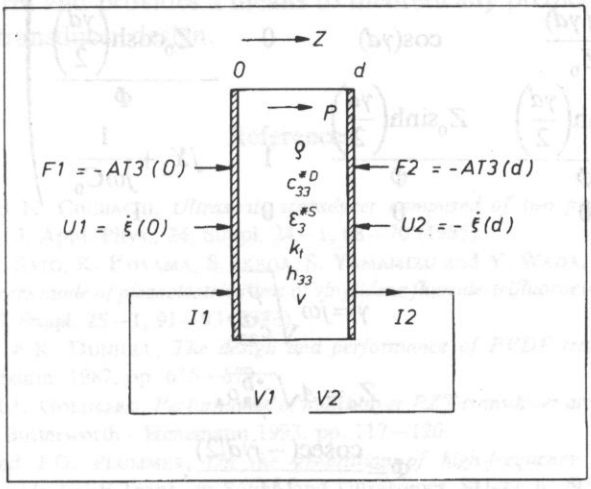

Fig. A.1. Configuration of a thickness mode free resonator. A: area of the piezoelectric material; D: thickness of the piezoelectric resonator; F_1, F_2 — forces acting on the piezoelectric material at $z=0$ and $z=d$, respectively; U_1, U_2: velocities of a particle at $z=0$ and $z=d$, respectively; I_1, I_2: currents due to electric potential difference on the piezoelectric material; k_t: electromechanical coupling factor for thickness mode resonator; v: velocity of the wave propagating in the piezoelectric material.

Fig. A.1 summarizes all forces, displacements, voltages and currents related to a basic thickness mode free resonator.

Using Eq. (A.3) and assuming a harmonic vibration, the amplitude ξ of a particle at z can be expressed as [16]:

$$\xi(z)=\frac{1}{j\omega}\,\frac{U_1\sinh[\gamma(d-z)]-U_2\sinh(\gamma z)}{\sinh(\gamma d)}, \tag{A.6}$$

where U_1 and U_2 are the velocities of the particles at $z=0$ and $z=d$, respectively.

By substituting Eq. (A.6) into Eqs. (A.1) and (A.2) and using the relationships:

$$F_1=-AT_3(0), \tag{A.7}$$

$$F_2=-AT_3(d), \tag{A.8}$$

$$V_1 - V_2 = \int_0^d E_3 dz, \tag{A.9}$$

$$I_1 = I_2. \tag{A.10}$$

the following matrix is obtained:

$$\begin{pmatrix} F_1 \\ U_1 \\ V_1 \\ I_1 \end{pmatrix} = \begin{pmatrix} \cos(\gamma d) & Z_0 \sin(\gamma d) & 0 & -\dfrac{Z_0 \sinh\left(\dfrac{\gamma d}{2}\right)}{\Phi} \\ \dfrac{\sin(\gamma d)}{Z_0} & \cos(\gamma d) & 0 & -\dfrac{Z_0 \cosh\left(\dfrac{\gamma d}{2}\right)}{\Phi} \\ \dfrac{Z_0 \cosh\left(\dfrac{\gamma d}{2}\right)}{\Phi} & \dfrac{Z_0 \sinh\left(\dfrac{\gamma d}{2}\right)}{\Phi} & 1 & jX_1 + \dfrac{1}{j\omega C_0} \\ 0 & 0 & 0 & 1 \end{pmatrix} \begin{pmatrix} F_2 \\ -U_2 \\ V_2 \\ I_2 \end{pmatrix} \tag{A.11}$$

where

$$\gamma = j\omega \sqrt{\frac{\rho}{c_{33}^{*D}}}, \tag{A.12}$$

$$Z_0 = A\sqrt{c_{33}^{*D}\rho}, \tag{A.13}$$

$$\Phi = \frac{\operatorname{cosec}(-j\gamma d/2)}{2M}, \tag{A.14}$$

$$X_1 = Z_0 M^2 \sin(-j\gamma d), \tag{A.15}$$

$$M = \frac{h_{33}}{\omega Z_0}, \tag{A.16}$$

$$C_0 = \frac{A\varepsilon_3^{*T}}{d}. \tag{A.17}$$

Since

$$v = \sqrt{\frac{c_{33}^D}{\rho}}. \tag{A.18}$$

and

$$h_{33}^2 = \frac{k_t^2 c_{33}^D}{\varepsilon_3^S} \text{ [16]}, \tag{A.19}$$

Φ and X_1 can be expressed as:

$$\Phi = \mathrm{j}\,\frac{\omega \mathrm{A}}{2k_t}\sqrt{\rho\varepsilon_3^S(1+j\varphi)}\,\frac{1}{\sinh\left(\dfrac{\gamma d}{2}\right)}, \tag{A.20}$$

$$jX_1 = \frac{k_t^2 v}{\varepsilon_3^S \omega^2 A \sqrt{1+j\varphi}} \sin(\gamma d). \tag{A.21}$$

It should be noted that the matrix of (A.11) can be used to describe layers with both forward and reverse polarization directions as well as piezoelectrically inactive layers by ascribing k_t a positive, negative or zero value, respectively.

Using the electromechanical analogies detailed in [20], it was verified that the matrix given in (A.11) is fully equivalent to the KRIMHOLTZ, LEEDOM and MATTHAEI model [13].

In summary, the matrix expression for a thickness mode free resonator was derived. This expression allows the multiple piezoelectric layers to be described in a mathematical form and provides a means to theoretically predict the performance of the multilayer transducer design.

References

[1] S. YAMAMIZU and N. CHUBACHI, *Ultrasonic transducer composed of two piezoelectric layers with variable weighting*, J. Appl. Phys., **24**, Suppl. 24–1, 68–70 (1985).

[2] K. SAKAGUCHI, T. SATO, K. KOYAMA, S. IKEDA, S. YAMAMIZU and Y. WADA, *Wide-band multilayer ultrasonic transducers made of piezoelectric films of vinylidene fluoride-trifluoroethylene copolymer*, Jap. J. Appl. Phys., **25, Suppl. 25–1**, 91–93 (1986).

[3] M.R. SMITH and A.K. DUNHILL, *The design and performance of PVDF transducers*, Proc. IEEE Ultrasonic Symposium, 1987, pp. 675–679.

[4] S.W. SMITH and R.L. GOLDBERG, *Performance of multi-layer PZT transducer arrays*, proc. Ultrasonics International 93, Butterworth–Henemann 1993, pp. 117–120.

[5] R.G. SWARTZ and J.D. PLUMMER, *On the generation of high-frequency acoustic energy with polyvinylidene fluoride*, IEEE Trans. on Sonics and Ultrasonics, **SU-27**, 6, 295–303 (1980).

[6] L. CHOFFLET and M. FINK, *A multi-piezoelectric structure: The stacked transducer*, Proc. IEEE Ultrasonics Symposium 1991, pp. 611–614.

[7] J.A. HOSSACK and B.A. AULD, *Improving the characteristics of a transducer using multiple piezoelectric layers*, IEEE Trans. UFFC, **40**, 2, 131–139 (1993).

[8] R.H. BARKER, *Group synchronizing of binary digital systems*, in: Communication theory [Ed.] W. Jackson, Butterworth, London 1953, pp. 273–287.

[9] K.M. SUNG, *Piezoelectric multilayer transducers for ultrasonic pulse compression*, Ultrasonics, **22**, 61–68 (1984).

[10] M. PLATTE, *Barker-codierte Mehrschichtwandler aus Polyvinylidenfluorid fur den Impuls-Echo-Betrieb mit Ultraschall*, Acustica, **56**, 29–33 (1984).

[11] M. PLATTE, *PVDF ultrasonic transducers*, Ferroelectrics, 75, 327–337 (1987).

[12] W.P. MASON, *Electromechanical transducers and wave filters*, D. Van Nostrand Company, Inc. 2nd Ed. 1948.

[13] R. KRIMHOLTZ, D.A. LEEDOM and G.L. MATTHAEI, *New equivalent circuits for elementary piezoelectric transducers*, Electronics Letters, **6**, 13, 398–399 (1970).

[14] E.K. SITTIG, *Transmission parameters of thickness-driven piezoelectric transducers arranged in multilayer configurations*, IEEE Trans. Sonics and Ultrasonics, **SU-14**, 4, 167–174, (1967).

[15] E. AKCAKAYA, E.L. ADLER and G.W. FARNELL, *Apodization of multilayer bulk-wave transducers*, IEEE Trans. UFFC, **36**, 6, 628–637 (1989).

[16] H. OHIGASHI, *The applications of ferroelectric polymers*, [Eds.] T.T. Wang, J.M. Herbert and A.M. Glass, The Blackie Group Publishers/Chapman and Hill, New York 1988, pp. 236–249.

[17] G.S. De Silets, J.D. Fraser and G.S. Kino, *The design of efficient broad-band piezoelectric transducers*, IEEE Trans. on Sonics and Ultrasonics, **SU-25**, 3, 115–125 (1978).

[18] P.A. Lewin, Q. Zhang and P.E. Bloomfield, *Enhanced bandwidth ultrasound transducers with multiple piezoelectric polymer layers*, in: New developments in ultrasonic transducers and transducer systems, Proc. SPIE 1733, SPIE Washington, USA, 1992, pp. 297–306.

[19] P.A. Lewin, *Miniature piezoelectric polymer ultrasonic hydrophone probes*, Ultrasonics, **19**, 213–216 (1981).

[20] T.F. Hueter and R.H. Bolt, Sonics, Chapt. 4, John Wiley and Sons, 1955.

ARCHIVES OF ACOUSTICS
20, 1, 91–94 (1995)

BRIEF NOTE

AN APPROXIMATION TO SURFACE ADMITTANCE OF Y-ROTATED LANGASITE

E. DANICKI

Institute of Fundamental Technological Research
Polish Academy of Sciences
(00-049 Warszawa, Świętokrzyska 21)

New piezoelectric crystal, langasite, is expected to find many applications in piezoelectronics. An approximation to its electro-mechanical surface property is given that allows to analyze B-G waves in the crystal and corresponding SAW devices.

New piezoelectric crystal possessing interesting both optical and piezoelectric properties has been grown recently [1]. It is langasite, a trigonal crystal of 32 symmetry class (like quartz), which chemical formula is $La_3Ga_5SiO_{14}$. It is expected to have temperature compensated cuts, like quartz, what is important for applications in piezoelectric devices, resonators and some surface acoustic (SAW) filters. The langasite is much stronger piezoelectric and this will allow many new applications of such filters [2].

A number of SAW devices has been proposed exploiting Bleustein-Gulayev (BG) wave in Y-rotated quartz, which is the wave propagating on the crystal surface tangential to the crystallographic X axis, which axis is transversal to the wave propagation direction (the wave does not depend on X). Similar waves exist in langasite, and due to stronger piezoelectric effect, they can be even more interesting for applications.

In this paper we present certain useful characterization of electro-mechanical surface properties of Y-rotated langasite. This is a functional approximation to the surface Green's function in spectral domain, valid in certain small but important domain of spectral variable. Y-rotated crystal halfspace of langasite is considered, and all electro-mechanical quantities observed on its surface $y=0$ are involved in the approximated relationship, similar to that presented for quarts in [3]. Following [2, 4], the material constants of langasite important for our purposes are: mass density $\rho = 5.751$ [10^3 kg/m^3], e_{11}, e_{14} equal — .45 and .077 [C/m^2], c_{14}, c_{44}, c_{66} equal 14.7, 53.4, 42.35 [10^9 N/m^2], and ε_1, ε_3 equal 19 and 49.2, correspondingly:

These quantities are:

- electric potential φ,
- particle displacement (X-component) $u_3 = u$,
- surface traction (T_4 in matrix notation) $T_{23} = t$,

all on the surface of the substrate stretching out for $x_2 = y > 0$, and expressed in coordinate system which axes $x_1 = x$ and $x_3 = X$ (crystallographic axis) lay on the substrate surface. In what follows, we consider these quantites as harmonic functions of lime (t) and space (at $y = 0$)

$$\exp(j\omega t - jrx)$$

where ω, r are angular frequency (given) and wave-number (a spectral variable), correspondingly. For convenience, the notations of complex amplitudes of the above enlisted quantities are applied the same.

On the reasons presented in [3], we postulate following approximated functional relationship involving the above quantities, dependent on spectral variable r,

$$\begin{aligned} \varphi &= \frac{1}{\varepsilon_0 \varepsilon_e \sqrt{r^2}} \frac{\sqrt{r^2 - k_s^2} - \alpha\sqrt{r^2}}{\sqrt{r^2 - k_s^2} - \beta\sqrt{r^2}} D + \frac{1}{\sqrt{r^2}} \frac{a\sqrt{r^2 - k_s^2} - b\sqrt{r^2}}{\sqrt{r^2 - k_s^2} - \beta\sqrt{r^2}} T, \\ u &= \frac{1}{\sqrt{r^2}} \frac{a^*\sqrt{r^2 - k_s^2} - b^*\sqrt{r^2}}{\sqrt{r^2 - k_s^2} - \beta\sqrt{r^2}} D + \frac{1}{\sqrt{r^2}} \frac{c\sqrt{r^2 - k_s^2} - \gamma\sqrt{r^2}}{\sqrt{r^2 - k_s^2} - \beta\sqrt{r^2}} T, \end{aligned} \tag{1}$$

which can also be rewritten in form

$$\begin{aligned} D &= \varepsilon_0 \varepsilon_e \sqrt{r^2} \frac{\sqrt{r^2 - k_s^2} - \beta\sqrt{r^2}}{\sqrt{r^2 - k_s^2} - \alpha\sqrt{r^2}} \varphi - e_0 e_e \frac{a\sqrt{r^2 - k_s^2} - b\sqrt{r^2}}{\sqrt{r^2 - \alpha\sqrt{r^2}}} T, \\ u &= \varepsilon_0 \varepsilon_e \frac{a^*\sqrt{r^2 - k_s^2} - b^*\sqrt{r^2}}{\sqrt{r^2 - k_s^2} - \alpha\sqrt{r^2}} \varphi - \frac{1}{\sqrt{r^2}} \frac{d\sqrt{r^2 - k_s^2} - \eta\sqrt{r^2}}{\sqrt{r^2 - k_s^2} - \alpha\sqrt{r^2}} T, \end{aligned} \tag{2}$$

which both approximations are assumed valid for $r \approx k_s$, where k_s is the cut-off wave-number of bulk transversal wave (for considered rotated halfspace), $\sqrt{\cdot}$ is chosen positive if real-valued, or negative if imaginary-valued.

In the above approximation, ε_e, α, β, γ, η, c, d are real-valued parameter, and a, b — complex parameters which should be replaced by their complex-conjugated values if r is negative. All the approximation parameters, and cut-off wave-number k_s can be evaluated with help of the method presented in [3] (note however the difference in relationships presented in this paper, there is D_2 involved instead of $\Delta D_\perp$ in [3], this is applied for convenience of analysis of interfacial waves [5]. They are presented in Fig. 1 as a function of rotation angle θ (if $\theta = 0$ then $x = Y$ and $y = Z$, and if $\theta = 90°$ then $x = Z$ and $y = -Y$), while in Fig. 2 we present corresponding parameters for Y-rotated quartz, for comparison.

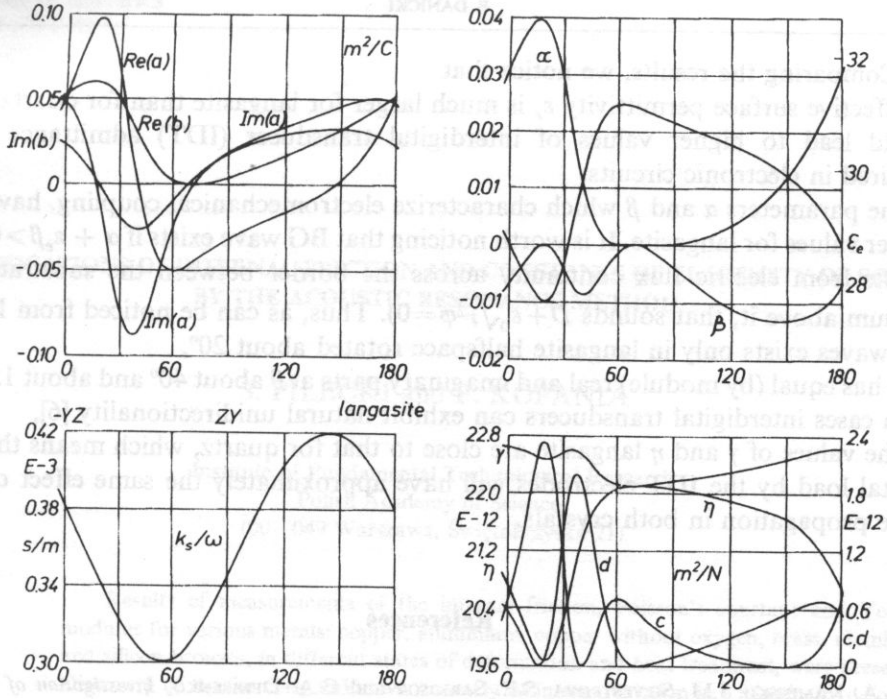

Fig. 1 Dependence of the approximation parameters for langasite on rotation angle θ.

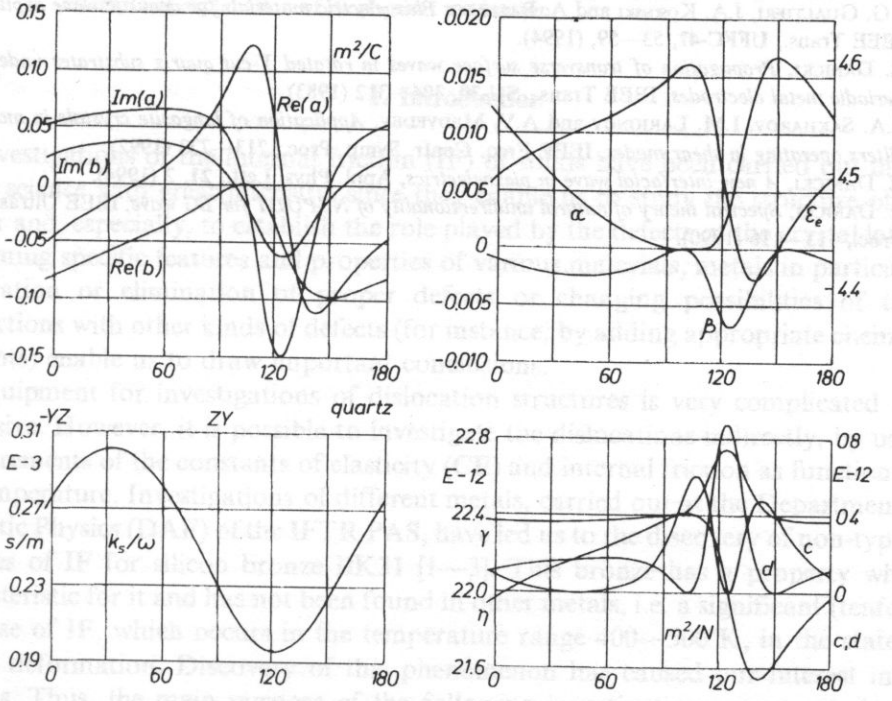

Fig. 2 Approximation parameters for *Y*-rotated quartz.

Comparing the results, we notice that

- effective surface permittivity ε_e is much larger for langasite than for quartz. This would lead to higher values of interdigital transducer (IDT) admittance often required in electronic circuits,
- the parameters α and β which characterize electromechanical coupling, have also higher values for langasite. It is worth noticing that BG wave exists if $\alpha + \varepsilon_e\beta > 0$ (this results from electric flux continuity across the border between the substrate and vacuum above it, that sounds $D + \varepsilon_0\sqrt{r^2\varphi} = 0$). Thus, as can be noticed from Fig. 1, BG waves exists only in langasite halfspace rotated about 20°,
- b has equal (by module) real and imaginary parts at θ about 40° and about 150°, in both cases interdigital transducers can exhibit natural unidirectionality [6],
- the values of γ and η langasite are close to that for quartz, which means that the crystal load by the IDT electrodes will have approximately the same effect on BG wave propagation in both crystals.

References

[1] A.A. KAMINSKII, I.M. SILVESTROVA, S.E. SARKISOV and G.A. DENISENKO, *Investigation of trigonal* La_{1-x} Nd_x Ga_5SiO_{14} II *Spectral laser and electromechanical properties*, Physica Statue Solidi, **80**, 607-620 (1983).

[2] J.G. GUALTIERI, J.A. KOSINSKI and A. BALLATO, *Piezoelectric materials for acoustic wave applications*, IEEE Trans., **UFFC-41**, 53—59, (1994).

[3] E. DANICKI, *Propagation of transverse surface waves in rotated Y-cut quartz substrates under heavy periodic metal electrodes*, IEEE Trans., **SU-30**, 304—312 (1983).

[4] S.A. SAKHAROV, I.M. LARIONOV and A.V. MEDVEDEV, *Application of langasite crystals in monolithic filters operating in shear modes*, IEEE Freq. Contr. Symp. Proc., 713—723 (1992).

[5] E. DANICKI, *A new interfacial wave in piezoelectrics*, Appl. Phys. Lett., **21**, 2 (1994).

[6] E. DANICKI, *Spectral theory of natural unidirectionality of NSPUDT for BG wave*, IEEE Ultras. Symp. Proc., 113—116 (1990).

ARCHIVES OF ACOUSTICS
20, 1, 95–110 (1995)

INVESTIGATIONS OF INTERNAL FRICTION AND CONSTANTS OF ELASTICITY OF SOLIDS BY THE ACOUSTIC RESONANCE METHOD

S. PILECKI and P. KOPANIA

Institute of Fundamental Technological Research
Polish Academy of Sciences
(00—049 Warszawa, Świętokrzyska 21)

Results of measurements of the internal friction, Poisson's constant and Young's modulus for various metals: copper, aluminium, copper without oxygen, brass, aluminium and silicon bronzes, in different states of deformation and heat treatment, were presented. Discovery of the formerly unknown anomaly of internal friction in a plastically deformed silicon bronze BK31, occurring in the temperature range 400—500 K, was discussed. A number of effects that accompany this phenomenon were described, together with attempts of explanation of its physical mechanism.

1. Introduction

Investigations of the internal friction (IF) of solids have been carried out in the world science with great intensity, since they enable us to study the structure of the matter and, especially, to establish the role played by the defects of the crystal lattice in forming specific features and properties of various materials, metals in particular. Generation or elimination of proper defects or changing possibilities of their interactions with other kinds of defects (for instance, by adding appropriate chemical elements) enable us to draw important conclusions.

Equipment for investigations of dislocation structures is very complicated and expensive. However, it is possible to investigate the dislocations indirectly, by using measurements of the constants of elasticity (CE) and internal friction as functions of the temperature. Investigations of different metals, carried out at the Department of Acoustic Physics (DAF) of the IFTR PAS, have led us to the discovery of non-typical changes of IF for silicon bronze BK31 [1—3]. This bronze has a property which characteristic for it and has not been found in other metals, i.e. a significant (tenfold) decrease of IF, which occurs in the temperature range 400—500 K, in the state of plastic deformation. Discovery of this phenomenon has caused our interest in its reasons. Thus, the main purpose of the following investigations was to study the mechanisms causing this phenomenon. The way leading to that consists in geting

information on the submicroscopic processes that occur in BK31 bronze and cause the mentioned macroscopic effects connected with IF under the specified conditions. This phenomenon was not known in the world science before, and was discovered by us and announced at two international conferences [2, 4]. At the DAF, the investigations were carried out by applying the resonance elastometer, i.e. the apparatus for measurements of IF by means of the acoustic resonance method [6, 7]. Other investigations performed by means of a torsional pendulum and a quartz resonance oscillator were made in cooperation with Gdańsk University of Technology and Physical-Technological Institute in St. Petersburg, respectively.

2. Conditions of investigations and results

Generally, the phenomenon of friction and the energy dissipation connected with it can be external, for instance friction of surfaces sliding in contact with one another, or internal, for instance, displacements of atoms pressed against each other, motion of dislocations, interactions of magnetic and electric fields in ferromagnetic and dielectric materials.

Changes of IF are most frequently recorded as functions of different parameters, such as the amplitude of deformations of a sample, the frequency of deformation and the temperature of a sample. Their analysis can give a lot of information on the internal processes induced by mobility of defects of the crystal lattice and their different transformations.

Changes of the modulus of elasticity E and Poisson's constant ν are usually measured together with measurements of IF as functions of the same variables. In general, important changes or anomalies do not occur during measurements of these parameters; namely, when temperature increases, Poisson's constant ν also increases monotonically and Young's modulus E decreases. The changes of IF cause the deflection of the curve $E(T)$. This deflection is easy to notice due to the measurements made by means of a torsional pendulum, and slightly less visible when the resonance elastometer is applied.

2.1. The dependence of IF *on the amplitude of deformation*

The measurements of IF can be done in a wide range of amplitudes of deformation. The applicable amplitudes depend on the frequency and the method used in measurements.

In the case of high frequencies, $10^5 - 10^{10}$Hz, the measurements of IF can be done in the range of the amplitudes of relative deformation of about $10^{-9} - 10^{-8}$, which are too small to cause a permanent deformation of the crystal structure. The frequencies $10^{-2} - 10^4$ Hz and the amplitude $10^{-3} - 10^{-2}$ that can distrub the physical cohesion of the crystals are the second extreme case. In measurements of IF by the torsional pendulum and resonance elastometer, the amplitude of relative deformation is within the ranges $10^{-6} - 10^{-3}$ and $10^{-9} - 10^{-8}$, respectively.

In the first approximation one can notice that, in the range of low deformations, the value of IF is independent of the amplitude. On the other hand, for higher deformation, this value increases when the amplitude increases (Fig. 1) [16]. This fact indicates the existence of two different mechanisms of energy dissipation that occur in the ranges of the relatively low and high amplitudes. The limit between these ranges corresponds to the points of inflexion of the curves presented in Fig. 1. The value of the amplitude that starts the mechanism of the internal friction dependent on the amplitude is different for various materials and, for the same material, depends on the temperature and frequency. This fact can be explained when the influence of temperature and frequency on the mobility of lattice defects is considered.

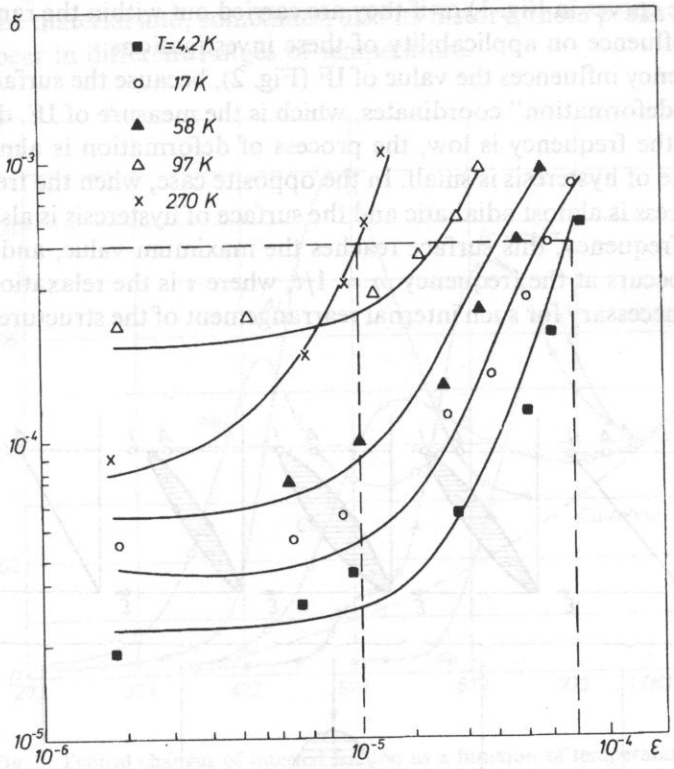

Fig. 1. Dependence of internal friction on the amplitude.

Generally, the total value of IF, Q^{-1}, consists of two parts,

$$Q^{-1} = Q_0^{-1} + Q_z^{-1}, \tag{2.1}$$

where $Q^{-1} = Q_0^{-1}$ is the component independent of the amplitude and occurs at lower amplitudes up to the point of inflexion, Q_z^{-1} is the component for higher amplitudes and depends on the amplitude.

2.2. *The dependence of* IF *on the frequency*

By applying different measurement methods, it is possible to investigate IF in the very range of frequencies — from 10^{-4}... 10^{-3} Hz to 10^{11}... 10^{12} Hz. Investigation made by means of the torsion pendulum and the resonance elastometer can be done in the ranges 10^{-2}... 10^{2} Hz and 5.10^{3}... 3.10^{4} Hz, respectively.

The known results of investigations of the IF dependence on the frequency are inconsistent with each other, not only in the case of different materials, but even for the same material.

The fact, whether the investigations are made at a sufficiently low amplitude of deformation, for which $Q^{-1} = Q_0^{-1}$ is still independent of the amplitude (the horizontal sections of the curves in Fig. 1) or if they are carried out within the range of high Q_z^{-1}, has a great influence on applicability of these investigations.

The frequency influences the value of IF (Fig. 2), because the surface of hysteresis in the „stress-deformation" coordinates, which is the measure of IF, depends on this frequency. If the frequency is low, the process of deformation is almost isothermal and the surface of hysteresis is small. In the opposite case, when the frequency is very high, this process is almost adiabatic and the surface of hysteresis is also small. At the intermediate frequency, this surface reaches the maximum value, and then IF is the largest. This occurs at the frequency $\omega = 1/\tau$, where τ is the relaxation time, i.e. the time which is necessary for such internal rearrangement of the structure of a body that

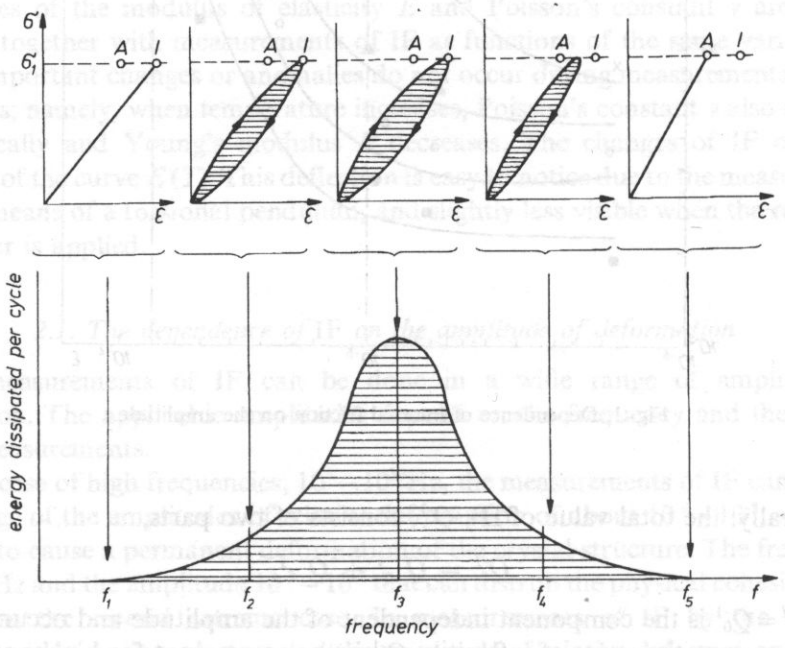

Fig. 2. Dependence of internal friction on the frequency [9].

the deformation of this body changes by $1/e$ of its initial values, where e is the base of natural logarithms.

2.3. The dependence of IF on the temperature

The investigations of most of the materials indicate that, in the range of temperature from 4 K to 0.5—0.6 T_t, where T_t is the melting temperature, the value of Q^{-1} (T) increases monotonically almost lineary when T increases, whereas, at higher temperature, the increase of Q^{-1} (T) is more rapid-exponential (Fig. 3). In many cases, despite this kind of changes, the peaks appear on the curves of Q^{-1} (T), which are caused by the specific influence of different kinds of the crystal lattice defects. According to the material and, sometimes, also its history, these peaks have different height and appear in different ranges of temperature.

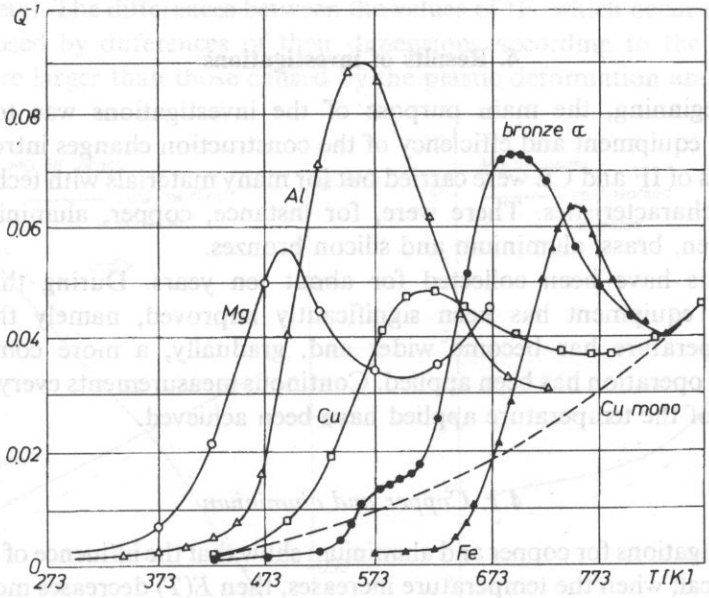

Fig. 3. Typical changes of internal friction as a function of temperature.

3. The samples and procedure of measurements

In the measurements made at the DAP by means of the resonance elastometer, the samples in the form of disks with diameter 30 mm and thickness 1 – 3 mm were used. They were supported at three points placed symmetrically with respect to the center, and in line with the nodes of bending vibrations for two different modes. The electronic setup excited the sample to oscillations in the first or second modes with

two different resonance frequencies, which depend on the temperature. Knowing the values of these frequencies, the dimensions of the sample and the density of the material, the CE have been calculated. The IF has been determined by the measurements of the amplitude of vanishing free oscillations of the sample excited to the resonance vibrations [6, 7].

To achieve a low temperature, the measurement cell together with the sample were submerged in a liquid nitrogen and this caused cooling of the sample to about -160° (about 110 K) after a few hours. Total or partial emerging of the cell from the liquid nitrogen made the temperature increase faster or slower. The electric heater was used to achieve higher temperature. The rate of the temperature increase was regulated by changing the power of the heater. Construction of the experimental equipment and/or the elastic properties of the tested materials limit the maximal applied temperature.

The operating principle of the torsion pendulum has been described, for instance, in [15].

4. Results of investigations

In the beginning, the main purpose of the investigations was to verify the measurement equipment and efficiency of the construction changes introduced. The measurements of IF and CE were carried out for many materials with technical purity and known characteristics. There were, for instance, copper, aluminium, copper without oxygen, brass, aluminium and silicon bronzes.

The results have been collected for about ten years. During that time the measurement equipment has been significantly improved, namely the range of possible temperature has become wider and, gradually, a more complete automatization of operation has been applied. Continous measurements every 1 deg in the whole range of the temperature applied have been achieved.

4.1. Copper and aluminium

The investigations for copper and aluminium show that the influence of temperature on CE is typical; when the temperature increases, then $E(T)$ decreases monotonically and $v(T)$ increases. The changes of $Q^{-1}(T)$ are similar to those presented in Fig. 3, which is a typical diagram of the monotonic increase of IF as a function of temperature.

4.2. Copper without oxygen of the MOB type

Besides the general testing properties of copper without oxygen, the special purpose of our measurements is to verify whether, after application of high hydrostatic pressures, the changes in the elastic properties of metal occur, like after the mechanical plastic deformation. CE was measured in the range of temperature 20 ... 230°C, with the step of 10 deg. IF was investigated for the temperature 30, 100, 170 and 230°C.

Results of these measurements show that the influence of hydrostatic pressure is completely similar to that of the mechanical deformation, despite the fact that the shape of the samples was practically unchanged when pressures of 300, 450 and 600 MPa were used. This result is rather unexpected, since it should not occur theoretically.

4.3. Brass MO58

Brass MO58 was investigated at the temperature from about 110 to 800 K, after a single plastic deformation (near 9%) and annealing. Typical functions $Q^{-1}(T)$, $E(T)$ and $\nu(T)$ have been found; when the temperature increases, the values of $E(T)$ and $\nu(T)$ change almost linearly, and $Q^{-1}(T)$ increases — slowly in the beginning Fig. 4, and faster above the temperature 420 K, like in Fig. 3. The value of IF, in the whole range of temperature, does not differ significantly for the plastically deformed and annealed metal. The differences between the values of IF, which occur in the samples and are caused by differences of their dimensions according to the technological tolerance, are larger than those caused by the plastic deformation and annealing.

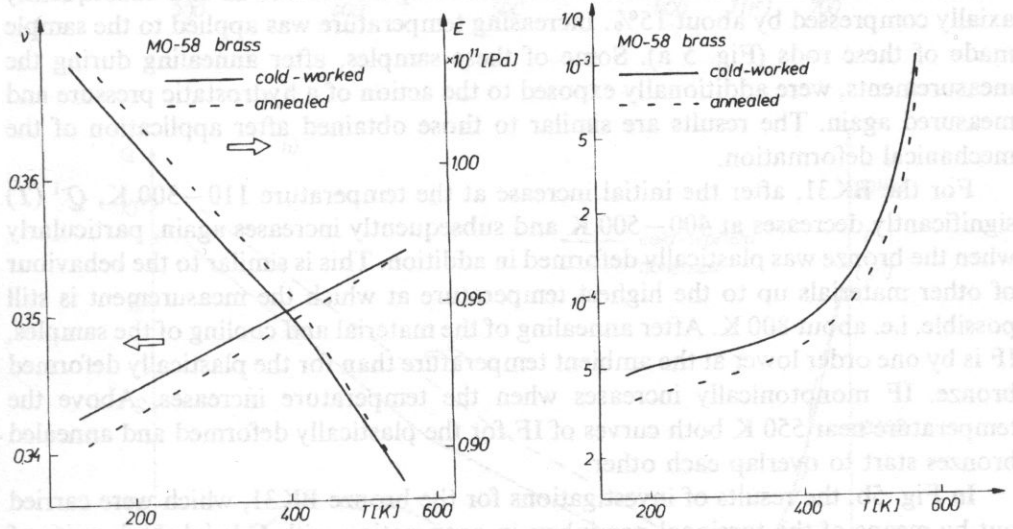

Fig. 4. Constants of elasticity and internal friction for brass as a function of the temperature.

4.4. Aluminium bronze BA1044

The samples of aluminium bronze, which were out from a raw rod, were heated during the measurements to the temperature at which IF could be measured. Monotonic increase of $Q^{-1}(T)$ and typical changes of CE were obtained.

Similarity of the changes of Q^{-1} (T) is very important in the case of materials described since, on this basis, a different behavior of Q^{-1} (T) for the silicon bronze becomes very significant.

4.5. Silicon bronze BK31

The investigations made at the DAP of IFTR have led us to the discovery of non-typical changes of Q^{-1} (T) for silicon bronze BK31 [1–3]. For this bronze, a significant about tenfold decrease of IF occurs in the plastically deformed state at the temperature from 400 to 500 K (Fig. 5a). Consequently, this bronze has been tested under various conditions and by means of other methods. Previous investigations were done in the whole range of temperature, i.e. from about 110 to 800 K. Later, this range was limited to the temperature above 300 K, since the anomalies of the properties occur at the temperature in the range 400–500 K.

Four types of rods made of bronze BK31 were used to cut out the samples. First rod was simply a raw material from metallurgical works, the second and third ones were, in addition, axially compressed by about 4.5% and 15%, respectively. The fourth one was annealed for one hour at the temperature 780 K and subsequently axially compressed by about 15%. Increasing temperature was applied to the sample made of these rods (Fig. 5 a). Some of these samples, after annealing during the measurements, were additionally exposed to the action of a hydrostatic pressure and measured again. The results are similar to those obtained after application of the mechanical deformation.

For the BK31, after the initial increase at the temperature 110–300 K, Q^{-1} (T) significantly decreases at 400–500 K and subsequently increases again, particularly when the bronze was plastically deformed in addition. This is similar to the behaviour of other materials up to the highest temperature at which the measurement is still possible, i.e. about 800 K. After annealing of the material and cooling of the samples, IF is by one order lower at the ambient temperature than for the plastically deformed bronze. IF monotonically increases when the temperature increases. Above the temperature near 550 K both curves of IF for the plastically deformed and annealed bronzes start to overlap each other.

In Fig. 5b, the results of investigations for the bronze BK31, which were carried out by means of the torsional pendulum in cooperation with Gdańsk University of Technology, are shown. A complete compliance of results follows from the comparison of Figs. 5a and 5b.

5. The most important results for the silicon bronze

Trying to explain the abnormal changes of IF for the silicon bronze, the investigations of metallographic specimens was made before and after annealing. They indicate that the grains of the metal become smaller during annealing. To check whether this fact of reduction of the grain dimensions is the reason of the anomaly of

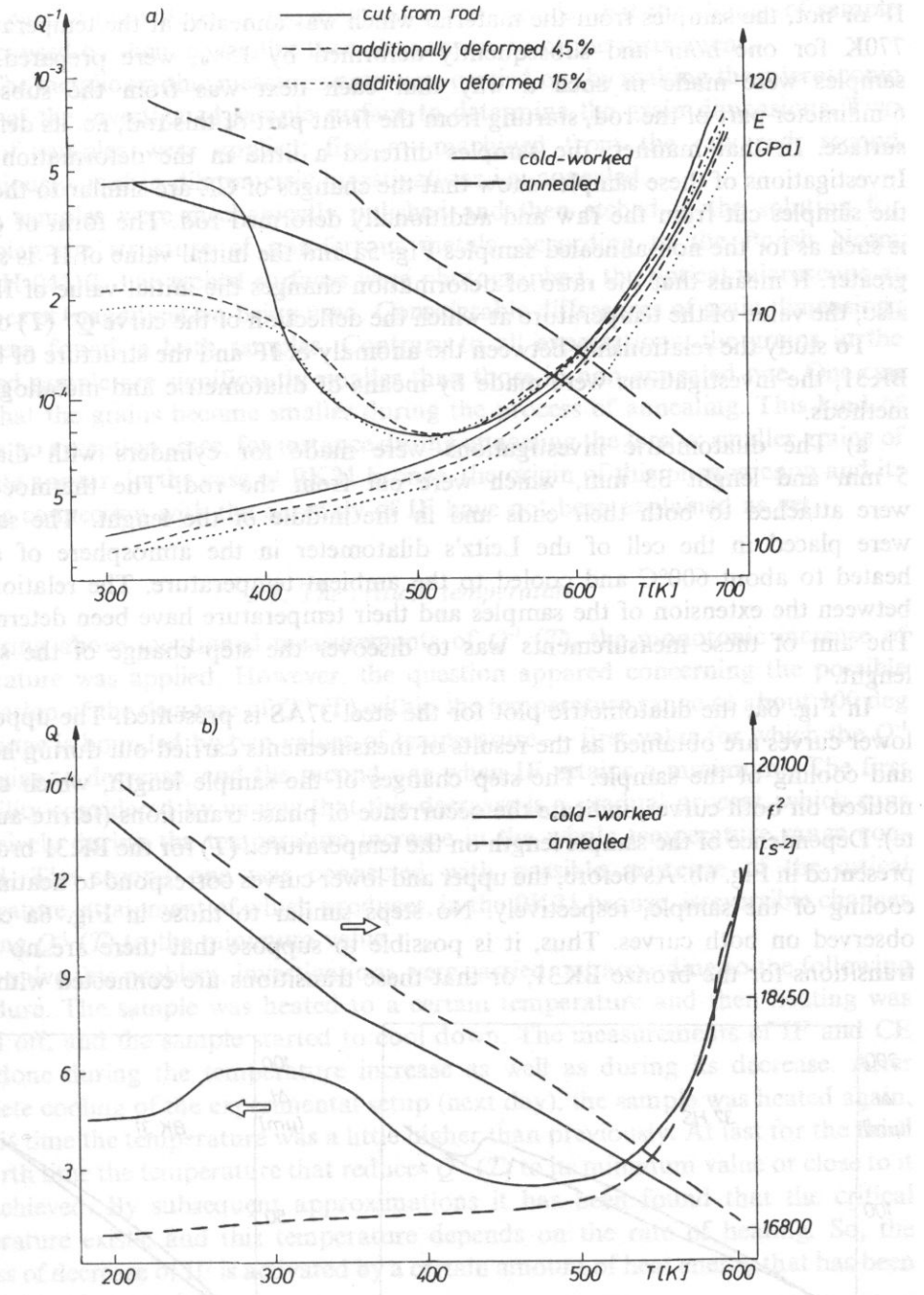

Fig. 5. Internal friction and Young's modulus of the plastically deformed and annealed bronze BK31 measured by means of: a) — resonance elastometer, b) — torsional pendulum.

IF or not, the samples from the material which was annealed at the temperature of 770K for one hour and subsequently deformed by 15%, were prepared. Four samples were made in such a way that each next was from the subsequent 6-milimeter part of the rod, starting from the front part of this rod, i.e. its deformed surface. In that manner, the samples differed a little in the deformation ratio. Investigations of these samples show that the changes of CE are similar to those for the samples cut from the raw and additionally deformed rod. The form of $Q^{-1}(T)$ is such as for the non-annealed samples Fig. 5a and the initial value of IF is slightly greater. It means that the ratio of deformation changes the initial value of IF and, also, the value of the temperature at which the deflection of the curve $Q^{-1}(T)$ occurs.

To study the relationship between the anomaly of IF and the structure of bronze BK31, the investigations were made by means of dilatometric and metallographic methods.

a) The dilatometric investigations were made for cylinders with diameter 5 mm and lenght 33 mm, which were cut from the rod. The thermocouples were attached to both their ends and in the middle of the lenght. The samples were placed in the cell of the Leitz's dilatometer in the atmosphere of argon, heated to about 600°C and cooled to the ambient temperature. The relationships between the extension of the samples and their temperature have been determined. The aim of these measurements was to discover the step change of the sample lenght.

In Fig. 6a, the dilatometric plot for the steel 37AS is presented. The upper and lower curves are obtained as the results of measurements carried out during heating and cooling of the sample. The step changes of the sample length, which can be noticed on both curves, indicate the occurrence of phase transitions (ferrite-austenite). Dependence of the sample length on the temperature $l(T)$ for the BK31 bronze is presented in Fig. 6b. As before, the upper and lower curves correspond to heating and cooling of the sample, respectively. No steps similar to those in Fig. 6a can be observed on both curves. Thus, it is possible to suppose that there are no phase transitions for the bronze BK31, or that these transitions are connected with such

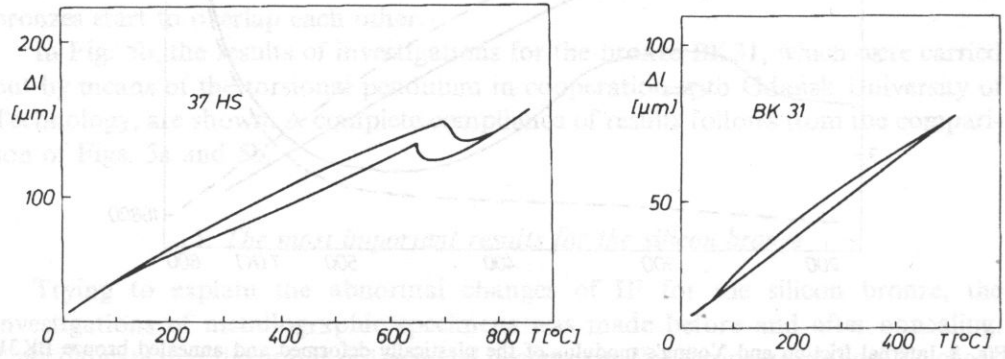

Fig. 6. Dependence of the extension on the temperature for: a) — steel 37HS. b) — bronze BK31.

a small part of the volume of the material of the sample, that the change of sample length caused by them is smaller than the sensitivity of the instrument.

b) The metallographic measurements were carried out by making the microscopic photos of the investigated sample surface to determine the grain dimensions. Two kinds of samples were applied; first — machined from the raw rod, second — previously used in dilatometric investigations i.e. annealed.

The samples were mechanically polished and then etched in the solution for developing the structure of non-ferrous metals, according to the Polish Norm PN-75/H-04512. The etched surfaces were photographed, the optical microscope at 500 times of magnification being used. Considerable differences of grain dimensions have been found in both samples. Contrary to all expectations, the grains in the annealed sample are significantly smaller than those in non-annealed one. One can think that the grains become smaller during the process of annealing. This kind of effect is no exception since, for instance during annaeling the ferrite; smaller grains of austenite appear. In the case of BK31 bronze, the origin of this phenomenon and its possible connection with the anomaly of IF have not been explained as yet.

5.1. The critical temperature

During above mentioned measurements of Q^{-1} (T), the monotonic increase of temperature was applied. However, the question appared concerning the possible explanation of the decrease of Q^{-1} (T) within the temperature range of about 100 deg (this range is bounded by two values of temperature — first value for which the Q^{-1} (T) begins to decrease, and the second one when IF attains a minimum). The first possibility considered by us was that this decrease is a gradual process, which runs successively during the temperature increase in the whole temperature range considered. The second one was connected with possible existence of the crtical temperature, attainment of which produces, in the BK31 bronze, irreversible changes reducing Q^{-1} (T) to the minimum value.

To solve this problem, investigations were carried out according to the following procedure. The sample was heated to a certain temperature and then heating was turned off, and the sample started to cool down. The measurements of IF and CE were done during the temperature increase as well as during its decrease. After complete cooling of the experimental setup (next day), the sample was heated again, but this time the temperature was a little higher than previously. At last for the third or fourth time the temperature that reduces Q^{-1} (T) to its minimum value or close to it was achieved. By subsequent approximations it has been found that the critical temperature exists, and this temperature depends on the rate of heating. So, the process of decrease of IF is activated by a certain amount of heat energy that has been supplied to the sample.

Since IF is connected with the mobility of the lattice defects, dislocations in particular, the comparative measurements of the usual samples and the ones additionally irradiated by the gamma rays dose of 40Mrad were carried out. This

kind of irradiation increases the concentration of point defects, which can additionally attract the dislocations and, consequently, decrease their mobility [10, 11, 12]. After this irradiation, the depth of the decrease of Q^{-1} (T) remains unchanged, but the temperature connected with the beginning of this decrease is higher — about 70 deg — for the irradiated samples.

Critical temperatures for the non-irradiated BK31 bronze and the irradiated one are equal to 110°C (380 K) and 180°C (450 K), respectively — (see Fig. 7). Thus, this irradiation influences also the critical temperature.

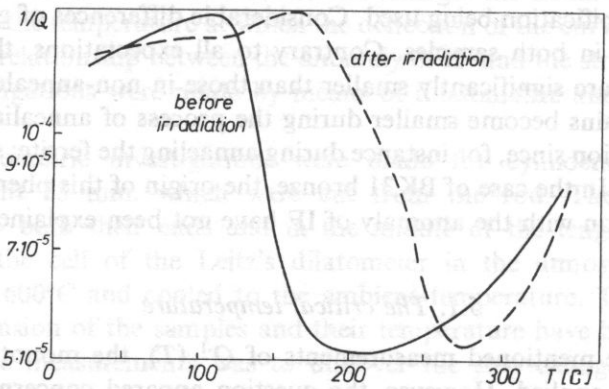

Fig. 7. Dependence of Q^{-1} (T) for irradiated and non-irradiated bronzes.

To find out how strong the connection between the anomaly of IF and the plastic deformation is, the samples with different ratios of deformation and those deformed in two steps were investigated. The first step was a plastic deformation of the raw rood in metals works, i.e. cold working. After cutting the samples off this rod and annealing them at the temperature used in the first measurement, the second step of the plastic deformation was done mechanically or by means of the hydrostatic pressure. The influence of the maximal temperature of annealing on the character of the anomaly was also examined. The samples annealed at the maximal temperature for this material, near 800 K, do not differ from those annealed at a lower temperature, even by 100 or 200 K, when the characteristics of Q^{-1} (T) for the first and second measurements are compared.

5.2. Influence of the chemical composition changes of the bronze

To investigate the importance of each component of the alloy BK31 on formation of the IF anomaly, ten laboratory-prepared alloys, with various contents of manganese and silicon, were made (Table 1). They slightly differed in compositions in comparison to the norm PN-69/H-87050, and they did not contain the additions and impurities, occuring in the raw material. The measurements of IF have not led us to the conclusion that the phenomenon of the IF decrease exists in any of these alloys in the scale comparable with BK31.

Table 1. Compositions of the laboratory-prepared alloys similar to the composition of the bronze BK31, according to the norm, [weight %].

Number of sample	Copper content [%]	Manganese content [%]	Silicon content [%]	Impurities [%]
1	95.03	1.98	2.99	—
2	95.08	1.61	2.51	—
3	96.71	1.24	2.04	—
4	97.54	0.89	1.58	—
5	98.35	0.53	1.12	—
6	96.94	1.94	1.12	—
7	96.83	1.59	1.58	—
8	96.71	1.24	2.05	—
9	96.60	0.89	2.51	—
10	96.48	0.54	2.98	—
NORM	94.0—95.3	1.0—1.5	2.7—3.5	1.0

Our analysis of the chemical composition of BK31 which was carried out with the help of the X-ray analyser, shows large differences between the reality and the norm (Table 2). Thus, the second series of the alloy, with various contents of the basic chemical elements, was prepared. This time, their compositions were based on the real one obtained from our analysis, i.e. with addition of titanium, which is not mentioned in the norm. The results of the measurements of Q^{-1} (T), obtained for these alloys confirm the existence of anomalous changes of IF, which have been observed for BK31. However, these changes are smaller, because the depth of the IF decrease for laboratory-prepared alloys is lower than for the raw material, i.e. originating from

Table 2. Compositions of the laboratory-prepared alloys similar to the real composition of the bronze BK31 [weight %]

Number of sample	Copper content [%]	Manganese content [%]	Silicon content [%]	Titanium content [%]	Impurities [%]
1	97.12	1.35	1.53	—	—
2	98.27	0.20	1.53	—	—
3	97.93	0.50	1.53	—	—
4	98.45	1.35	0.20	—	—
5	98.15	1.35	0.50	—	—
6	100.00	—	—	—	—
7	96.47	1.35	1.53	0.65	—
BK31	94.7	1.30	1.50	0.60	1.90

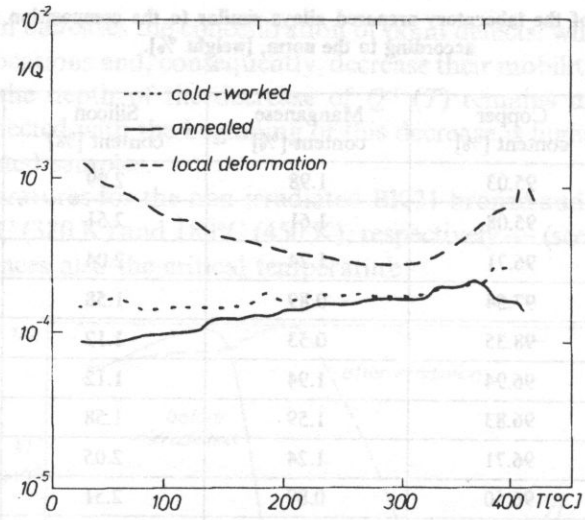

Fig. 8. Dependence of Q^{-1} (T) for the sample No. 10 from Table 1. This sample was deformed to a different extent.

metalurgical works (Fig. 8). The ratio of plastic deformation is undoubtedly higher for raw rods as a result of cold working in metal works than for the samples machined from cast billet and squeezed in the laboratory. Thus, the increase of the ratio of deformation intensifies the anomaly of Q^{-1} (T).

It is possible to assume that the interactions between the basic components of the alloy, eventually in the presence of the vacancies, are the origin of the described anomaly of IF. In the metal, the concentration of vacancies significantly increases when the deformation and temperature increase, and decreases after annealing. The various phases of such compounds as for instance Cu-Si, Cu-Ti, Mn-Ti, Mn-Si and others, can be these components. Our investigations will be continued to confirm the above suggestions.

6. Conclusions

1. The measurements of IF and CE for several metals, which were carried out at the beginning of the measurements by means of the resonance elastometer, gave us the results complying with the references. This confirm the opinion about proper functioning of the measurement equipment and reliability of the measurements made. These measurements enabled us to find the important differences in the value of IF occuring in the silicon bronze and in other materials tested.

2. There is an interesting property of the silicon bronze; the approx. tenfold decrease of IF occurs in the plastically deformed state of this bronze at the temperature in the range of 400... 500K. This phenomenon does not appear in the annealed samples; then Q^{-1} (T) increases monotonically.

3. The decrease of IF at 400... 500K should be caused by the decrease of the dislocation motion, i.e. the appearance of additional obstacles which block this motion. This fact can be connected with attraction of the dislocations by the point defects or complexes formed by the atoms of silicon, manganese and, eventually, titanium and by vacancies.

4. The obstacles of small dimensions even those which are comparable with the dimensions of a few atoms are sufficient to impede the dislocation motion. On the other hand, the possibility or direct recognition of such small obstacles is very small in the highly complicated structure as BK31, even with the help of the electron microscopy. Therefore, indirect methods, based on investigations of macroscopic properties of the material, are necessary.

5. There is a critical temperature for plastically deformed BK31, which depends on the time of annealing. When this temperature is attained the process of significant decrease of IF can not be stopped solely by the temperature decrease.

6. Comparison of the temperature characteristics of the anomaly of IF for the irradiated and non-irradiated bronzes indicates that the starting point of this anomaly is shifted by about 80 deg towards higher temperature in the case of application of the irradiation.

7. The described feature of the temperature characteristic of IF for the silicon bronze is a unique phenomenon. The reasons of this phenomenon are not known as yet. We intend to carry on further investigations to explain that phenomenon.

References

[1] S. PILECKI, R. JEMIELNIAK and J. KRÓLIKOWSKI, *Acoustic investigations of the role of dislocations in the process of metal destruction* (in Polish), Acoustics in technology and medicine, IFTR PAS, Warsaw 1985, pp. 103—110.

[2] S. PILECKI, J. KRÓLIKOWSKI and R. JEMIELNIAK, *Internal friction on silicon bronze at elevated temperatures*, J. de Physique, **46**, C10—395 (1985).

[3] S. PILECKI, *Acoustic methods in testing of metals. Problems and methods of present acoustic (in Polish)*, IFTR PAS Warsaw 1991 pp. 71—156.

[4] S. PILECKI, W. IVANOW, A. LEBEDEV, *Proc. of ICIFUAS. 9*. Pergamon Press, Oxford 1990 pp. 583—586.

[5] S. PILECKI, W. IVANOV and A. LEBEDEV, phys. stat. sol a, **119**, 87—92 (1990).

[6] S. PILECKI and P. KOPANIA, Scient. Instrum., **4**, 4, 89—109 (1989).

[7] S. PILECKI and P. KOPANIA, *Equipment for the measurement of elasticity constants and internal friction of solids*, (in Polish) IFTR Reports 39 (1989).

[8] S. PILECKI, *The possibility of description of the average value of density and dislocation distribution by the equation of diffusion with source*, Engng. Trans., **36**, 2, 269—298 (1988).

[9] H.W. HAYDEN, W.G. MOFFATT and J. WULFF, *The structure and properties of materials*, vol. III. Mechanical behavior, J. Wiley, New York 1965.

[10] D.O. THOMPSON and D.K. HOLMES, J. Appl. Phys., **27**, 713 (1956).

[11] D.O. THOMPSON and V.K. PARE, in: Physical acoustics. Principles and methods [Ed.] W. Mason, Academic Press, 1967.

[12] H.G. VAN BUEREN, *Imperfectons in crystals*, North-Holland Publ., Amsterdam 1961.

[13] W.S. POSTNIKOV, *Vnutrenneje trenije w metallach*, Metalurgija, Moskva 1974.

[14] A. GRANATO and K. LÜCKE, J. Appl. Phys., 27, 583, 789 1956.
[15] M. PSTROKOŃSKI, Doctoral Thesis (in Polish), Institute of Gdańska University of Technology, Gdańsk 1980.
[16] S.P. NIKARANOV and B.K. KARDASHEV, *Elasticity and dislocation non-elasticity of crystals* (in Russian), Nauka, Moskva 1985.
[17] S. PILECKI, P. KOPANIA, S. KUSTOV, B. KARDASHEV, K. SAPOZHNIKOV, V. CHERNOV, *Dislocation internal friction in silicon bronze during and after plastic deformation*, Mater. Sci. Forum, 119—121, 261—266 (1993).
[18] S. PILECKI and A. LEVI, Proc. 1st Intern. Conf. on NDT, Roma 1983, I/22, 1—8.